Design and Analysis of Quasioptical Components for use in Astronomical Telescopes

Presented by

Rory Eoin Sheridan

Department of Experimental Physics, Maynooth University,

December 2018

Head of Department

J. Anthony Murphy

Research Supervisor:

Creidhe O'Sullivan

Co-Supervisor:

Darragh McCarthy

Contents

Abstract

This thesis describes the use of Gaussian beam modes (GBM) and physical optics (PO) to design and analyse astronomical telescope systems operating at millimetre and submillimetre wavelengths. The techniques are applied to a proposed re-design of the 3 mm channel of the 20 m Onsala Space Observatory telescope. The industry-standard software GRASP was used for the PO simulations; GBM analysis was carried out using code written in mathematical software packages. GRASP was used to investigate the effect of random and systematic surface errors on such systems. Finally, Maynooth University's Vector Network Analyser was calibrated, aligned and used to characterise new waveguide probes.

Acknowledgements

While my name occupies the author position of this thesis, it would be an act of great arrogance to not mention the numerous people who have helped me in this endeavour.

Thank you to my supervisor, Dr. Créidhe O'Sullivan, for all the assistance, patience and time she gave to me throughout both my undergraduate and postgraduate studies. Thank you for for all the helpful comments and advice over the duration of my thesis and for taking the time to answer my questions and then to help me understand these answer.

I would also like to thank Darragh McCarthy who, during his time with the department, always made himself available to answer questions or help me with any problems I had. Thank you for making yourself available for questions even after.

I would like to extend a massive thanks to all the other staff of the Experimental Physics department. Especially to Dr. Anthony Murphy, for making the department facilities available to me. Thank you also to Dr. Marcin Gradżiel for his help and training in using the VNA. Thank you to Mr. John Kelly for all his technical support, be it printer issues, network problems, or my hard drive crashing, John never got visibly annoyed, which is an achievement in itself. Last, but not least, thank you Gráinne Roche for all that you do in keeping the department organized, thank you for your support, for the advice, for the laughs, and for being an all round great friend.

Thank you to all my other postgrads who helped me down the line. Thank you

Chapter 1

Introduction

1.1 A Brief History of Astronomy

The mystery of the cosmos and all that it holds has held humans enthralled since the birth of our species and has given us a yearning to discover its many secrets. The night sky has been an object of religious worship and a timekeeping instrument; civilizations have studied the night sky and derived different meanings from their viewings. Celestial bodies such as the Sun, planets and meteors in the solar system were first considered as deities that created and controlled the Earth and its elements. As human society progressed calendars based on the position of these celestial bodies were established and land and sea navigation was made possible. In these modern times the science of astronomy is the window to our understanding of the universe and the laws of physics that govern it.

In the beginning of the long history of astronomy, the skies were observed using the naked eye. Even with this crude method, many great advances in the field were made. Nicholaus Copernicus first introduced the concept that our solar system was heliocentric, as opposed to the geocentric model of the time. The famous astronomer and mathematician Johannes Kepler developed three renowned equations of plane-

tary motion from the naked eye viewings of Tycho Brahe. Then, with the invention of the telescope, Galileo had a tool to view our local system in more detail than had ever been done before. Even with the advancement of the telescope, observers were still limited to viewing within the optically visible region of the electromagnetic spectrum. However, this changed when, in 1931, Karl Jansky first detected radio emissions from astronomical sources. These astronomical radio emissions were found to be emanating from the centre of the Milky Way and subsequently a number of other sources in the sky such as radio galaxies, quasars, supernova remnants and the cosmic microwave background were discovered. Soon afterwords the world of astronomical observations was opened to all regions of the electromagnetic spectrum (figure 1.1)
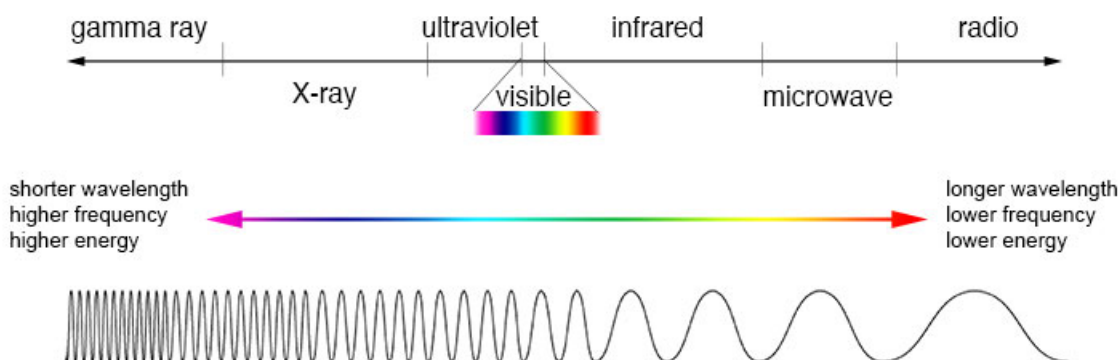
Figure 1.1: Electromagnetic Spectrum. [NASA, 2013]

Each region of the spectrum required different technologies to observe and record the radiation. Telescopes began to be developed that were tailored towards specific regions of the spectrum. Examples of recent specialised technology include the Wilkinson Microwave Anistropy Probe (WMAP) [NASA, 2010] and the Planck satellite [ESA, 2009] which observed in the microwave region, the Fermi Gamma-ray Space telescope [NASA, 2017] for astronomy at gamma-ray wavelengths, the Atacama Large Millimeter Array [ALMA] which operates at the millimetre to sub-

millimetre band and finally the Chandra x-ray Observatory [Harvard, 2014] which views in the X-ray region.

When observing the sky, using only one region of the spectrum can vastly limit the information that can be gathered. Certain aspects and characteristics of astronomical objects, while being opaque at a certain wavelength, can become transparent or visible in another. Figure 1.2 depicts an example of this using the galaxy M33 which has had an image taken at five different wavelengths.
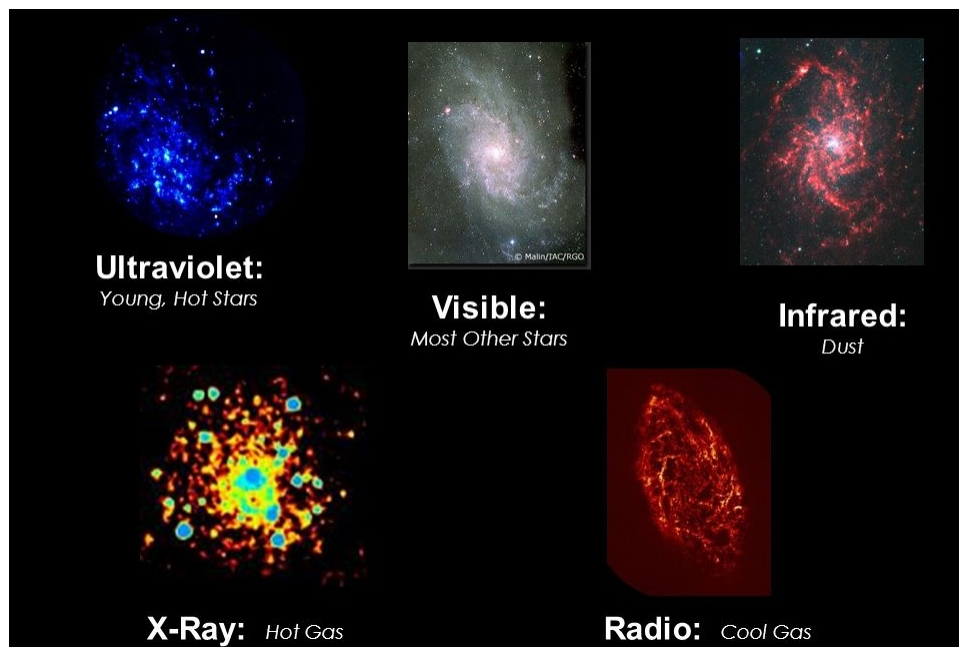
Figure 1.2: Galaxy M33 viewed using different wavelengths of radiation [Lyons, 2016].

From figure 1.2 it is clear that each different wavelength M33 is observed at gives different information about the galaxy. Ultraviolet and visible light allow for the stars that make up the galaxy to be seen. The hot gas of heavy elements within the galaxy is visible at x-ray wavelengths, and the cooler dust and gas become visible at infrared and radio wavelengths respectively.

The region of radiation relevant to this thesis falls between the infrared and microwave domains of the spectrum and is known as the millimetre and submillimetre wavebands.

1.2   Millimetre and Submillimetre Astronomy

The Millimetre and submillimetre bands of radiation refer to an area that lies between the infrared and microwave regions of the electromagnetic spectrum. The boundaries between the upper part of the infrared band and the start of the submillimetre are quite blurred and the term terahertz band (a reference to the frequency of the radiation) is commonly used to describe the submillimetre region of the spectrum. Typically 'Submillimetre' refers to the band of radiation in the wavelength range of 100 μm - 1 mm or the frequency range of 0.3 THz to 3 THz. Millimetre radiation frequencies extend from 300 GHz to 30 GHz or wavelengths of 1 mm to 10 mm.

After the massive strides made in astronomy and its technological advances, the terahertz region was the least developed domain of the spectrum. This lack of exploration was mainly due to the unavailability of detectors capable of dealing with terahertz radiation. Because of this, the area became known as the 'terahertz' gap. The development of terahertz radiation research has opened up a number of avenues for profitable applications. Medicine [Pawar et al., 2013], security [Liu et al., 2007], communications [Akyildiz and Han, 2014] and astronomy [Withington, 2004] are some areas where submillimetre technology is becoming a strong addition.

Astronomy at terahertz frequencies is a popular branch of astrophysics as there are many astronomical objects that radiate here. Thermal blackbody radiation from objects at temperatures between 40 and 480 K peaks in this part of the electromagnetic spectrum. As a result there are a number of important astronomical objects, such as circumstellar and interstellar gas and dust, which have significant

emission within this band. Interstellar dust, for example, can have temperatures of approximately 10 K in its cooler regions, up to 200 K in the denser regions. The cosmic microwave background (CMB) also emits significant radiation within the lower frequencies of the millimetre band. Photons from highly-redshifted galaxies, obscured by dust that optical and UV radiation cannot penetrate, are absorbed and re-emitted at wavelengths that fall within the submillimetre range. In addition, the chemical make up of dust and gas clouds can also be determined from the spectral lines caused by rotational and atomic transitions in the submillimetre band. This band is particularly rich in lines from important species such as CO and OH [Schilke et al., 1997].

At millimetre wavelengths, with the exception of particular O_2 and H_20 lines that are present, there is a certain amount of transparency through the atmosphere. Contrary to this, there are a large number of atmospheric absorption bands in the submillimetre band (mostly from H_20) and the abundance of water vapour in the atmosphere means it is mostly opaque. Figure 1.3 gives a representation of the levels of transmission for the atmosphere at different wavelengths. In both the millimetre and submillimetre the atmosphere offers a relatively low level of transmission. To combat this, the majority of ground-based telescopes designed to operate at these wavelengths are placed in areas where the amount of absorption due to water vapour is at a minimum. Dry, high environments allow for this. ALMA and the James Clerk Maxwell Telescope (JCMT) [EAO] are both examples of ground based observatories for submillimetre and millimetre astronomy. ALMA, situated in the Chilean desert at an altitude of 5,058 meters above sea level and JMCT, which sits on the summit of Mauna Kea in Hawaii at 4,092 metres above sea level, are both in ideal locations for the placement of telescopes sensitive to water vapour.
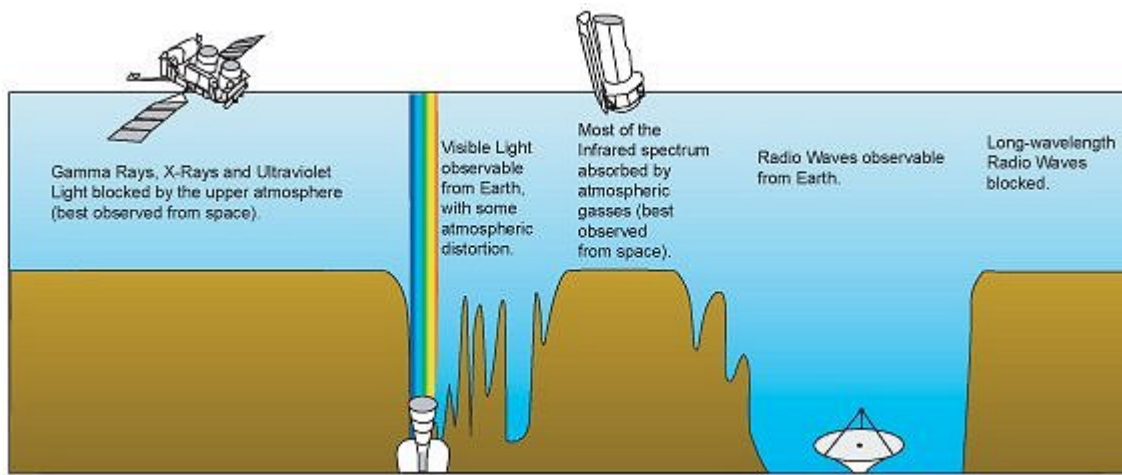
Figure 1.3: Representation of how transmissive the atmosphere is to the different regions of the EM spectrum [Montgomery et al., 2015].

Leaving Earth's atmosphere is also an option for this branch of astronomy. Odin [Frisk et al., 2003] was a Swedish led astronomy/aeronomy satellite with a major contribution from Onsala Space Observatory who provided the submillimetre radiometer (4 channels around 500 GHz) and the overall integration and test of the system including a 119 GHz radiometer provided by Finland. The Planck Telescope [ESA, 2009] is another such example. Operated by ESA from 2009 to 2013, this telescope was placed into orbit around L2 and mapped the anisotropies of the cosmic microwave background (CMB) at microwave and infrared wavelengths. While this method of observation offers unhindered views of the deep universe it has its drawbacks, it is costly, involves a significant amount of technology development and space-based instruments are difficult to maintain.

A large portion of this theses is concerned with the analysis and design aspects of the Onsala 20 m telescope [Cumming and Nystås, 2014]. This telescope operates in two channels called the 3 mm and 4 mm channels. As well as operating as a standalone telescope, Onsala is part of a number of international projects, such as the Global Millimeter VLBI Array (GMVA) working alongside a number of observatory

stations: Effelsberg (Germany), Plateau de Bure (France), Pico Veleta (Spain), Yebes (Spain) and a number of others. [Hodgson et al., 2014]. Onsala has also had a hand in the development [SKA, 2019] of the Square Kilometre Array (SKA) [SKA].

1.3   Optical Modelling

Terahertz radiation lies in a middle ground between short wavelength radiation and long wavelength radiation (when compared to component size) and this causes some difficulty when attempting to examine a system. At small wavelengths (such as in the optical where the wavelength is sufficiently small when compared to the component size) standard geometrical optics can be used to map a beam of radiation as it propagates through a system. At larger wavelengths, however, diffraction is significant and the use of more accurate electromagnetic analyses such as physical optics is required. For very large wavelengths this is not too onerous a calculation but in the terahertz region it can be very time consuming.

When trying to map or analyse a beam of radiation in the terahertz band, a technique known as 'quasi-optics' is often used. This method of analysis is based on the propagation of Gaussian Beam mode solutions of the paraxial equation. Gaussian Beam mode analysis is an effective method of creating an initial model of an optical system as it is quite time efficient. It is a more accurate method when compared to ray tracing, however not as accurate as, for example, physical optics. Physical optics, or wave optics, is a method of analysis that considers all wave phenomena that radiation undergoes as it travels through a system.

In Chapter 2, the theory behind these methods will be explained in greater detail.

1.4   Other Applications

Along with astronomy, the generation and detection of terahertz radiation has opened up a number of other commercial and industrial avenues. A few examples of these are summarised below.

- **Security**

  Security systems that operate in the terahertz region allow for screening of sharp objects and illegal substances. The human body absorbs this terahertz radiation while most metallic and ceramic materials reflect them. This absorption by the skin is much safer than scanning at x-ray wavelengths as terahertz radiation is lower in energy and non-ionizing which limits cell damage. This characteristic of terahertz radiation would be especially useful in the case of airport security. [Federici et al., 2005]

- **Non-Destructive Testing**

  Terahertz radiation can penetrate many materials such as paper, plastics, textiles and foam. This characteristic of terahertz radiation can be used as a method of examining the interior of closed objects. The Colombia space shuttle disaster was attributed to manufacturing defects of foam materials within the shuttle, after this NASA turned to research in detector systems that used terahertz radiation for remote sensing of any flaws [NASA]. The relatively short wavelength of terahertz radiation also allows for high spatial resolution.

- **Medical**

  Due to the sensitivity of terahertz wavelengths to water, terahertz radiation offers a potential way of investigating human tissue. Certain cancers can be effectively detected by scanning at terahertz frequencies. Terahertz radiation can also be used to investigate wounds beneath bandages allowing for safer

treatment [Pickwell et al., 2004].

- **Communication**

  Terahertz radiation is high frequency and so has a large bandwidth allowing for much larger amounts of data to be transferred [Sethy et al., 2015] compared with traditional bands. So far, only short distance wireless communication is possible due to the attenuation of terahertz beams through air, however the transmission through space is mostly lossless offering long range communications with the use of little power.

- **Terahertz Spectroscopy**

  In typical spectroscopy, radiation of different frequencies are filtered and separated using gratings and the radiation transmitted through a sample is measured to obtain its spectrum. Terahertz Time Domain Spectroscopy (THz -TDS) is spectroscopy using broadband terahertz pulses as the light source. Terahertz pulses have a very short time width but contain a broadband frequency spectrum. The waveform collected after it is transmitted through a sample is then used to deduce the sample spectrum. [Dean et al., 2014]

1.5   Contents of this Thesis

A large portion of this thesis pertains to the methods and techniques used in the design and analysis of submillimetre and millimetre telescope systems, predominantly the Onsala 20 m telescope.

Along with this, an examination using the ZVA-24 Rohde and Schwarz Vector Network Analyser is carried out. This involves examining the techniques used in the alignment of the optical components which transmit and receive specified signals, and the effects of this on subsequent measurements of terahertz systems in the laboratory. The following is a breakdown of the contents of this thesis.

1.5.1   Chapter 2: Optical Modelling

Chapter 2 introduces the techniques and methodologies for modelling terahertz radiation that are used throughout the thesis. An introduction to Gaussian beams and quasioptical analysis is given as well as a look at the use of ray matrices. All of these methods are used in the design of optical systems in the following chapters. An introduction to GRASP [TICRA, 2013], a physical optical analysis software program, is also given. The techniques that this software uses are described.

1.5.2   Chapter 3: Re-Design and Analysis of the Onsala 3-mm Receiver

Chapter 3 describes the analysis of telescope and receiver systems and of the Onsala 20 m telescope receivers in particular. An analysis of the system was carried out using Gaussian beam mode/ray matrix theory and GRASP physical optics. The same methods were then applied to a feasibility study for a proposed redesign of the receiver for the current 3 mm channel.

1.5.3   Chapter 4: Surface Tolerance Simulations with GRASP

In chapter 4, the effects of manufacturing non-idealities are investigated using GRASP physical optics. Varying levels of these aberrations are simulated by adding them to models of the receiver mirror surfaces in the 4 mm channel of the Onsala 20 m telescope. The effect that these errors on the reflectors have is found by comparing the output beam to that of a perfect system.

1.5.4   Chapter 5: Vector Network Analyser

In this chapter the Vector Network Analyser (VNA) is introduced. The VNA is used to make laboratory measurements of the amplitude and phase of radiation

in the W-band (70 - 110 GHz). Modelling techniques and predictions are verified using such measurements and so it is important to fully understand the operation and performance of the VNA. The process used to calibrate and align this sensitive piece of equipment is outlined, and some example measurements are given.

1.5.5   Chapter 6: Summary and Conclusions

In the final chapter, the main results of the work carried out in this thesis are summarised and discussed.

Chapter 2

Optical Modelling

2.1 Introduction

When designing an optical system, the best method to use depends on the region of
the electromagnetic spectrum that it operates in. For the most part, when dealing
with visible light, geometrical optics is the standard technique. Geometrical optics
works quite well when the radiation being examined has a wavelength that is neg-
ligible when compared to component sizes. However when the wavelength becomes
comparable to the dimensions of the objects it is interacting with, the propagation
is dominated by diffraction effects. Physical optics (see eg. [Chirkin, 1999]) is an
accurate way of analysing such long wavelength beams (when the wavelength is of
the same order of magnitude, or larger, than component sizes) but it becomes com-
putationally expensive for shorter wavelengths. The terahertz band lies between
these extremes and we are dealing with what is often called quasi-optics. Here the
beam size is moderately large relative to the wavelength of the beam. Two useful
tools that are used to characterise beams of radiation within this band [Winnewisser,
1997] are Gaussian Beam Mode Analysis (GBMA) and matrix ray transformation
[Bernal, 2016]. GBMA is an effective method of modelling a propagating Gaussian
beam by calculating how its beam width and phase radius of curvature vary. As

19

a beam progresses through a system, its beam width begins to change as does its phase radius of curvature. Ray matrices allow for a concise and efficient method of seeing how a beam changes as it propagates through the components of the system. In this chapter, the principle of both these analysis methods will be described. A brief introduction into the simulation software, GRASP which implements physical optics, will also be outlined in this chapter.

2.2 The Paraxial Equation

A Gaussian beam can be considered as a well collimated beam of radiation that has a well defined direction of propagation. It has transverse electric and magnetic fields. Its electric field has a Gaussian amplitude profile which changes in width as a function of distance. A benefit of using Gaussian beam modes is that calculations are not computationally expensive and so can be carried out on a short time scale. The term "mode" refers to an analytical solution of the paraxial equation. Over the next few pages I will outline how to derive a Gaussian beam's propagation for a fundamental Gaussian beam as well higher mode beam. Much of this is referenced from [Goldsmith, 1998].

Deriving an expression for Gaussian beam modes [Goldsmith, 1998] begins by taking the Helmholtz wave equation for an electromagnetic field:

$$(\nabla^2 + k^2)E = 0. \tag{2.1}$$

Here E is the electric field which can be expressed as:

$$E(x, y, z) = u(x, y, z)e^{-ikz}. \tag{2.2}$$

u is the scalar function that describes the non-plane wave part of the beam, z is the axis of propagation, k is the wavenumber $\left(\frac{2\pi}{\lambda}\right)$ and in this equation the time dependence $(e^{i\omega t})$ has been excluded. The Helmholtz equation then expands to:

$$\frac{\partial^2 E}{\partial x^2} + \frac{\partial^2 E}{\partial y^2} + \frac{\partial^2 E}{\partial z^2} + k^2 E = 0. \tag{2.3}$$

Substituting for E the expression in equation (2.2)

$$\frac{\partial^2 u}{\partial x^2} + \frac{\partial^2 u}{\partial y^2} + \frac{\partial^2 u}{\partial z^2} - 2jk\frac{\partial u}{\partial z} = 0. \tag{2.4}$$

Finally, this equation can be further simplified by applying the paraxial approximation. If the terms in equation 2.4 are considered individually, the paraxial approximation assumes that the third term, describing the magnitude of the variation of the field along the z axis (i.e. the axis of propagation), is much smaller than the first, second and fourth terms. Due to this, the third term can be dropped from the equation. This gives us the paraxial equation in rectangular coordinates:

$$\frac{\partial^2 u}{\partial x^2} + \frac{\partial^2 u}{\partial y^2} - 2jk\frac{\partial u}{\partial z} = 0. \tag{2.5}$$

2.3 The Fundamental Gaussian Beam Mode Solution in Cylindrical Coordinates

The paraxial equation can be solved in various coordinate systems (see [Goldsmith, 1998] for more detail). When dealing with optical system components such as feed horns and lenses, which are often rotationally symmetric, it is common practice to convert the equation to cylindrical coordinates. Here the z axis is still taken as the axis of propagation. The term r is used to describe the perpendicular distance from the propagation axis and the angular coordinate is denoted by φ. The paraxial equation in cylindrical coordinates is:

$$\frac{\partial^2 u}{\partial r^2} + \frac{1}{r}\frac{\partial u}{\partial r} + \frac{1}{r^2}\frac{\partial^2 u}{\partial \varphi^2} - 2jk\frac{\partial u}{\partial z} = 0. \tag{2.6}$$

Commonly it is assumed that the beam is axially symmetric and therefore u is independent of φ. The equation can then be simplified to:

$$\frac{\partial^2 u}{\partial r^2} + \frac{1}{r}\frac{\partial u}{\partial r} - 2jk\frac{\partial u}{\partial z} = 0. \tag{2.7}$$

The simplest form of an axially symmetric paraxial wave solution is of the form:

$$u(r,z) = A(z)e^{\frac{-jkr^2}{2q(z)}}. \tag{2.8}$$

Here A and q are complex functions which are defined separately. u is Gaussian-like in its field distribution. Substituting the expression for u into equation 2.7 gives:

$$-2jk\left(\frac{A}{q} + \frac{\partial A}{\partial z}\right) + \frac{k^2 r^2 A}{q^2}\left(\frac{\partial q}{\partial z} - 1\right) = 0. \tag{2.9}$$

For equation 2.9 to be always (for all values of z) true each part must be individually equal to zero. This leads to two relationships:

$$\frac{dq}{dz} = 1. \tag{2.10}$$

$$\frac{dA}{dz} = -\frac{A}{q}. \tag{2.11}$$

Equation 2.10 has the following solution:

$$q(z) = q(z_0) + (z + z_0). \tag{2.12}$$

Here z_0 refers to the reference position of the wave which can be defined as $z_0 = 0$. Equation 2.12 becomes:

$$q(z) = q(0) + z. \tag{2.13}$$

$q(z)$ is known as the **complex beam parameter** or **Gaussian beam parameter**. In equation 2.8 q appears in the form $\frac{1}{q}$ and it can be written as:

$$\frac{1}{q} = \left(\frac{1}{q}\right)_r - j\left(\frac{1}{q}\right)_i. \tag{2.14}$$

Here r and i refer to the real and imaginary part of $\frac{1}{q}$. The last term in equation 2.8 becomes:

$$e^{\frac{-jkr^2}{2q(z)}} = e^{\frac{-jkr^2}{2}\left(\frac{1}{q}\right)_r - \frac{kr^2}{2}\left(\frac{1}{q}\right)_i}. \tag{2.15}$$

The imaginary part of this expression has the form of the phase variation of a spherical wavefront in the paraxial limit. If the phase radius of curvature is R then within the limit $r << $ R, the phase delay of the wavefront can be written as:

$$\phi(r) \approx \frac{kr^2}{2R}. \tag{2.16}$$

Figure 2.1 shows an example of $\phi(r)$ for a propagating wave. The real part of q can be identified with the phase radius of curvature of the beam:

$$\left(\frac{1}{q}\right)_r = \frac{1}{R}. \tag{2.17}$$

As q is a function of z, it is clear that as the beam propagates the radius of curvature of the beam will change depending on the position of the beam along its propagation axis.
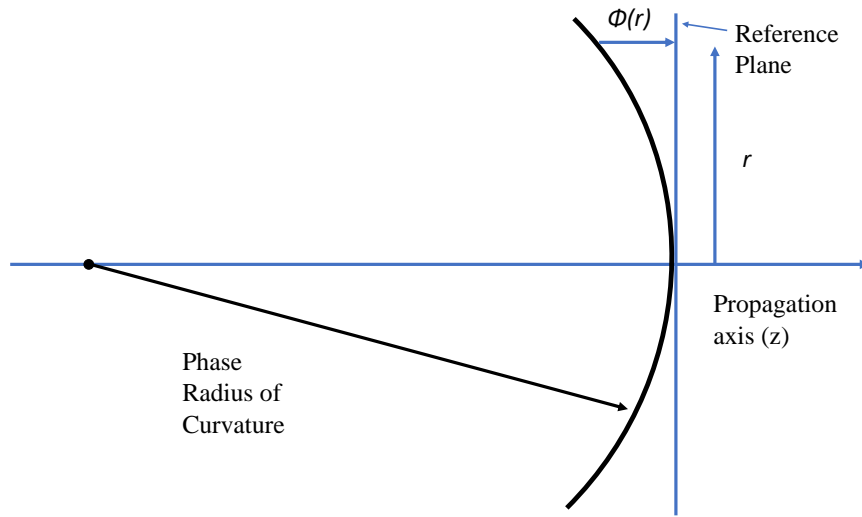
Figure 2.1: The phase delay (ϕ_r) of a spherical wave relative to a plane wave along its axis of propagation.

In equation 2.15 it can be seen that the second part of the exponent is real and has a Gaussian variation as a function of distance along the plane perpendicular to the propagation axis (the transverse plane). To write it in the form of a Gaussian distribution ($e^{-(\frac{r}{r_0})^2}$) we can set:

$$\left(\frac{1}{q}\right)_i = \frac{2}{kr_0^2} \tag{2.18}$$

where r_0 represents the radius where the amplitude falls to $\frac{1}{e}$ relative to its on-axis value. r_0 is usually written as w and is known as the beam radius, w also vaires with z. So $(\frac{1}{q})_i$ can be written as:

$$\left(\frac{1}{q}\right)_i = \frac{2}{kw^2(z)} = \frac{\lambda}{\pi w^2(z)}. \tag{2.19}$$

With this in mind, the function $\frac{1}{q}$ is given by:

$$\frac{1}{q} = \frac{1}{R(z)} - \frac{j\lambda}{\pi w^2(z)}. \qquad (2.20)$$

Looking back at equation 2.8, taking $z = 0$ and choosing an initial beam radius w_0 such that $w_0 = \sqrt{\frac{\lambda q(0)}{j\pi}}$, the relative field distrubition in the transverse plane can be described as:

$$u(r,0) = u(0,0)e^{\frac{-r^2}{w_0^2}}. \qquad (2.21)$$

Here w_0 is the beam radius when it is at its narrowest. w_0 is also called the beam waist radius and calculated as the beam radius at $z = 0$. This can be linked to important expression for q:

$$q = \frac{j\pi w_0^2}{\lambda} + z \qquad (2.22)$$

Using equation 2.20 and 2.22 allows the phase radius of curvature and the beam radius at any plane along the propagation axis to be calculated:

$$R = z + \frac{1}{z}\left(\frac{\pi w_0^2}{\lambda}\right)^2 \qquad (2.23)$$

$$w = w_0\sqrt{1 + \left(\frac{\lambda z}{\pi w_0^2}\right)^2}. \qquad (2.24)$$

As well as the beam radius being at a minimum at $z = 0$ it can be seen that at this plane the phase radius of curvature becomes infinite. From both of these equations it can be seen that the waist and radius of curvature are wavelength dependent and as $\lambda \to 0$ the beam radius becomes constant with z while the radius of curvature tends to infinity.

By now it is apparent how the beam radius and phase radius of curvature of the beam change as it propagates. To complete the expression of a basic Gaussian mode, we also include how the phase of the beam varies. From equations 2.10 and 2.11 it can be written that $\frac{dA}{A} = -\frac{dq}{q}$. Integrating this from $z = 0$ to z gives:

$$\frac{A(z)}{A(0)} = -\frac{q(0)}{q(z)}. \tag{2.25}$$

Here q can be substituted with the expression 2.22 to give:

$$\frac{A(z)}{A(0)} = \frac{1 + \frac{j\lambda z}{\pi w_0^2}}{1 + (\frac{\lambda z}{\pi w_0^2})^2}. \tag{2.26}$$

It is convenient to describe the term $\frac{\lambda z}{\pi w_0^2}$ in the form of a phasor by defining:

$$\tan(\phi_0) = \frac{\lambda z}{\pi w_0^2} \tag{2.27}$$

and substituting this into equation 2.26. Using standard trigonometric identities along with equation 2.24, equation 2.26 becomes:

$$\frac{A(z)}{A(0)} = \frac{w_0}{w}e^{j\phi_0}. \tag{2.28}$$

ϕ_0 is called the Gaussian beam phase shift, and using this a complete expression for the fundamental Gaussian beam mode can be written (where it is assumed the amplitude on-axis at the beam waist is unity):

$$u(r, z) = \frac{w_0}{w}e^{\left(\frac{-r^2}{w^2} - \frac{j\pi r^2}{\lambda R} + j\phi_0\right)}. \tag{2.29}$$

Finally, the electric field can be obtained using equation 2.2 as:

$$E(r, z) = \frac{w_0}{w}e^{\left(\frac{-r^2}{w^2} - jkz - \frac{j\pi r^2}{\lambda R} + j\phi_0\right)}. \tag{2.30}$$

Here, the only difference from equation 2.29 is the inclusion of the plane wave phase factor.

To relate the electric field in equation 2.30 to the power in a Gaussian beam, the assumption is made that the electric and the magnetic components of the field are related to each other in a similar way to those in a plane wave and the power is proportional to the square of the electric field. A convenient method for normalizing this is to set the integral of the total power within a beam to unity:

$$\int_{r=0}^{r=\infty} \mid E^2 \mid 2\pi r dr = 1 \tag{2.31}$$

Evaluating the integral in equation 2.31 using the field from equation 2.30 at $z = 0$ will give $\frac{\pi w_0^2}{2}$. From this, the normalized electric field distribution along the axis of propagation is:

$$E(r, z) = \sqrt{\frac{2}{\pi w^2}} e^{\left(\frac{-r^2}{w^2} - jkz - \frac{j\pi r^2}{\lambda R} + j\phi_0 \right)} \tag{2.32}$$

Using equation 2.32 along with the expressions for $R(z)$, $w(z)$ and $\phi(z)$ (equations 2.23, 2.24 and 2.27) allows us to model the propagation of a Gaussian beam in free space.

2.4 The Fundamental Gaussian Beam Mode Solution in Rectangular Coordinates

It is also possible to derive an expression for the fundamental Gaussian beam mode in rectangular coordinates. This can be done for a beam that varies in one or two-dimensions as it travels. In the case of one-dimension, the beam is assumed to be varying in one coordinate perpendicular to its axis of propagation while the other

remains the same. The paraxial wave equation, in this case, becomes:

$$\frac{\partial^2 u}{\partial x^2} - 2jk\frac{\partial u}{\partial z} = 0 \tag{2.33}$$

Using a trial simple solution for a paraxial wave similar to equation 2.8 we get:

$$u(x,z) = A_x(z)e^{\frac{-jkx^2}{2q_x(z)}}. \tag{2.34}$$

Using this, a solution for the variable q can be derived which is of the same form as that of equation 2.20:

$$\frac{1}{q_x} = \frac{1}{R_x} - \frac{j\lambda}{\pi w_x^2}. \tag{2.35}$$

Following this, the normalized form of the electric field distribution can be found:

$$E(x,z) = \left(\frac{2}{\pi w_x^2}\right)^{0.25} e^{\frac{-x^2}{w_x^2} - jkz - \frac{j\pi x^2}{\lambda R_x} + \frac{j\phi_{0x}}{2}}. \tag{2.36}$$

Here, w_x, R_x and ϕ_{0x} are defined in a similar way to w, R and ϕ_0 in equations 2.23, 2.24, 2.27 and refer to the beam in the x-coordinate as it propagates in the z-direction.

To solve the paraxial equation in two-dimensions, following Goldsmith [Goldsmith, 1998], a trial solution that is independent in x and y of the form:

$$u(x,y,z) = A_x(z)A_y(z)e^{\frac{-jkx^2}{2q_x}} e^{\frac{-jky^2}{2q_y}} \tag{2.37}$$

is used.

If we require that it is a solution independently for all x and y we get a normalised solution of the form:

$$E(x,y,z) = \sqrt{\frac{2}{\pi w_x w_y}} e^{\frac{-x^2}{w_x^2} \frac{-y^2}{w_y^2} \frac{-j\pi x^2}{\lambda R_x} \frac{-j\pi y^2}{\lambda R_y} + \frac{j\phi_{0x}}{2} \frac{j\phi_{0y}}{2}} \tag{2.38}$$

where $w_y = w_{0y}\sqrt{1 + (\frac{\lambda z}{\pi w_{0y}^2})}$ with w_{0y} being the beam waist radius in the y-direction and w_{0x} is the beam waist radius in the x-direction. In the case where the beam waist in the x and y directions have the same radius ($w_{0x} = w_{0y} = w_0$) and location, we recover the same solution as equation 2.32.

2.5   Higher Order Gaussian Modes

The Gaussian beam solutions that have been derived so far, known as the fundamental Gaussian beam mode, are of a simple form and, while they are often very useful in many situations, solutions having a more complex amplitude variation may be required. More complex solutions to the paraxial wave equation can be found and these solutions, while having similar characteristics as the fundamental beam mode in terms of their beam width and radius, experience a different phase shift as they propagate. These 'higher order' solutions are formed by superimposing a number of polynomials over the fundamental mode. The extra phase shift is mode dependant. The importance of these higher order modes for this project is that they give a more accurate representation of a beam from a corrugated horn which, while having a large amount of axial symmetry, is not completely Gaussian.

2.5.1   Higher Order Modes in Cylindrical Coordinates

To derive higher order modes in cylindrical coordinates, the trial solution must allow a variation in the polar angle φ. The solution can be written as:

$$u(r, \varphi, z) = A(z)e^{-\frac{jkr^2}{2q(z)}}S(r)e^{jm\varphi}. \tag{2.39}$$

The $S(r)$ term in this equation refers to an unknown radial function and m is some integer. The complex amplitude $A(z)$ and complex beam parameter are still both functions of z. If q is assumed to have the same form as that for the fundamental

Gaussian beam mode, the solutions to the paraxial wave equations is:

$$S(r) = \left(\frac{\sqrt{2}r}{w} \right)^m L_{pm} \left(\frac{2r^2}{w^2} \right) \qquad (2.40)$$

where, w refers to the beam radius and L_{pm} is a generalised Laguerre function in which p and m represent the radial and angular index respectively. The Laguerre function is a solution of the associated Laguerre equation that can be written as [Riley et al., 2006]:

$$u \frac{d^2 L_{pm}}{du^2} + (m + 1 - u) \frac{dL_{pm}}{du} + p L_{pm} = 0. \qquad (2.41)$$

The function $L_{pm}(u)$ can be obtained:

$$L_{pm}(u) = \frac{e^u u^{-m}}{p!} \frac{d^p}{du^p} e^{-u} u^{p+m}. \qquad (2.42)$$

Using this, the electric field distribution for the normalized Gaussian-Laguerre beam in cylindrical coordinates takes the form:

$$E_{pm}(r, \varphi, z) = \sqrt{\frac{2p!}{\pi(p+m)!}} \ \frac{1}{w(z)} \left(\frac{\sqrt{2}r}{w(z)} \right)^m L_{pm} \left(\frac{2r^2}{w^2(z)} \right)$$
$$. e^{\frac{-r^2}{w^2(z)} - jkz - \frac{j\pi r^2}{\lambda R(z)} - j(2p+m+1)\phi_0(z) + jm\varphi} \qquad (2.43)$$

Once again, the beam radius (w), phase radius of curvature (R) and phase shift (ϕ_0) are the same as that for the fundamental Gaussian beam mode. The mode dependant "phase slippage" occurs because of the $(2p + m + 1)$ factor in the phase term.

The Gaussian-Laguerre function L_{00} is the same as the fundamental Gaussian beam mode but as the orders of p and m increase, the beam begins to take on the

complexity that is inherent in higher order modes.

2.5.2   Higher Order Modes in Rectangular Coordinates

In the same way as higher order modes, when described in cylindrical coordinates, are the products of the fundamental Gaussian beam mode and solutions to the Laguerre equation, in a rectangular coordinate system they are products of the fundamental mode and Hermite polynomials.

To derive the Gaussian-Hermite beam polynomials, a paraxial wave solution must be solved in two-dimensional rectangular coordinates. A typical two-dimensional Gaussian beam is the product of two one-dimensional modes. These can be separated into the x and y dimensions. Starting with the x-dimension a trial solution of the form:

$$u(x,z) = A(z)H\left(\frac{\sqrt{2}x}{w(z)}\right)e^{-\frac{jkx^2}{2q(z)}} \qquad (2.44)$$

works if the the beam radius w and the complex beam parameter q are taken to be the same as for the fundamental mode. H is a function that satisfies Hermite's differential equation:

$$\frac{d^2H(u)}{du^2} - 2u\frac{dH(u)}{du} + 2mH(u) = 0. \qquad (2.45)$$

Here, m is a positive integer, $H_0(u) = 1$, $H_1(u) = 2u$, and the remaining polynomials of order m have the form;

$$H_{n+1}(u) = 2[uH_n(u) - nH_{n-1}(u)]. \qquad (2.46)$$

Using this, the normalized electric field in rectangular coordinates and in one-dimension can be written as:

$$E_m(x,z) = \sqrt[4]{\frac{2}{\pi}}\sqrt{\frac{1}{w_x 2^m m!}} H_m\left(\frac{\sqrt{2}x}{w_x}\right) e^{-\frac{x^2}{w_x^2} - jkz - \frac{j\pi x^2}{\lambda R_x} + \frac{j(2m+1)\varphi_{0x}}{2}}. \tag{2.47}$$

Finally, as previously stated, the two-dimensional solution is formed using the product of the individual x and y expression of the form in equation 2.47. The normalized electric field distribution for a two-dimension Gaussian-Hermite beam is:

$$
\begin{aligned}
E_{mn}(x,y,z) = &\sqrt{\frac{1}{\pi w_x w_y 2^{m+n-1} m! n!}} H_m\left(\frac{\sqrt{2}x}{w_x}\right) H_n\left(\frac{\sqrt{2}y}{w_y}\right) \\
&.e^{-\frac{x^2}{w_x^2} - \frac{y^2}{w_y^2} - jkz - \frac{j\pi x^2}{\lambda R_x} - \frac{j\pi y^2}{\lambda R_y} + \frac{j(2m+1)\varphi_{0x}}{2} + \frac{j(2m+1)\varphi_{0y}}{2}}
\end{aligned}
\tag{2.48}
$$

Because the fundamental and higher order modes are solutions to the paraxial wave equation, the form of their amplitude distributions remains unchanged as they propagate. This is what makes them so useful for optical modelling. They constitute a complete orthonormal set so any arbitrary solution to the wave equation can be expressed as a linear superposition of these modes as described next.

2.6 Mode Coefficients

An arbitrary field distribution can be described using a superposition of propagating free space modes (ψ_n) each with a scaling factor (A_n) known as the mode coefficient. Equation 2.49 describes this field:

$$Field = \sum_{n=0}^{N} A_n \psi_n. \tag{2.49}$$

To determine the coefficients, an overlap integral is performed between the field and the mode at a plane, S, where the field is known. This integral can be written as:

$$A_n = \int_S (Field)\psi_n^* dS. \tag{2.50}$$

To describe the field at another plane, the modes are propagated along z and the summation of the modes is calculated again at this plane. The mode coefficients stay the same (if no truncation or loss of power is present in the optical system), however the beam radius, phase radius of curvature and phase slippage change as described earlier. Beam coefficients can also be complex. These techniques are used later in Chapter 3 to calculate the power in a beam through an optical system.

2.7   Propagation of a Gaussian beam

As a Gaussian beam travels along the z axis, the beam radius, radius of curvature and phase slippage vary (equations 2.24, 2.23, 2.27). An example of the evolution of a Gaussian beam as it propagates can be seen in Figures 2.2 and 2.3 [Goldsmith, 1998].

Figure 2.2: A visual representation of how a Gaussian beam spreads as it propagates.
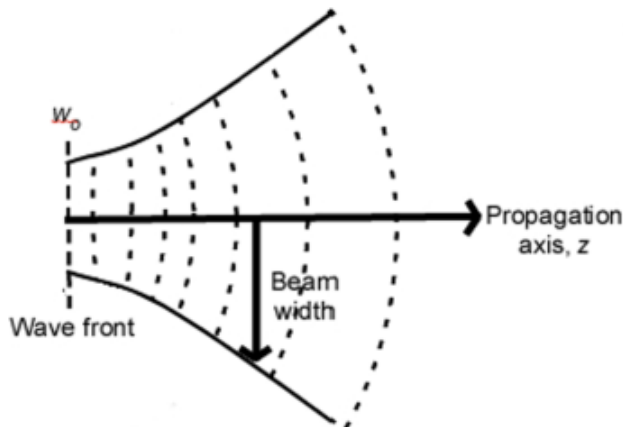
Figure 2.3: As the beam spreads, its radius of curvature changes along with it.

As the beam radius reaches its minimum size, that is, its waist radius (w_0), the phase radius of curvature approaches that of a plane wave $(R \approx \infty)$. If the convention of left to right being the positive propagation direction is taken, as the beam reaches its waist location the radius of curvature has a large negative value (converging beam). At the waist location the radius of curvature becomes infinite, from here it reaches a positive minimum value (Figure 2.4) and then again increases in value as it propagates (diverging beam). Figure 2.5 shows the evolution of the beam width from its minimum waist value at $z = 0$.

The propagation of a Gaussian beam can also be described in terms of a parameter called the confocal distance:

$$z_c = \frac{\pi w_0^2}{\lambda}. \tag{2.51}$$

The confocal distance is a position along a beam's propagation axis which separates the near-field and the far field region of the beam i.e. the near field region corresponds to the region where $z \ll z_c$ while the far field region corresponds to $z \gg z_c$. Using this value to express a beam's characteristics, the beam radius, phase radius

of curvature and phase slippage can be written as:

$$R = z + \frac{z_c^2}{z} \tag{2.52}$$

$$w = w_0 \sqrt{1 + \left(\frac{z}{z_c}\right)^2} \tag{2.53}$$

$$\phi_0 = \tan^{-1}\left(\frac{z}{z_c}\right). \tag{2.54}$$

Also known as the Rayleigh range the confocal distance is a useful way of describing a beam in reference to its waist position. When the beam's parameters are defined using the confocal distance it can be seen that in the near field, the radius of curvature of the beam is inversely proportional to z while in the far field the radius of curvature can be approximated as $R(z) \approx z$.
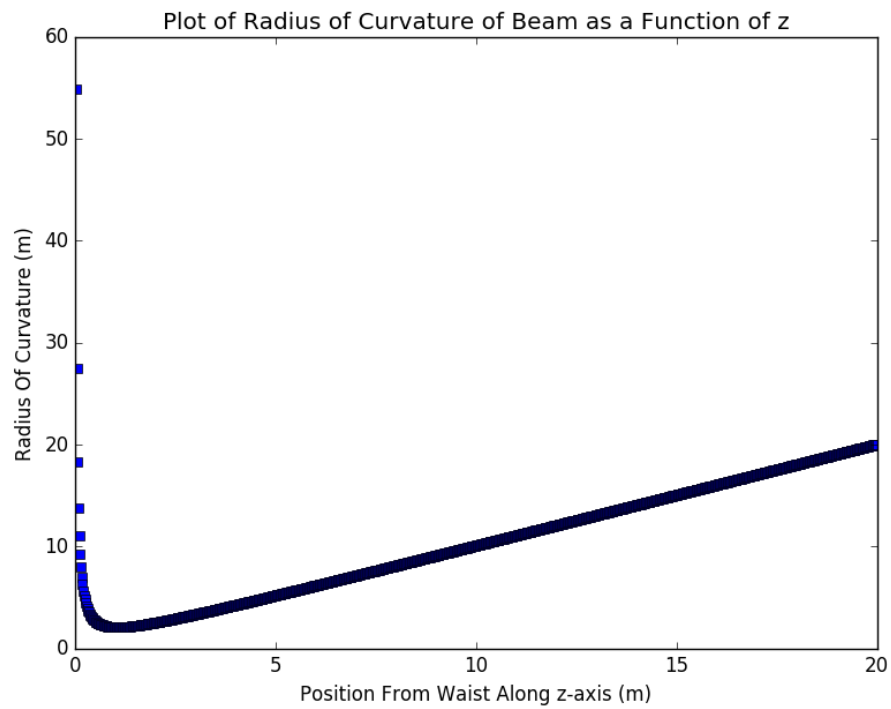
Figure 2.4: Plot of beam radius of curvature, R, as a function of z where $w_0 = 7.74$ mm and frequency $= 76.5$ GHz. At values close to the beam waist, $z = 0$, the radius of curvature becomes infinite
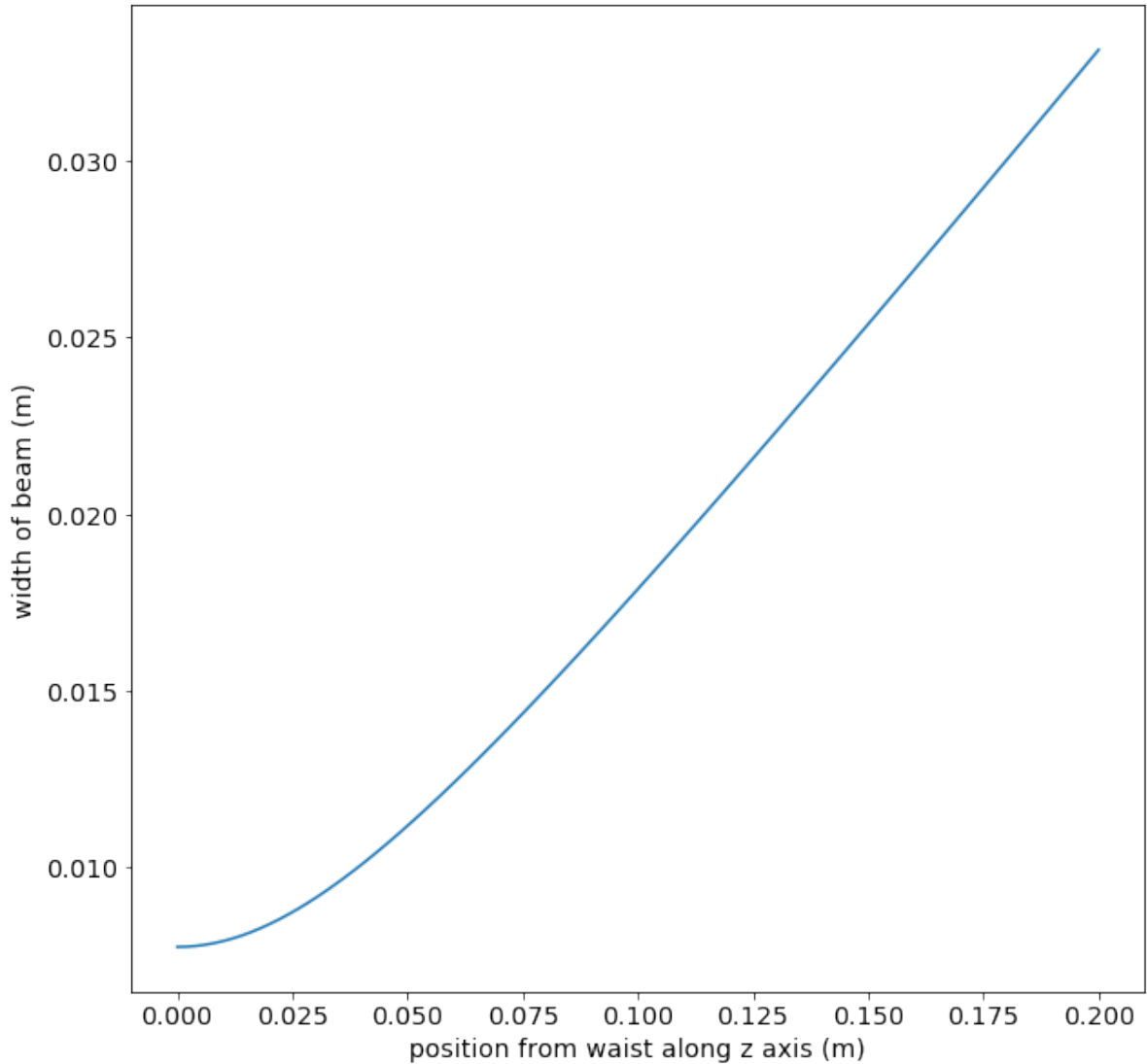
Figure 2.5: Plot of beam width, w, as a function of z where $w_0 = 7.74$ mm and frequency $= 76.5$ GHz. As the beam propagates along the z-axis the beam radius increases slowly. However further along the propagation axis, it approaches a linear expansion.

The confocal distance is also a useful value to describe where the beam is more or less collimated along its propagation axis as there is very little growth by the beam within this distance. At the confocal distance from the beam waist location the radius of the beam is $\sqrt{2}w_0$. However after this the beam's width begins to

increase at a much faster rate.

2.8   Power in a Gaussian Beam

For a Gaussian beam the distribution of the electric field perpendicular to the z-axis is given by:

$$\frac{|E(r,z)|}{|E(0,z)|} = e^{-\left(\frac{r}{w(z)}\right)^2} \tag{2.55}$$

and the power (or intensity) can then be given by:

$$\frac{|P(r,z)|}{|P(0,z)|} = e^{-2\left(\frac{r}{w(z)}\right)^2} \tag{2.56}$$

The relative transverse power density of the beam at a certain radius, r_e, is known as the edge taper, T_e. This is given by;

$$T_e = \frac{|P(r_e)|}{|P(0)|} = e^{\left(-2\frac{r_e^2}{w^2}\right)} \tag{2.57}$$

The edge taper is usually described in decibels (dB) to accommodate a large range. This calculation is a convenient tool when trying to calculate the power remaining within in a beam as it propagates through a train of optical elements within a system. For a typical system the reflectors are designed to be a minimum of 4ω in size which corresponds to a -34 dB edge taper.

2.9   Ray Matrix Analysis

So far, the propagation of a Gaussian beam through free space has been described. In reality, it is necessary to be able to describe the behaviour of a beam as it interacts with a number of optical elements. A simple and efficient method of doing this is the use of ray matrix analysis. Adapted from geometrical analysis, this process uses

the elements of a 2 × 2 matrix to determine the effect of an optical component on the beam parameter, q, and hence on the beam radius, phase radius of curvature and phase slippage. These 2 × 2 matrices are usually denoted as ABCD matrices as A, B, C and D denote the elements within each. The ABCD matrix of an optical element is the same as that used in ray tracing.

Consider an optical system containing a number of optical components. The ABCD matrix technique considers two reference planes for each of these components, the input and the output plane. A ray incident on the input plane can be described by its distance from the optical axis (r_{in}) and the angle it makes with the optical axis (its slope, r'_{in}). After travelling a further distance through the component it is transformed into another ray (position r_{out}, slope r'_{out}).
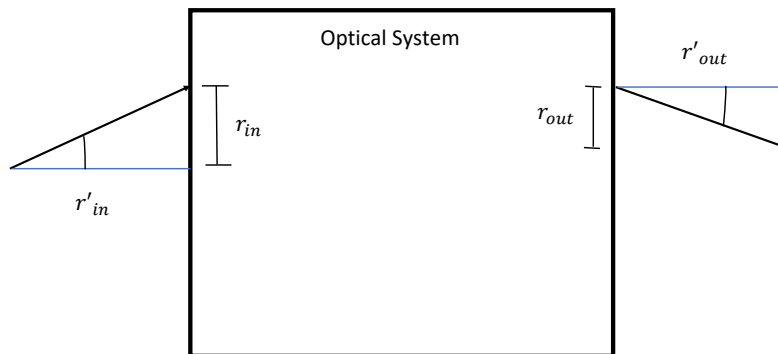

Figure 2.6: The ray matrix formalism that considers the input and output ray location (r_{in}, r_{out}) and slope (r'_{in}, r'_{out}).

The output ray's slope and position depend in some way on the input slope and position:

$$r_{out} = Ar_{in} + Br'_{in}$$

$$r'_{out} = Cr_{in} + Dr'_{in}$$

(2.58)

or, written as a matrix equation:

$$\begin{bmatrix} r_{out} \\ r'_{out} \end{bmatrix} = \begin{bmatrix} A & B \\ C & D \end{bmatrix} \cdot \begin{bmatrix} r_{in} \\ r'_{in} \end{bmatrix}$$

(2.59)

where A, B, C, D are characteristic of a particular component or set of components.

For a propagating beam, the radius of curvature can be described as $R = \frac{r}{r'}$ and equation 2.59 can be simplified to:

$$R_{out} = \frac{A.R_{in} + B}{C.R_{in} + D}$$

(2.60)

Furthermore, this equation can be used to model changes in the complex beam parameter q (also called the complex radius of curvature) using the following equation for quasi-optical systems:

$$q_{out} = \frac{A.q_{in} + B}{C.q_{in} + D}.$$

(2.61)

The complex beam parameter of a Gaussian beam undergoes changes similar to the evolution of the radius of curvature of a geometrical source. Using this method, the significant characteristics of a beam can be easily found at any plane within the quasi-optical system once the ABCD matrix for its components is known. Once q is found, the equations for solving for the beam radius, w, and radius of curvature, R, of the beam can be found from equation 2.20.

$$w = \sqrt{\frac{\lambda}{\pi Im\left(\frac{-1}{q}\right)}} \tag{2.62}$$

$$R = \left[Re\left(\frac{1}{q}\right)\right]^{-1}. \tag{2.63}$$

The phase slippage, $\Delta\phi_0$, in this case defined as the difference between the phase slippage of the input and output beam, is found from:

$$\Delta\phi_0 = -arg\left[A + B\frac{1}{q_{in}}\right]. \tag{2.64}$$

A significant benefit of ABCD matrices is that they allow for a quick and efficient method of calculating a beam's interaction with optical elements within a quasi-optical system. Each component of the system has its own matrix to represent it. An overall matrix for a system can be calculated by multiplying a sequence of separate matrices for each stage in the system. The order of this multiplication is the right most matrix of the product is that of the first component the beam interacts with. Table 2.1 lists the matrices for some of the more common optical components.

Element	Matrix	Description
Free Space Propagation	$\begin{bmatrix} 1 & d \\ 0 & 1 \end{bmatrix}$	d is the distance propagated
Thin Lens	$\begin{bmatrix} 1 & 0 \\ \frac{-1}{f} & 1 \end{bmatrix}$	f is the focal length of the lens
Reflection from a Flat Mirror	$\begin{bmatrix} 1 & 0 \\ 0 & 1 \end{bmatrix}$	Mirror is lying perpendicular to beam's propagation axis
Reflection from a Curved Mirror	$\begin{bmatrix} 1 & 0 \\ \frac{-2}{R} & 1 \end{bmatrix}$	R is the radius of curvature of the mirror where $R > 0$ for a convex mirror
Refraction at a Flat Interface	$\begin{bmatrix} 1 & 0 \\ 0 & \frac{-n_1}{n_2} \end{bmatrix}$	Here n_1 is the refractive index of initial surface and n_2 is refractive index of final surface
Refraction at a Curved Interface	$\begin{bmatrix} 1 & 0 \\ \frac{n_1-n_2}{Rn_2} & \frac{n_1}{n_2} \end{bmatrix}$	n_1 and n_2 are the same as that of a flat interface, R is the radius of curvature

Table 2.1: List of matrices for common optical system elements

Figure 2.7 depicts a simple example of an optical system. The beam originates at the left plane of the image interacting with two lenses before it reaches the output plane. The free space propagation distances (d_n) and lens focal lengths (f_n) are indicated. The overall system matrix is the product of each individual matrix (equation 2.65).

$$M = \begin{bmatrix} 1 & d_3 \\ 0 & 1 \end{bmatrix} \begin{bmatrix} 1 & 0 \\ \frac{-1}{f_2} & 1 \end{bmatrix} \begin{bmatrix} 1 & d_2 \\ 0 & 1 \end{bmatrix} \begin{bmatrix} 1 & 0 \\ \frac{-1}{f_1} & 1 \end{bmatrix} \begin{bmatrix} 1 & d_1 \\ 0 & 1 \end{bmatrix} \tag{2.65}$$

The overall system matrix found by multiplication is:

$$M = \begin{bmatrix} 1 - \frac{d_3 + d_2(1 - \frac{d_3}{f_2})}{f_1} - \frac{d_3}{f_2} & d_3 + d_2(1 - \frac{d_3}{f_2}) + d_1(\frac{1 - d_3 + d_2(1 - \frac{d_3}{f_2})}{f_1} - \frac{d_3}{f}) \\ \frac{\frac{d_2}{f_2} - 1}{f_1} - \frac{1}{f_2} & 1 - d_1(\frac{1 - \frac{d_2}{f_2}}{f_1} + \frac{1}{f_2}) - \frac{d_2}{f_2} \end{bmatrix}. \qquad (2.66)$$

which if $d_1 = f_1$, $d_2 = f_1 + f_2$ and $d_3 = f_2$ (see discussion on Gaussian beam telescopes later) reduces too:

$$M = \begin{bmatrix} \frac{-f_2}{f_1} & 0 \\ 0 & \frac{-f_1}{f_2} \end{bmatrix}. \qquad (2.67)$$
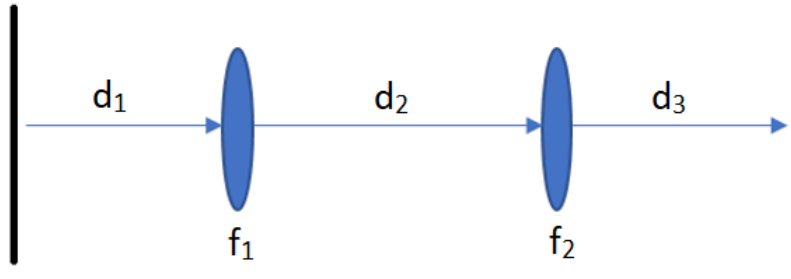
Figure 2.7: d_1,d_2 and d_3 are propagation distances through free space while f_1 and f_2 are the focal lengths of two lens.

The Onsala 3 mm and 4 mm channel use a similar setup to figure 2.7 as the beam propagates from the sub reflector up to a mirror, followed by further propagation to another mirror and finally propagates to the feed horn.

2.10 The Gaussian Beam Telescope

In this thesis, a method of beam manipulation using a Gaussian beam telescope is used to map a beam waist from one point to another further along its propagation path. This following section aims to give a brief description of this process.

2.10.1   Transformation of a beam with a single lens

From the previous section, we can see that the interaction of a Gaussian beam with a lens allows for the phase of a beam to be transformed. As we have seen, as a beam propagates its beam waist expands. On interaction with a lens, a beam will be focussed towards its waist position. This can be seen in figure 2.8:
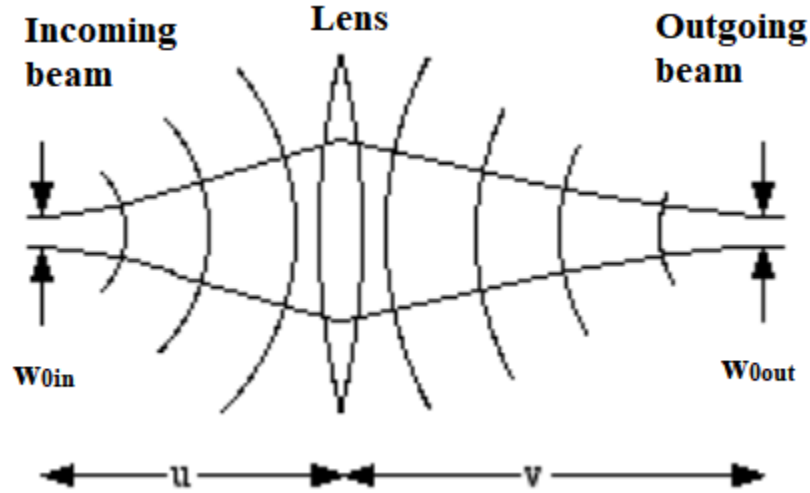
Figure 2.8: Here the incoming beam passes through the lens and it starts to compress towards an output beam waist.

If we consider the situation in figure 2.8, where u is the distance of the input beam waist from the lens, focal length f_1, and v is the output beam waist distance from the lens then

$$\frac{w_{oout}}{w_{0in}} = \frac{1}{[(\frac{u}{f} - 1)^2 + \frac{z_c^2}{f_2}]^{\frac{1}{2}}} \tag{2.68}$$

and

$$\frac{v}{f} = 1 + \frac{\frac{u}{f} - 1}{(\frac{u}{f} - 1)^2 + \frac{z_c^2}{f_2}}. \tag{2.69}$$

In the specific case where $u = f$ then the output beam waist is also at $v = f$ and

$$w_{0out} = \frac{\lambda f}{\pi w_{0in}}.$$ (2.70)

2.10.2 Transformation of a Beam with a Gaussian Beam Telescope

Now, if we introduce a second lens, of focal length f_2, and place it a distance equal to the sum of their focal lengths away from the first lens, it is an arrangement known as a Gaussian Beam Telescope (Figure 2.9)
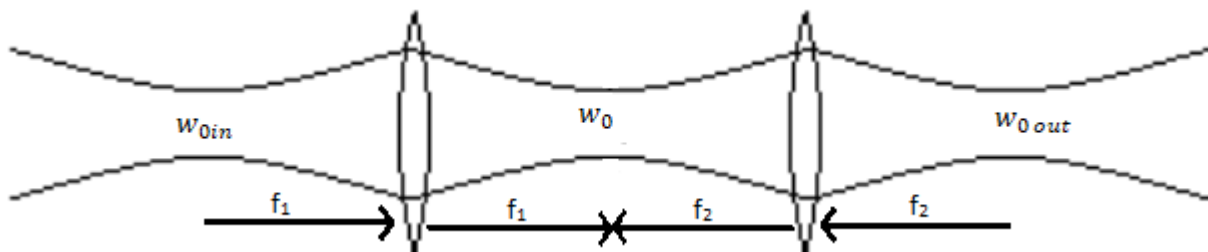
Figure 2.9: The incident beam, whose waist is positioned at the focal point of the first lens results in a waist positioned at the output focal length. This coincides with the focal length of the second. The output waist of the beam is found again at a distance equal to the focal length from the second lens.

The beam waist after the second lens is given by

$$w_{0out} = \frac{f_2}{f_1} w_{0in}$$ (2.71)

and is wavelength independent. The position of the output waist, v, depends only on u and the focal lengths:

$$v = \frac{f_2}{f_1}(f_1 + f_2 - \frac{f_2}{f_1}u)$$ (2.72)

and if we set $u = f_1$ then $v = f_2$ as in figure 2.9 regardless of wavelength. This can be a very useful property and it is used later in Chapter 3 of this thesis as a solution to the extension of a beam's path through a telescope system.

2.11 Generalized Reflector Antenna farm Analysis Software Package (GRASP)

An example of the limitations of GBMA used in conjunction with ray matrices is that when calculating the interaction of a beam with a mirror, the mirror is treated like an on-axis thin lens. More sophisticated software can be used to investigate situations where mirrors are off-axis or beams are not paraxial. A common technique for describing the interaction of a beam with an optical system is Physical Optics (PO)[Smith, 2013]. This technique solves Maxwell's equation for a beam at a certain plane and allows for a description of the full electromagnetic field vector at each point. GRASP is an industry standard software package that employs this method of analysis. The increased accuracy comes at the expense of computation time, however, and often an initial design is first carried out using Gaussian beam modes before being accurately analysed with PO.

2.11.1 Physical Optics

PO in GRASP can be considered as a three step procedure. The first step is to calculate the surface currents that are induced on a scatterer by a source field, then the next step is to calculate the fields radiated by these currents and finally the source and scattered fields are summed together to calculate the total field:

$$E_{tot} = E_i + E_{sc} \tag{2.73}$$

The first step, calculating the surface currents, can be difficult and so PO makes the assumption that the surface current at a specific point on a curved (assumed perfectly conducting) scatterer is the same as that on a planar scatterer if it were tangent to the surface at that point. This PO approximation is accurate so long as the radius of curvature of the surface is large compared to the wavelength of the

incident beam. The electric current induced on a plane, perfectly conducting surface by an incident field is given by:

$$\vec{J} = 2\hat{n} \times \vec{H}_{inc} \tag{2.74}$$

where $\vec{J}$ is the induced electric current, H_{inc} is the incident magnetic field and $\hat{n}$ is the unit surface normal (directed outward from the illuminated side of the scatterer). In GRASP, PO also makes the assumption that the current at any point on the scatterer that is not illuminated by the incident field is zero. For simple surface shapes, PO in GRASP is often used for surfaces with diameters down to five wavelengths across.

The radiated electric and magnetic field are then calculated from the induced and magnetic currents by first calculating vector potentials as follows:

$$A(\vec{r}) = \frac{\mu}{4\pi} \int_{surf} \vec{J}(r') \frac{e^{-jkr}}{R} ds' \tag{2.75}$$

$$F(\vec{r}) = \frac{\epsilon}{4\pi} \iint_{surf} M(\vec{r}') \frac{e^{-jkR}}{R} ds' \tag{2.76}$$

where $\vec{r}$ is the local observation point and $\vec{r}'$ runs over the surface of integration and $R = |r - r'|$. A is the magnetic vector potential, F is the electric vector potential (and for a perfect conductor $M(\vec{r}') = 0$). Finally we get:

$$E = -jw(F(\vec{r}) + \frac{1}{w\mu\epsilon}\nabla(\nabla.F(\vec{r}))) - \frac{1}{\epsilon}\nabla \times A(\vec{r}) \tag{2.77}$$

$$H = -jw(A(\vec{r}) + \frac{1}{w\mu\epsilon}\nabla(\nabla.A(\vec{r}))) - \frac{1}{\epsilon}\nabla \times F(\vec{r}) \tag{2.78}$$

The integrals over the scatterer surface are carried out numerically and calculation accuracies depend on the sample size chosen. Further details on how the

calculations are carried out can be found in the GRASP technical description [TI-CRA, 2013].

2.11.2   Physical Theory of Diffraction

The PO approximation is an effective tool for calculating the currents induced on a scatterer but it is derived from those for an infinite plane surface, and may not be accurate near the edges of the scatterer. To include the interactions of a field at the edges of a scatterer, a method called the Physical Theory of Diffraction (PTD) is used. This technique approximates the currents at the edge by calculating the induced currents on an infinite perfectly conducting half plane illuminated by the wave. The PTD technique in GRASP calculates these edge currents along the illuminated edge of the scatterer for incremental surface area strips. Depending on the surface, GRASP uses infinite incremental strips for reflectors while a finite number are used for flat planes [Johansen, 1996]. Details are given in the GRASP technical description [TICRA, 2013].

PTD is a useful tool when the scatterer being modelled causes a moderate degree of truncation. In this case when combined, PTD and PO allow a user to get a much more accurate calculation of the output field from a scatterer.

2.11.3   Generating a System in GRASP

GRASP uses two main file types when a system is created within it. These are TI-CRA Object Repository (*.tor) and TICRA Command Input (*.tci). *.tor files are used to store the information about the various objects defined within the GRASP project while the *.tci contains the calculations that the project must carry out. The creation of a system within GRASP is carried out using two Graphical User Interfaces (GUI) that are: the pre-processor and post-processor. The pre-processor

assists the user in setting up the initial geometry of the telescope system being used. This allows the user to visualise the system they are developing before any calculations are carried out. GRASP offers a range of options for the user to design scatterers such as defining conic sections, using quadratic equations and tabulated surfaces.

2.11.4   Sources within GRASP

Before a system can be analysed, a source of radiation must be defined. GRASP offers a number of different source origin types to choose from. In this section, two types of sources will be described, those being: Gaussian Beams and Hybrid Mode Conical Horns.

Gaussian Beam

The Gaussian beam source is a point source that radiates a beam with Gaussian taper that satisfies Maxwell's equations in the near and far field.

The point source of the field is taken as a Huygens source directed along the z-axis. This consists of both an electrical and magnetic dipole in the x and y axes respectively. The equation for the electric field from such a Huygens source at a large distance r is:

$$\vec{E}(r,\theta,\phi) = E_0 \frac{e^{-jkr}}{r}(1 + \cos\theta)(cos\phi\hat{\theta} - \sin\phi\hat{\phi}). \qquad (2.79)$$

The GRASP technical description [TICRA, 2013] describes how a complex point source can be used to generate a Gaussian beam. Figure 2.10, depicts the Gaussian beam properties.
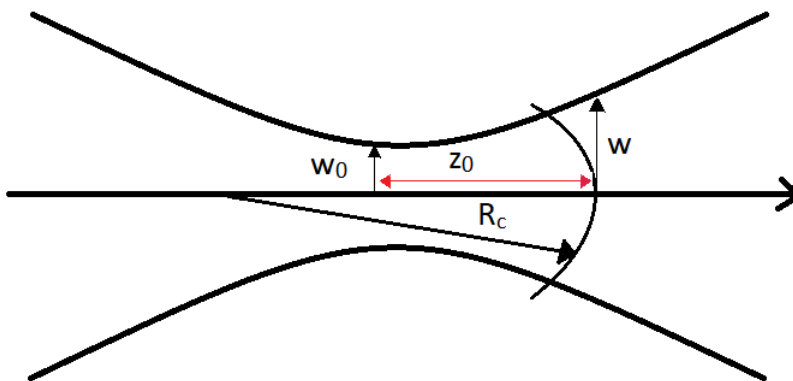
Figure 2.10: Example of the near field definitions of a Gaussian beam, here w_0 as usual represents the beam waist radius, z_0 is the distance from the waist to a specified wave front, R_c represents the radius of curvature of the wave front and w is the width of the beam at the front. The polarization of Gaussian beams are generally considered as linear and orthogonal to the axis of propagation.

Hybrid Mode Conical Horn

This source models a feed that is based on a standard corrugated conical horn. The user inputs the semi-flare angle of the horn, the waveguide radius and the aperture radius. GRASP supports the hybrid modes HE_{mn} ($1 \leq m \leq 8$) and EH_{mn} ($2 \leq n \leq 8$) and the conical modes TE_{0n} ($1 \leq n \leq 8$) and TM_{0n} ($2 \leq n \leq 8$) where m is the azimuthal mode index and n is the radial mode index. Due to the high frequency cut off of these horns, EH_{m1} and TM_{01} are not included.

2.11.5   Reflectors

In designing a system, reflectors must commonly be modelled. To do this in GRASP requires two pieces of information: a defined surface shape and a rim. The surface object describes the surface of the reflector in three-dimensional space and the rim describes the edge of the reflector.

GRASP contains a library of pre-defined quadric surfaces such as ellipsoids and paraboloids. These can also be custom designed by the user using specific charac-

teristics of the surfaces such as the vertex distance or focal length. They can also be defined by using second order polynomials or by importing grids of a tabulated surface. In this thesis, all three definition types (A-C below) are used.

A) Defining a Surface Using Second-Order Polynomials

Elliptical mirrors are used to map a beam waist from one plane to another. To create such an elliptical mirror an ellipsoid must be defined (ellipse rotated around one of its axes). The required focal length of the ellipsoidal section used is related to the input and output beam radii of curvature by:

$$\frac{1}{f} = \frac{1}{R_1} + \frac{1}{R_2}. \tag{2.80}$$

Here f is the focal length of the ellipse while R_1 and R_2 represent the input and output radius of curvature of a beam respectively. Figure 2.11 shows an example of these.

The focal length of a mirror can be initially found using ABCD matrices. Say we have a known source, with a known waist and waist position, placed at one of the focal points of the elliptical mirror. The beam travels a certain distance towards the mirror before it strikes it. The radius of curvature of the beam when it strikes the surface is the value R_1. The beam is then directed towards the second focal point of the elliptical mirror and travels a certain distance before reaching it. (Just after reflection by the mirror the new beam phase radius of curvature is R_2.)

Figure 2.11: Parameters of an ellipse
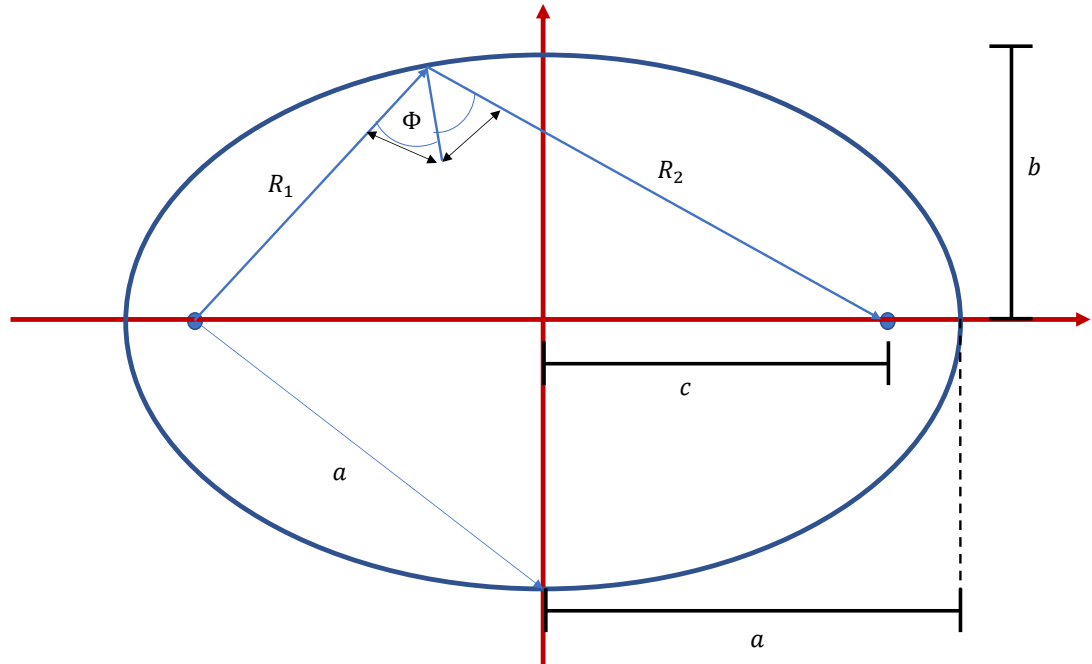
An ellipse's semi-major and semi-minor axis (a and b respectively) are related to R_1 and R_2 by:

$$a = \frac{R_1 + R_2}{2} \tag{2.81}$$

$$b = \sqrt{R_1 R_2} \cos(\phi) \tag{2.82}$$

Here ϕ denotes the angle of throw (see Figure 2.11). Using a and b the inter-focal distance ($2c$), eccentricity (e) and the radius of curvature of the ellipsoid (R_e) can

be found with:

$$c = \sqrt{a^2 - b^2} \tag{2.83}$$

$$e = \sqrt{1 - \frac{b^2}{a^2}} \tag{2.84}$$

$$R_e = a(1 - e^2) \tag{2.85}$$

Once these parameters of the ellipse have been calculated a polynomial equation can be constructed. This takes the form of:

$$\frac{x^2 + y^2}{2R_e} + \frac{(1 - e^2)z^2}{2R_e} + z = 0 \tag{2.86}$$

Using the polynomials coefficients, the surface can be implemented into GRASP as a 2nd order polynomial and from here can be decentered and rotated around its axes as required.

B) Conic Surfaces

Second Order polynomials can be used to create many different shapes such as ellipsoids, paraboloids and hyperboloids, however GRASP also offers other ways to create these more simple conic sections. The following list outlines the parameters each shape definition requires in order to construct the scatterer shape.

- **Paraboloid**

  This surface is constructed by rotating a parabola around its axis. GRASP requires the user to input the vertex position and the focal length of the parabola. A parabolic reflector can direct all incoming rays of light, parallel to its axis of symmetry.

- **Hyperboloid**

To define a hyperboloid the user inputs the shape's vertex distance (distance between the two vertices) and its focal length. A hyperbolic reflector is used for directing rays that go through one of its focii towards the other.

- **Ellipsoid**

  To construct an ellipsoid scatterer, GRASP requires the user to input the vertex distance (distance between the two vertices along the major axis $= 2a$), the focal length of the ellipsoid and also the axis angle. This axis angle is used to position the desired section of the reflector along the beam path.

C) Tabulated Surfaces

A surface can be defined using tabulated surfaces in GRASP and this can be carried out in a number of ways. A tabulated surface can be defined using a list of x, y and z coordinates for points on a surface. The program takes these points and fits a surface between them. The different possibilities that are available are:

- **Regular XY-Grid**

  This surface is defined using a set of tabulated z values in a regular xy grid. The program uses cubic interpolation to fill in the surface between these points.

- **Spline Surface**

  To define spline surfaces, a file is read into GRASP containing coefficients from a B-spline function. The x and y limits are defined in the file and GRASP uses these to evaluate z values from the spline expansion.

- **Zernike Surface**

  A Zernike surface is defined using a weighted sum of Zernike polynomials. Depending on the number of polynomials that are used, complex surface shapes can be described.

- **Rotationally Symmetric**

  For rotationally symmetric surfaces, a tabulated data profile is input to GRASP where data points are given as z values along a radial surface cut.

- **Irregular XY-Grid, Triangulation**

  Irregular grids allow the user to input a number of coordinates that GRASP knits together using triangulation such that from one point a triangular surface is created using the two nearest to it. These coordinates are given as (x,y,z) from a data file.

- **Irregular XY-Grid, Pseudo Splines**

  This method is similar to the irregular XY-grid, Triangulation except instead a quintic pseudo spline algorithim is used to generate a surface between points.

2.12   Summary

In this chapter I have described the theory behind the two optical analysis methods most often used in this thesis: Gaussian Beam Mode Analysis (GBMA) and the more accurate Physical Optics (PO). In the case of PO I have also outlined the functionality of the software package GRASP which I have used for the PO modelling. GBMA is straightforward and quick to carry out analytically and I wrote my own code to do this in the mathematical software package, Wolfram Mathematica. When describing these techniques I have concentrated on the aspects that are most relevant to the work in this thesis.

Chapter 3

Re-Design and Analysis of the Onsala 3-mm Receiver

In this chapter the methods used for the design and analysis of millimetre wave telescope systems, introduced in Chapter 2, are applied. I use as an example the 4 mm (67-87 GHz) channel of the 20 m telescope at the Onsala Space Observatory [Cumming and Nystås, 2014]. Using these techniques a feasibility study is carried out on the current 3 mm (85 - 116 GHz, W band) channel to investigate whether simultaneous observations in the K band (18 GHz - 27 GHz) and W band (85 - 116 GHz) would be possible. The proposed solution to this would be to push the receiver back 600 mm, this is further explained later in section 3.2.2. The Department of Experimental Physics of Maynooth University has close ties with Onsala, with both MSc and PhD students having carried out research on the development of the 20 m telescope receivers.

This chapter is divided into four sections. Firstly, a brief introduction to the Onsala Space Observatory and its telescopes is given; this is followed by a description of the initial analysis of the 4 mm system which is then extended to a feasibility study of the 3 mm channel. The chapter finishes with the analysis of the 3 mm

channel using Gaussian beam modes and the physical optics package in GRASP.

3.1   The Onsala Space Observatory

The Onsala Space Observatory (OSO) is the Swedish national facility for Radio Astronomy founded in 1949 by Olof Rydbeck and its location can be seen in figure 3.1. The Department of Space, Earth and Environment sciences in Chalmers University hosts OSO and operates it on behalf of the Swedish Research Council. OSO is part of a number of international projects such as SKA (Square Kilometer Array)[SKA] and the European Very Large Baseline Interferometry Network (VLBI) [ESA], along with Nuffield Radio Astronomy Lab., Jodrell Bank (UK), Max-Planck-lnstitute for Radio Astronomy (Germany) and others, see [Hirabayashi et al., 1998]. Onsala hosts two radio frequency telescopes, the 20 m and the 25 m.

Figure 3.1: Location of the Onsala Space Observatory in Sweden [Google, 2017]

The 20 m and 25 m telescopes of OSO are both of a Cassegrain design (reflecting

telescope comprised of two mirrors placed along the optical axis: a large primary and a smaller secondary). The range of frequencies that it is possible to observe with these two telescopes extends from 0.8 GHz to 116 GHz. The 25 m telescope (figure 3.2) receiver operates from 0.8 GHz to 6.7 GHz while the 20 m telescope (figure 3.3) receiver operates from 2.2 GHz to 116 GHz. The receivers used by the 25 m telescope for each frequency range are listed in Table 3.1

Figure 3.2: OSO's 25 m telescope [Lindqvist, 2014].

Frequency Range (GHz)	Receiver Temperature (K)	Receiver Type	Polarization
0.8 - 1.2	100	HEMT amplifier	Dual
1.2 - 1.8	30	HEMT amplifier	Dual
4.5 - 5.3	80	FET amplifier	Dual
6.0 - 6.7	80	HEMT mixer	Dual

Table 3.1: Table showing the operating temperatures and receivers for the 25 m telescope [Chalmers University, 2014].

The 20 m telescope at Onsala is housed inside a radome to protect it from the elements (see Figure 3.3). The receivers and their operating temperatures are listed in table 3.2

Figure 3.3: OSO 20 m telescope surrounded by its radome [Cumming and Nystås, 2014]

Frequency Range (GHz)	Reciever Temperature (K)	Receiver Type	Polarization
2.2 - 2.4	60	HEMT amplifier	Single
8.2 - 8.4	80	HEMT amplifier	Dual
18.0 - 26.0 **(K band)**	30	HEMT amplifier	Dual
26.0 - 36.0	50	HEMT amplifier	Single
36.0 - 49.8	50	HEMT amplifier	Dual
67.0 - 86 (4 mm)	50-60	HEMT amplifier	Dual
85 - 116 (3 mm)**(W band)**	50-60	SIS mixer	Dual

Table 3.2: Table showing the operating temperatures and receivers for the 20 m telescope [Chalmers University, 2016].

3.1.1   The Optics of the 20 m Telescope

As previously stated, the 20 m telescope has a Cassegrain design where there is a small convex sub-reflector in front of the concave primary mirror. The layout of this can be seen below in figure 3.4
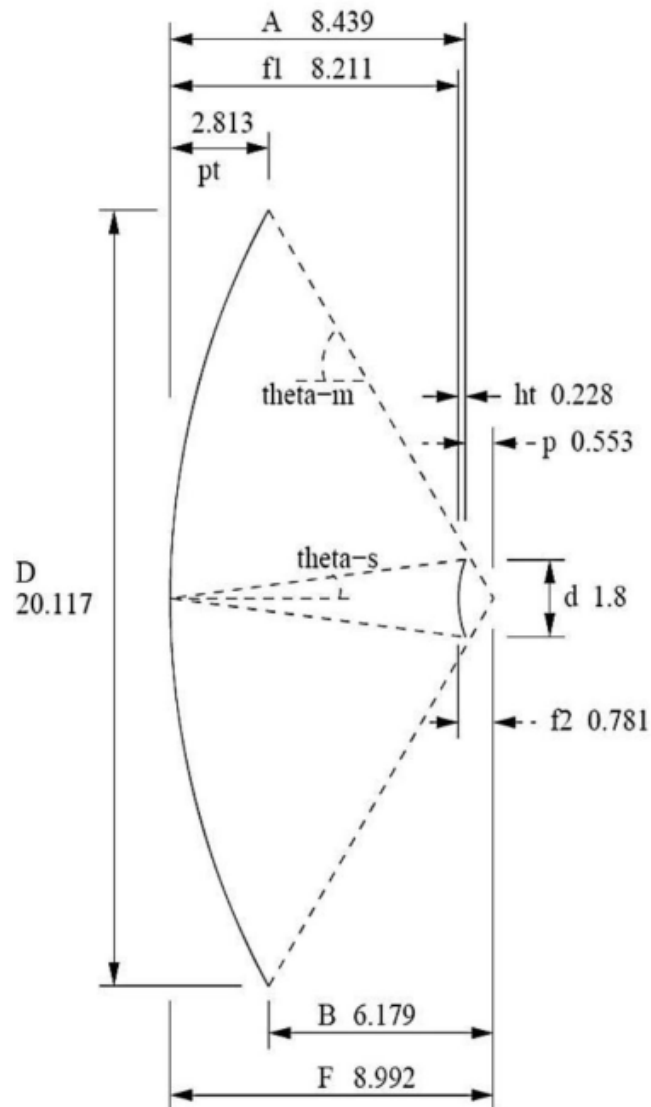
Figure 3.4: Plan of the primary mirror and sub-reflector for the 20 m Cassegrain telescope where values are in meters [Nyström, 2011].

After reflection from the primary mirror and the sub-reflector, incident radiation is directed towards the receivers. The beam interacts with a number of stops before it enters the receiver cryostat. A basic layout of the path that the beam takes can be seen in figure 3.5 (note that this is an equivalent, mainly on-axis, system and not the actual layout of the current system).
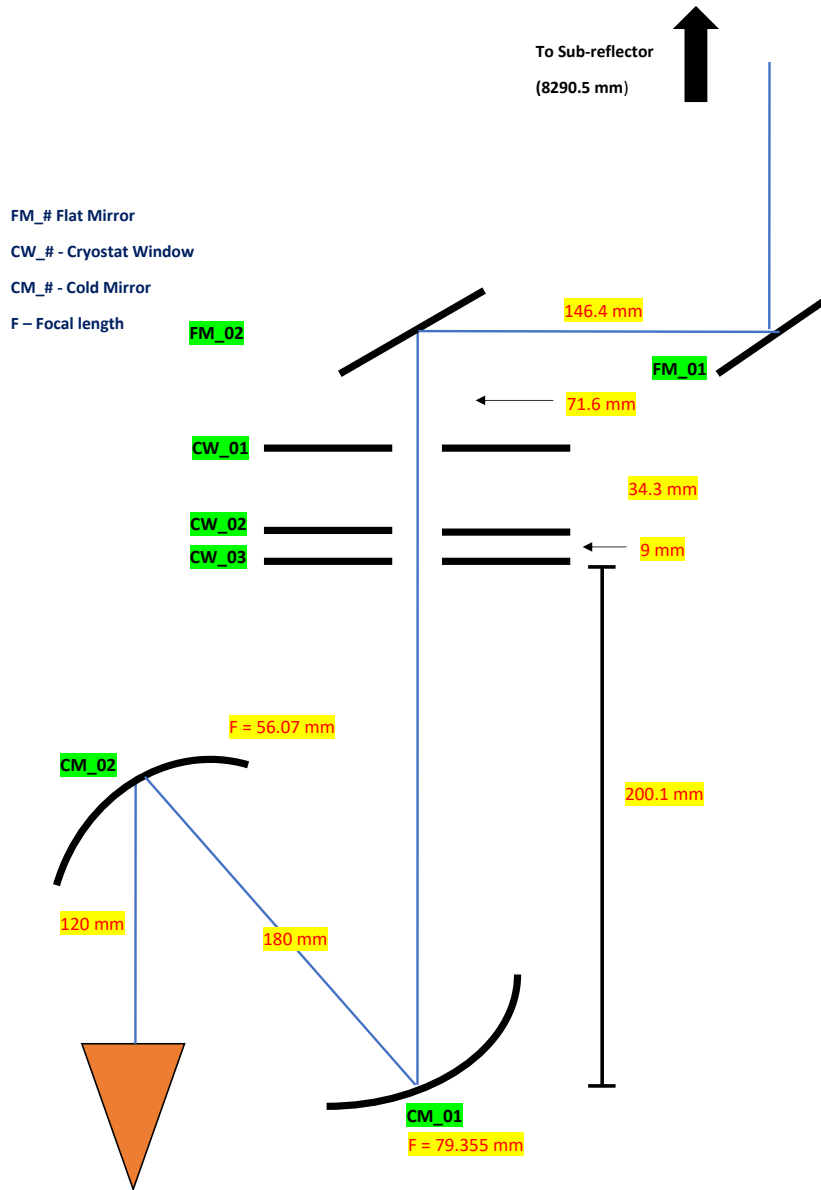
Figure 3.5: Simple layout of beam path towards the 4 mm receiver. The distances between each component are marked in yellow while the components themselves are marked in green.

3.1.2   The 3 mm and 4 mm Receivers of the 20 m Telescope

As listed in Table 3.2, the 20 m telescope is equipped with a number of receivers. In the case of the 3 mm and 4 mm channels, they are mounted within the same cylindrical cryostat. These channels are used independently using an on-axis/off-axis optical switch to load the channel to be used for observations. This optical switch consists of a system of flat mirrors which allows the beam to be directed into the preferred channel. Figure 3.6 shows a CAD drawing of the dual cryostat.
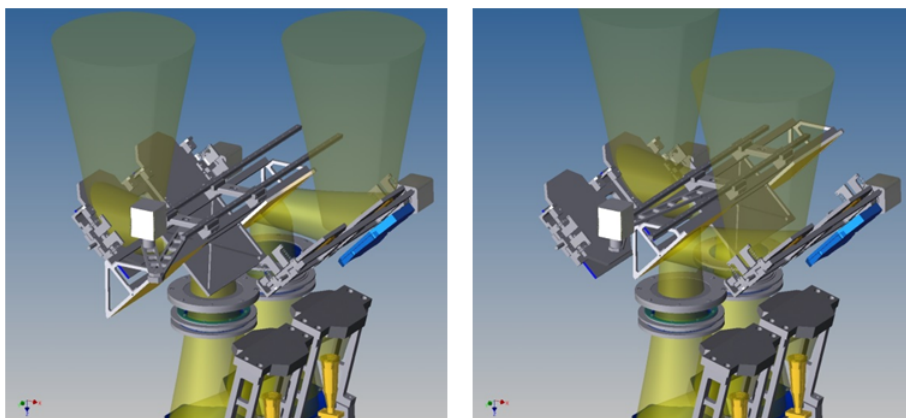

Figure 3.6: CAD model of cryostat [Whale, 2014] with left and right showing the beam switched to each channel.

The beam from the telescope interacts with two flat mirrors before entering the cryostat. From figure 3.5 the first flat mirror (FM01) is at a distance of 8290.5 mm from the cassegrain sub-reflector, the second flat mirror (FM02) is a further 146.4 mm away and then the beam propagates another 71.6 mm to the cryostat window. The two flat mirrors are only used for simply directing the beam and are not intended to change the beam's characteristics. The aperture diameters of each of these components can be seen in table 3.3. The diameters were chosen to be $5w$, where w is the Gaussian beam radius of the longest wavelength beam at the particular component.

Optical Stop	Diameter
Cold Mirror 2	140 mm
Cold Mirror 1	160 mm
Cryostat Window 3	95 mm
Cryostat Window 2	92 mm
Cryostat Window 1	91 mm
Flat Mirror 2	110 mm
Flat Mirror 1	110 mm
Subreflector	1.8 m

Table 3.3: Stop diameters

The two ellipsoidal mirrors that are used for coupling the beam to each receiver feedhorn were chosen for a number of reasons. There was only a small amount of space available for optical components within the cryostat and using two off-axis ellipsoidal mirrors allowed for a compact design as well as low levels of cross-polarization [Walker, 2016].

Each channel of this assembly has its own observational goal which will be described below.

3 mm receiver

The main observational goal of the 3 mm channel is molecular spectroscopy at frequencies between 85 GHz and 116 GHz. It is also used to participate in Very Large Baseline Interferometry (VLBI) observations in tandem with the Global VLBI Millimetre Array (GVMA) [Belitsky et al., 2015]. The table below outlines some of the spectral lines viewable with the 3 mm channel.

Substance	Central Frequency (GHz)	Bandwidth (GHz)
Methyl acetylene (CH$_3$CCH)	85.5	85.41 - 85.59
Deuterated Ammonia (NH$_2$D)	85.926	85.84 - 86.01
Carbon monosulphide (CS)	97.981	97.65 - 98.08
Sulphur monoxide (SO)	99.3	99.2 - 99.4
Methyl cyanide (CH$_3$CN)	110.38	110.27 - 110.49
Carbon monoxide (C$_{17}$O)	112.359	112.25 - 112.47

Table 3.4: Some of the spectral lines that are observable with the 3 mm channel [IAU, 1991].

4 mm receiver

The observational goal for the 4 mm receiver is also spectroscopy, more specifically the observations of deuterated molecules. An example of these molecules can be seen in Table 3.5.

Substance	Frequency (GHz)	Bandwidth (GHz)
Deuterated formylium (DCO$^+$)	72.039	71.97 - 72.11
Deuterium cyanide (DCN)	72.415	72.34 - 72.49
Deuterated water (HDO)	80.578	80.50 - 80.66
Deuterated Ammonia (NH$_2$D)	85.926	85.84 - 86.01

Table 3.5: Some of the spectral lines that are observable with the 4 mm channel [IAU, 1991]

3.2 Analysis of current 4 mm Channel and Possible Re-Design of the 20 m Telescope 3 mm Receiver

3.2.1 Analysis of the 4 mm Channel

The OSO 20-m currently has receivers operating in a 4-mm and a 3-mm channel. In this chapter I will investigate whether the 3-mm could be re-designed in order to also allow simultaneous obervations in K-band. The 3-mm channel shares much of its optics with the 4-mm channel and since the details of the 4-mm optical model are available to me, I will begin by analysing the beam width and truncation level of the existing OSO 4 mm channel (to compare with known results), and following this, the same techniques will be applied to the feasibility test for a proposed modification of the existing 3 mm channel. As is usual with this type of analysis, the principle of reciprocity is used and I consider the detector as an emitter and follow the beam from the receiver horn, out through the cryostat, the flat mirrors and onto the cassegrain sub-reflector.

Before the beam can be characterised along its path, the beam waist position at each frequency is determined. The beam waist location behind the receiver horn aperture varies with frequency. This distance can be calculated using the equation [Goldsmith, 1998]:

$$\Delta = \frac{R}{1 + (\frac{\lambda R}{\pi w^2})^2}.$$ (3.1)

where w is the beam width at the horn aperture and R is the phase radius of curvature of the beam at the aperture. The size of the beam radius at the waist is given by:

$$w_0 = \sqrt{\frac{w^2}{1 + (\frac{\pi w^2}{\lambda R})^2}}$$ (3.2)

For a scaler (conical/corrugated) feedhorn such as the one used here, the best-fit beam radius at the horn aperture is $w = 0.6435a$, where a is the aperture radius, and the phase radius of curvature R, is the same as the slant length of the horn. For the 4 mm channel $a = 15$ mm and $R = 100$ mm.

Table 3.6 below, gives the waist location behind the horn aperture and its size for the edge and centre frequencies of the 4 mm band.

Frequency (GHz)	Δ (mm)	Waist radius (mm)
67	29.97	8.08
76.5	35.81	7.74
86	41.35	7.39

Table 3.6: Location and size of the beam waist for the start, middle and end frequencies of the 4 mm band.

Knowing the position of the waist behind the horn aperture allows for the propagation distance of the beam to the first mirror for each frequency to be considered when initially investigating the beam size through the system. Tables 3.7 and 3.8 show the change in size of the radius and the phase radius of curvature of the beam as it propagates through each optical stop. These were calculated using the equations outlined in Chapter 2 (2.23, 2.24 and 2.27). There is a small variation (a fraction of a percent) across the band in the Walker design but this was considered acceptable.

Optical Stop (4 mm)	Beam Radius		
	67 GHz	76.5 GHz	86 GHz
Waist within Horn	8.08 mm	7.74 mm	7.4 mm
Cold Mirror 2	27.66 mm	26.31 mm	25.34 mm
Cold Mirror 1	32.15 mm	31.57 mm	31.16 mm
Cryostat Window 3	18.53 mm	17.15 mm	16.14 mm
Cryostat Window 2	18.11 mm	16.68 mm	15.62 mm
Cryostat Window 1	16.77 mm	15.14 mm	13.9 mm
Flat Mirror 2	15.69 mm	13.75 mm	12.24 mm
Flat Mirror 1	20.93 mm	19.24 mm	17.99 mm
Sub reflector	767.75 mm	766.3 mm	765.29 mm

Table 3.7: List of the beam radius at each optical stop and across the 4 mm frequency band

Optical Stop (4 mm)	Phase Radius of Curvature		
	67 GHz	76.5 GHz	86 GHz
Radius at Aperture	100 mm	100 mm	100 mm
At Cold Mirror 2	164.01 mm	170.61 mm	176.42 mm
After Cold Mirror 2	-85.2 mm	-83.52 mm	-82.19 mm
At Cold Mirror 1	98.69 mm	99.87 mm	100.76 mm
After Cold Mirror 1	-405.024 mm	-386.26 mm	-373.6 mm
Cryostat Window 3	-382.26 mm	-315.94 mm	-273.02 mm
Cryostat Window 2	-397.96 mm	-324.5 mm	-277.24 mm
Cryostat Window 1	-520.1 mm	-398.74 mm	-323.32 mm
Flat Mirror 2	4799.6 mm	12.027.4 mm	-17189.7 mm
Flat Mirror 1	347.46 mm	302.93 mm	270.65 mm
Sub reflector	8446.63 mm	8441.52 mm	8438 mm

Table 3.8: List of the phase radius of curvature of the beam at each optical stop and across the 4 mm frequency band.

As the beam travels through each aperture the majority but not all of its power is transmitted. The ratio of the power at the edge of an aperture to that on-axis is known as **edge taper** (equation 2.57) and can be calculated for a Gaussian beam as:

$$T_e(\mathrm{dB}) = -\frac{20}{\ln(10)}\left(\frac{a}{w}\right)^2. \tag{3.3}$$

Here, a is the aperture radius and w is the radius of the beam at the aperture. The edge taper criterion for the 20 m telescope was to be $T_e = -12$ dB at the sub reflector, the table below shows this was achieved for the aperture radii used.

Optical Stop (4 mm)	Edge Taper		
	67 GHz	76.5 GHz	86 GHz
Cold Mirror 2	-55.62 dB	-61.49 dB	-66.30 dB
Cold Mirror 1	-53.79 dB	-55.78 dB	-57.24 dB
Cryostat Window 3	-57.06 dB	-66.6 dB	-75.23 dB
Cryostat Window 2	-56.04 dB	-66.07 dB	-75.33 dB
Cryostat Window 1	-63.96 dB	-78.50 dB	-93.03 dB
Flat Mirror 2	-106.77 dB	-138.98 dB	-175.33 dB
Flat Mirror 1	-59.95 dB	-70.95 dB	-81.18 dB
Sub reflector	-11.94 dB	-11.98 dB	-12.01 dB

Table 3.9: Edge taper of the beam at each stop and across the 4 mm frequency band

The results agree with those published by Walker [Walker, 2016] and are a useful check that the optical model was set up correctly. This same analysis will now be carried out on a proposed re-design of the 3 mm channel of the 20 meter telescope. A further study of the system will also be carried out with GRASP to investigate the beam pattern is affected reflector.

3.2.2 The Re-Design of the 3 mm Channel

The optics for the 3 mm channel, within the cryostat, are the same as that of the 4 mm channel already discussed. Outside the cryostat, the beam from the sub reflector is directed using flat mirrors to the receiver being used. I was asked to investigate whether simultaneous viewing in bands K (18 - 27 GHz) and W (85 - 116 GHz, 3 mm channel) was possible. To do this, the K band beam would have to be folded towards the K-band receivers while the W-band beam would be free to pass through into the existing 3 mm cryostat. To allow for this the 3 mm cryostat would have to be moved 600 mm further away from the flat mirror FM02.

To account for the extra propagation distance that the beam must travel between the flat mirrors and the receiver, an optical system had to be designed so that the beam from the receiver, by the time it gets to the sub-reflector, is the same as it was previously, before the extra distance was introduced. Both the 3 mm and 4 mm channel are frequency independent, and this was to be the case for the re-design.

The Onsala team were also concerned with increasing the efficiency of the channel at the lower end of the frequency band (85 GHz). Since this is also the part of the band where diffraction and truncation effects are greatest, I paid particular attention to the performance of the system at frequencies 84 -88 GHz.

Initially, an attempt to use two off-axis ellipsoidal mirrors (not necessarily in a GBT configuration) to compensate for the extra propagation distance was tried in the same way that Walker [Walker, 2016] designed the CM_01 and CM_02 mirrors. To do this, an optimization routine using an ABCD matrix system was written that varied focal length of both mirrors until the required beam width at the sub reflector was achieved. However, this method did not produce satisfactory results and so it was not deemed possible to achieve a configuration which allowed a reasonable degree of frequency independence at the sub-reflector.

An alternative and effective re-design to compensate for the extra distance was to use two mirrors as a Gaussian beam telescope. The most obvious problem with adding an extra 600 mm of propagation distance was the expansion of the beam. However, using a Gaussian beam telescope it is possible to transmit a beam's waist radius and phase radius of curvature from one plane to another, independent of the frequency. A simple example of this can be seen in figure 3.7. More information on how this works was given in Chapter 2: Gaussian Beam Telescope.
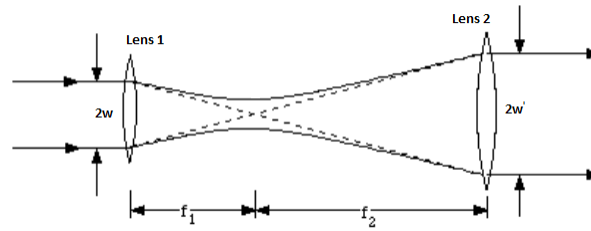
Figure 3.7: Example of a Gaussian beam telescope [Syms and Cozens, 1992]

If the two optical elements in figure 3.7 have the same focal lengths ($f_1 = f_2$) then the beam waist can be imaged from one point along its propagation path to another. The beam can be made narrower or wider if required depending on the ratio of the focal lengths of mirrors used.

Figure 3.8 shows the layout of the proposed plan for the 3 mm channel. Using two mirrors each with a focal length of 300 mm and separated by 600 mm, allows for the radius just after the cryostat windows to be mapped to a position in front of the flat mirrors as if it had not travelled through the extra distance. Because of the off-axis design, the beam travels more than 600 mm extra (due to travelling from the focal plane of both mirrors) but it is the 600 mm along the cryostat axis that is important. The distance between components are highlighted in yellow in figure 3.8.
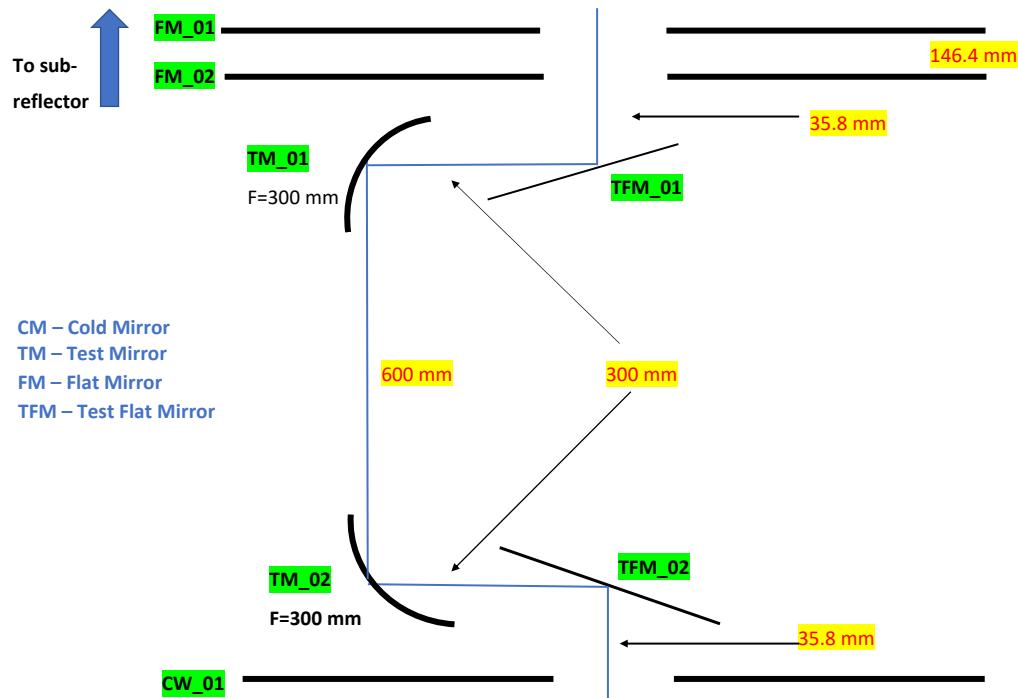
Figure 3.8: Proposed plan for 3 mm channel. The proposed Gaussian beam telescope is composed of the elliptical mirrors TM_01 and TM_02 and the flat mirrors TFM_01 and TFM_02 are used to re-direct the beam to and from them.

3.2.3 Analysis of the 3 mm Re-Design

Again, as with the work done on the 4 mm channel, the proposed 3 mm channel was first analysed using ABCD matrices to calculate the beam's size and phase radius through the system. The position (Δ) and size of the beam waist for a small range of frequencies at the lower end of the band is given in the table below.

Frequency (GHz)	Δ (mm)	Waist size (mm)
84	40.26	7.47
86	41.39	7.39
88	42.51	7.32

Table 3.10: Location and size of waist for start, middle and end frequencies under consideration.

With these starting waist radii and locations, and using ray matrices, the size of the beam along with its phase radius of curvature and edge taper at each component were calculated as previously, and are listed in Tables 3.11, 3.12 and 3.13. The phase radius of curvature before and after each powered mirror is calculated as it is changed by the mirror and used later in the mirror design. The aperture radius of both Gaussian beam telescope test mirrors was set at 2.5 times the 84 GHz radius of the beam at that plane to minimize power loss.

Optical Stop 3 (mm)	Beam Width		
	84 GHz	86 GHz	88 GHz
Waist within Horn	7.47 mm	7.4 mm	7.32 mm
Cold Mirror 2	25.52 mm	25.34 mm	25.17 mm
Cold Mirror 1	31.24 mm	31.16 mm	31.1 mm
Cryostat Window 3	16.33 mm	16.13 mm	15.96 mm
Cryostat Window 2	15.82 mm	15.62 mm	15.43 mm
Cryostat Window 1	14.14 mm	13.9 mm	13.68 mm
Test Flat Mirror 2	12.96 mm	12.69 mm	12.44 mm
Test Mirror 2	27.01 mm	26.61 mm	26.66 mm
Test Mirror 1	32.98 mm	32.88 mm	32.85 mm
Test Flat Mirror 1	12.96 mm	12.69 mm	12.44 mm
Flat Mirror 2	12.53 mm	12.24 mm	11.97 mm
Flat Mirror 1	18.23 mm	17.99 mm	17.77 mm
Sub reflector	765.48 mm	765.29 mm	765.12 mm

Table 3.11: The beam width at each optical stop across the frequency band. The Test mirrors 2 Flat Test mirrors are the added components, see figure 3.8

Optical Stop (3 mm)	Phase Radius of Curvature		
	84 GHz	86 GHz	88 GHz
Radius at Aperture	100 mm	100 mm	100 mm
At Cold Mirror 2	175.26 mm	176.42 mm	177.55 mm
After Cold Mirror 2	-82.45 mm	-82.19 mm	-81.95 mm
At Cold Mirror 1	100.59 mm	100.76 mm	100.91 mm
After Cold Mirror 1	-375.9 mm	-373.6 mm	-371.46 mm
Cryostat Window 3	-280.71 mm	-273.02 mm	-265.91 mm
Cryostat Window 2	-285.69 mm	-277.24 mm	-269.43 mm
Cryostat Window 1	-336.65 mm	-323.32 mm	-311.05 mm
Test Flat Mirror 2	-565.084 mm	-534.17 mm	-506.14 mm
At Test Mirror 2	336.033 mm	328.71 mm	328.91 mm
After Test Mirror 2	-375.9 mm	-371.97 mm	-371.46 mm
At Test Mirror 1	1267.31 mm	1305.94 mm	1311.72 mm
After Test Mirror 1	-375.90 mm	-371.97 mm	-371.46 mm
Test Flat Mirror 1	-565.084 mm	-534.17 mm	-506.14
Flat Mirror 2	-36910.3 mm	-17189.7 mm	-11115.7 mm
Flat Mirror 1	276.66 mm	270.65 mm	265.01 mm
Sub reflector	8438.64 mm	8438 mm	8437.4 mm

Table 3.12: List of the radius of curvature of the beam at each optical stop across frequency band

In order to illustrate the behaviour of the beam through this proposed re-design, w and R were calculated along all positions in the optical system. $w(z)$ and $R(z)$ are shown in figures 3.9 and 3.10. The abrupt changes in radius and phase are due to the presence of powered mirrors. The operation of the Gaussian Beam Telescope, translating w and R along the propagation path, can be clearly seen. Beams at 84, 86 and 88 GHz are shown but are very similar, illustrating the desired frequency independence.
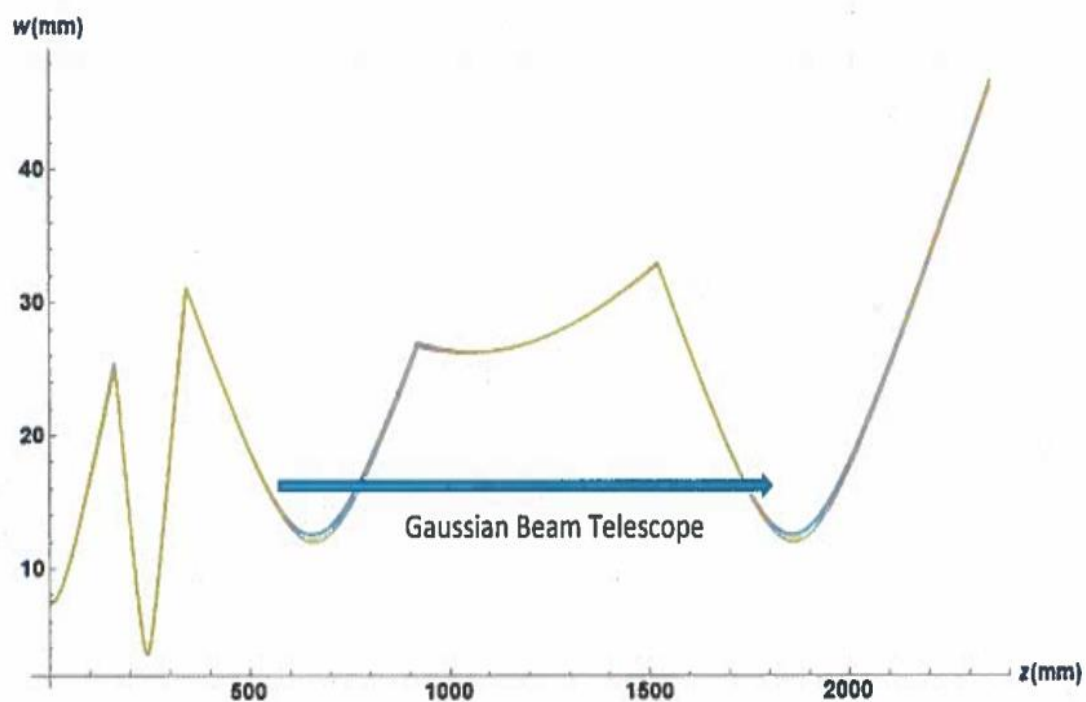
Figure 3.9: Plot of varying beam radius as a function of z, the propagation distance. The arrow illustrates how the Gaussian beam telescope maps the radius at one position to a position 1200 mm (300+600+300 mm) further on along the propagation path.
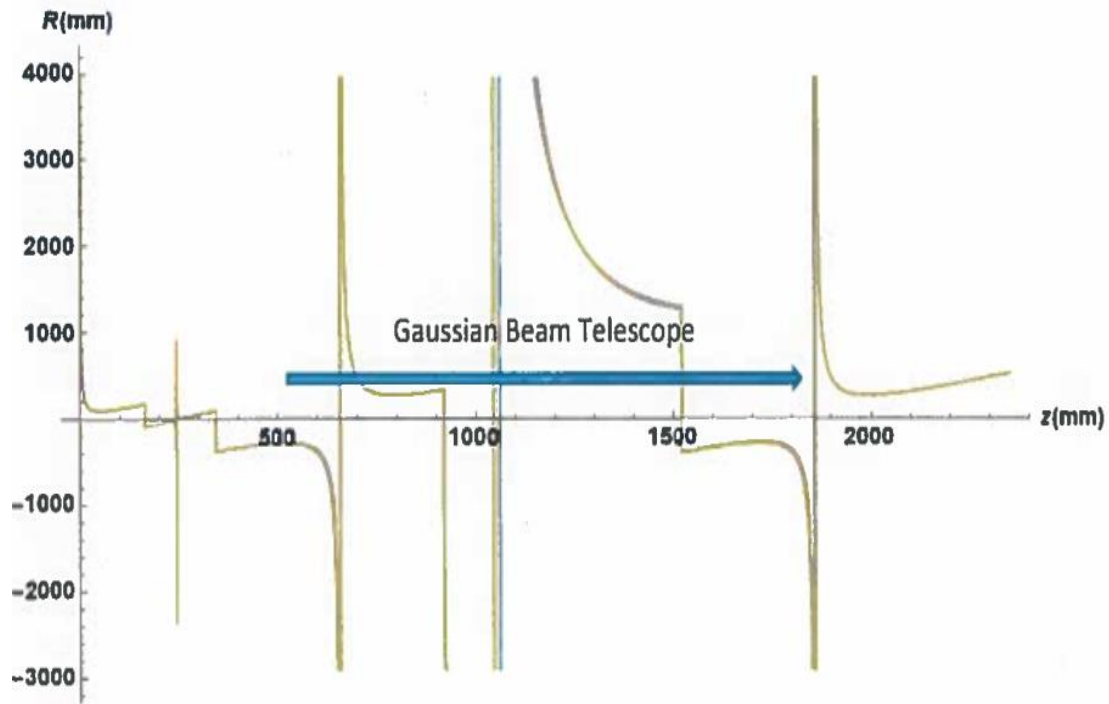
Figure 3.10: Plot of varying phase radius of curvature as a function of z, the propagation distance. The arrow illustrates how the Gaussian beam telescope maps the phase radius at one position to a position 1200 mm (300+600+300 mm) further on along the propagation path

As a further illustration, the component positions and sizes are illustrated in figure 3.11. This can be compared with figure 3.12 which is the equivalent plot for the 3 mm channel without the Gaussian Beam Telescope re-design. The beam at the mirror FM_01 is identical in both cases. The new mirrors required are similar in size to those already used.
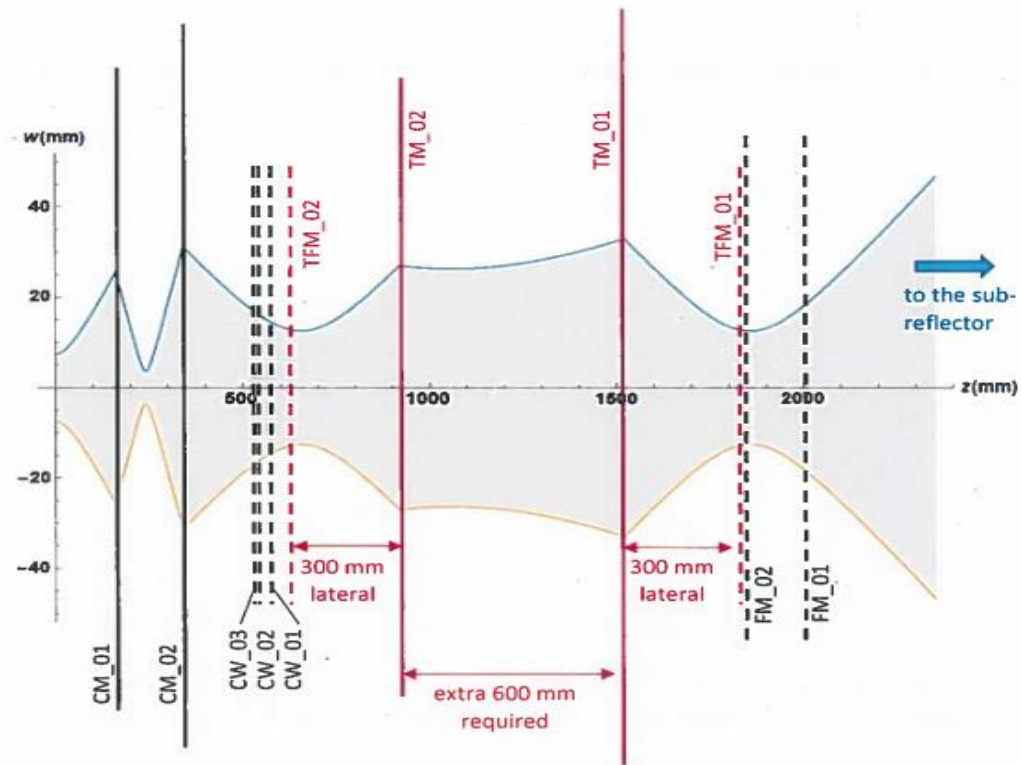
Figure 3.11: The beam radius w as a function of propagation distance through the 3 mm channel. The location and size of the optical components are shown. The components plotted in red are the proposed new elements. Components shown with a solid line are powered. $-w(z)$ is also shown for visualisation.
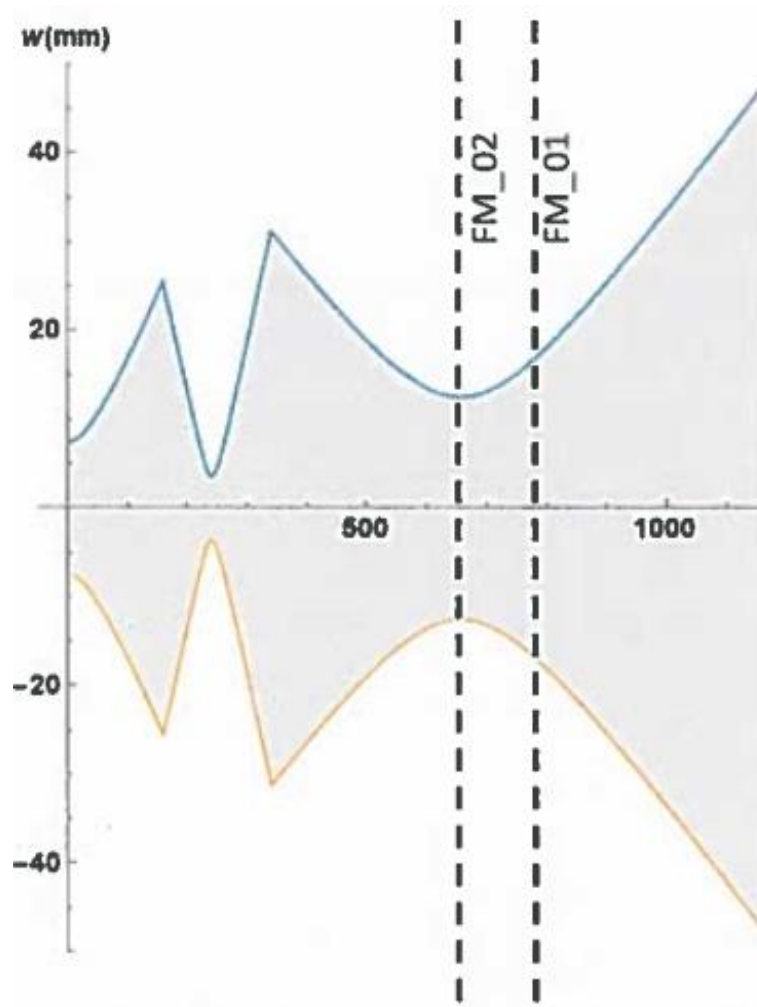
Figure 3.12: The beam radius w as a function of propagation distance through the existing 3 mm channel (i.e without the proposed Gaussian Beam Telescope). The location and size of the final two optical components are shown. $-w(z)$ is also shown for visualisation.

Optical Stop	Edge Taper for each Frequency		
	84 GHz	86 GHz	88 GHz
Cold Mirror 2	-65.37 dB	-66.30 dB	-67.2 dB
Cold Mirror 1	-56.96 dB	-57.24 dB	-57.49 dB
Cryostat Window 3	-73.49 dB	-75.23 dB	-76.93 dB
Cryostat Window 2	-73.45 dB	-75.33 dB	-77.17 dB
Cryostat Window 1	-89.99 dB	-93.03 dB	-96.06 dB
Test Flat Mirror 2	-54.29 dB	-56.62 dB	-58.92 dB
Test Mirror 2	-54.29 dB	-55.22 dB	-55.72 dB
Test Mirror 1	-54.29 dB	-55.22 dB	-55.72 dB
Test Flat Mirror 1	-54.29 dB	-56.62 dB	-58.92 dB
Flat Mirror 2	-167.333 dB	-175.33 dB	-183.51 dB
Flat Mirror 1	-79.1 dB	-81.18 dB	-83.23 dB
Sub reflector	-12.02 dB	12.01 dB	-12 dB

Table 3.13: Edge taper of the beam at each stop

From table 3.13, the addition of the extra 600 mm of propagation using the Gaussian beam telescope allows for the edge taper criterion at the sub reflector to be achieved.

3.2.4   Beam Truncation Through the System

One factor that greatly affects the quality and efficiency of millimetre and sub-millimetre systems is the effect of truncation and diffraction. The truncation level depends on the size of an optical component compared to the size of the beam. As a beam passes through an aperture some power within the beam is lost, how much is dependent on the size of the aperture relative to the size of the beam.

As well as the power loss in the beam calculated in the previous section, truncation also affects the shape of a beam. As the beam travels through an aperture, its edges are truncated, diffraction occurs and an increase in the side lobes of the beam can appear as the beam propagates further. If the truncation of a beam is severe enough, it can lead to errors in the coupling of the beam to a receiver horn. It is a

common rule of thumb that the minimum radius for an aperture to limit the amount of truncation to acceptable levels is $2w$, where w is the beam radius at the stop. Values below this can have significant effects on the beam shape and power [Ediss, 1990]. In the 3 mm and 4 mm system, the mirrors within the cryostat have a radius of 2.5 the size of the beam radius. The same method was applied for choosing the size for the four new mirrors proposed for the solution to the extension of the 3 mm channel. All other stops sizes can be seen in table 3.3 and the relevant beam width can be seen in table 3.11.

The effect of truncation on the beam can be found by comparing the electric field incident on the aperture to the output electric field just after the aperture. Unlike the previous analysis in section 3.2.3, higher order modes are used to model the shape of the beam with greater accuracy than can be achieved with a single Gaussian. The incident and output electric fields can be described using Laguerre-Gaussian modes as:

$$
\begin{aligned}
E_i(r) &= \sum_n A_n \psi_n(r) \\
E_o(r) &= \sum_m B_m \psi_m(r)
\end{aligned}
\tag{3.4}
$$

Here, A_n and B_m are the input and output beam mode coefficients and r is the radial distance from the axis of propagation of the beam, we assume circular symmetry here. These beam mode coefficients determine how much power is contained within a mode's transverse amplitude distribution and the total power in the beam can be found by summing up all the mode coefficients, e.g.

$$
Power = \sum_n A_n^* A_n.
\tag{3.5}
$$

It is possible to write the output field of the beam through a stop in terms of the incident field as follows, see e.g [Trappe, 2002]. At positions where $r < a$, the

incident beam is free to travel through the aperture and:

$$E_o(r) = E_i(r). \tag{3.6}$$

At positions where $r \geq a$ the electric field is essentially blocked from passing through and the aperture truncates the remaining power at these positions. Thus:

$$E_o(r) = 0. \tag{3.7}$$

When truncation occurs, the mode coefficients of the output field (B_m) are different to those of the input field (A_n). The output coefficients can be described using the overlap integral:

$$B_m = \int_0^\infty \psi_m^*(r) E_o(r) 2\pi r dr \tag{3.8}$$

Since the output field, where $r < a$, is equal to the incident field, and is zero outside of this, B_m can be described as;

$$B_m = \int_0^a \psi_m^*(r) E_i(r) 2\pi r dr. \tag{3.9}$$

Substituting for E_i from (3.4) this becomes:

$$B_m = \sum_n A_n \int_0^a \psi_m^*(r) \psi_n(r) 2\pi r dr \tag{3.10}$$

The integrand can be described as an element of a scattering matrix S_{mn} giving:

$$B_m = \sum_n A_n S_{mn} \tag{3.11}$$

where, if we are using Laguerre-Gaussian modes to describe the beam

$$S_{mn} = \int_0^a \psi_m^*(r) \psi_m(r) 2\pi dr = \int_0^a \frac{2}{\pi w^2} L_m \left[\frac{2r^2}{w^2} \right] L_n \left[\frac{2r^2}{w^2} \right] e^{\frac{2r^2}{w^2}} 2\pi r dr \tag{3.12}$$

Using equations 3.11 and 3.12, the beam modes for the output field from a stop or component aperture can be found.

3.3   Gaussian Beam Mode Analysis of the Beam Profile

3.3.1   Beam profile in the Existing 3-mm System

The effect of truncation was investigated by modelling beams (across the 84-88 GHz frequency band) as they propagated from the detector horn and out through the optical system of figure 3.5. The beam from the corrugated horn was modelled as a linearly polarised truncated Bessel function:

$$E_{aperture}(r) = J_0(\frac{2.450r}{a})e^{\frac{-j\pi r^2}{\lambda R}} \qquad (3.13)$$

where a and R are the aperture radius and phase radius of curvature ($=$ slant length of the horn), respectively (see e.g. [Goldsmith, 1998]). Here $a = 15$ mm and $R = 100$ mm. The best-fit Gaussian to this aperture has a waist radius and location as given by equations 3.1 and 3.2. The coupling of a single Gaussian to this distribution is high with

$$c = \frac{\int_\infty E_{aperture}\psi_G^* dA}{\sqrt{\int_\infty E_{aperture}E_{aperture}^* dA}\sqrt{\int_\infty \psi_G\psi_G^* dA}} \approx 0.99. \qquad (3.14)$$

The mode coefficients for the higher-order modes, A_n were calculated using equation (2.50) applied at the horn aperture. It was considered sufficient to use 20 modes for these calculations; using more did not have any significant effect on the results. The beam at each frequency was then propagated to the first component, CM_02, using the expressions for $w(z)$, $R(z)$ and $\phi_0(z)$ given in equations 2.52, 2.53 and 2.54. Truncation by the CM_02 mirror aperture was modelled by first determining

the mode scattering matrix S_{mn} using equation 3.12, then the new mode coefficients B_m from equation 3.11.

The field truncated by CM_02 was found from equation 1.4 where the modes ψ_m (Laguerre-Gaussian modes of equation 2.43) were calculated using the new values of $w(z)$, $R(z)$ and $\phi_0(z)$. w, R and ϕ_0 after reflection from the mirror were calculated using the ABCD analysis described in Chapter 2. The ABCD matrix used for the mirror was $\begin{bmatrix} 1 & 0 \\ \frac{-1}{f} & 1 \end{bmatrix}$ with f the equivalent focal length of the elliptical mirror CM_02 (equation 2.79). The coefficients B_m were then labelled A_n and the process repeated from CM_02 to CM_01 using the new $w(z)$, $R(z)$ and $\phi 0(z)$ as the values at the start of the propagation step.

Propagation beyond CM_01 was carried out similarly except the ABCD matrix step was not required for the cryostat windows or at the flat mirrors. Table 3.14 lists the propagation and truncation steps used in the analysis. Table 3.17 shows this truncation had little effect and edge taper levels were low.

	Component	Propagation distance (mm)	Truncation (radius, mm)	Focal length (mm)
1	Waist to aperture	40.18		
2	aperture		$a(= 15\ mm)$	
3	aperture $\rightarrow$ CM02	120		
4	Mirror CM02		70	56.07
5	CM02 $\rightarrow$ CM01	180		
6	Mirror CM01		80	79.355
7	CM01 $\rightarrow$ CW03	200.1		
8	CW03		47.5	
9	CW03 $\rightarrow$ CW02	9		
10	CW02		46	
11	CW02 $\rightarrow$ CW01	34.3		
12	CW01		45.5	
13	CW01 $\rightarrow$ FM02	71.6		
14	FM02		55	
15	FM02 $\rightarrow$ FM01	146.4		
16	FM01		55	
17	FM01 $\rightarrow$ subreflector	8290.5		

Table 3.14: Propagation, focussing and truncation steps carried out for the Gaussian beam mode analysis of the existing 3-mm channel. Row 13 is the step that is replaced in the new proposed design

Figure 3.13 shows cuts through the predicted beam at optical components in the system. Each beam is compared with the beam that would have been obtained if there were no truncation at the mirrors and a simple single Gaussian beam mode analysis (Tables 3.7 and 3.8). The field at the horn aperture is shown on both a linear and logarithmic(dB) scale.

The analysis shows that although the power coupling between a Gaussian and the Bessel function aperture field is high ($= c^2 \approx 98\%$) it does not always represent the beam shape well (and the difference may appear slightly greater when both are individually normalised as was done here). Truncation and diffraction at the horn and optical component apertures causes the development of sidelobes and other features at low levels at intermediate planes and even with this low level of

truncation there is some difference in beam shape on the subreflector. The edge taper is slightly higher than the $-12\,\text{dB}$ given by the single-mode analysis (Figure 3.13).

The power lost by truncation at the mirrors can be determined from the mode coefficients. If the input beam is normalised so that $\sum_n A_n A_n^* = 1$ then the power remaining in the beam at each component can be found from $\sum_n B_n B_n^*$. Calculated values are given in Table 3.15 and show that with this level of truncation, very little power ($< 1\%$) is lost.

Component	Power (84 GHz)
aperture	1
CM02	0.9987
CM01	0.9981
CW03	0.9977
CW02	0.9976
CW01	0.9976
FM02	0.9976
FM01	0.9969

Table 3.15: Power in the beam as it propagates through the existing 3-mm channel.
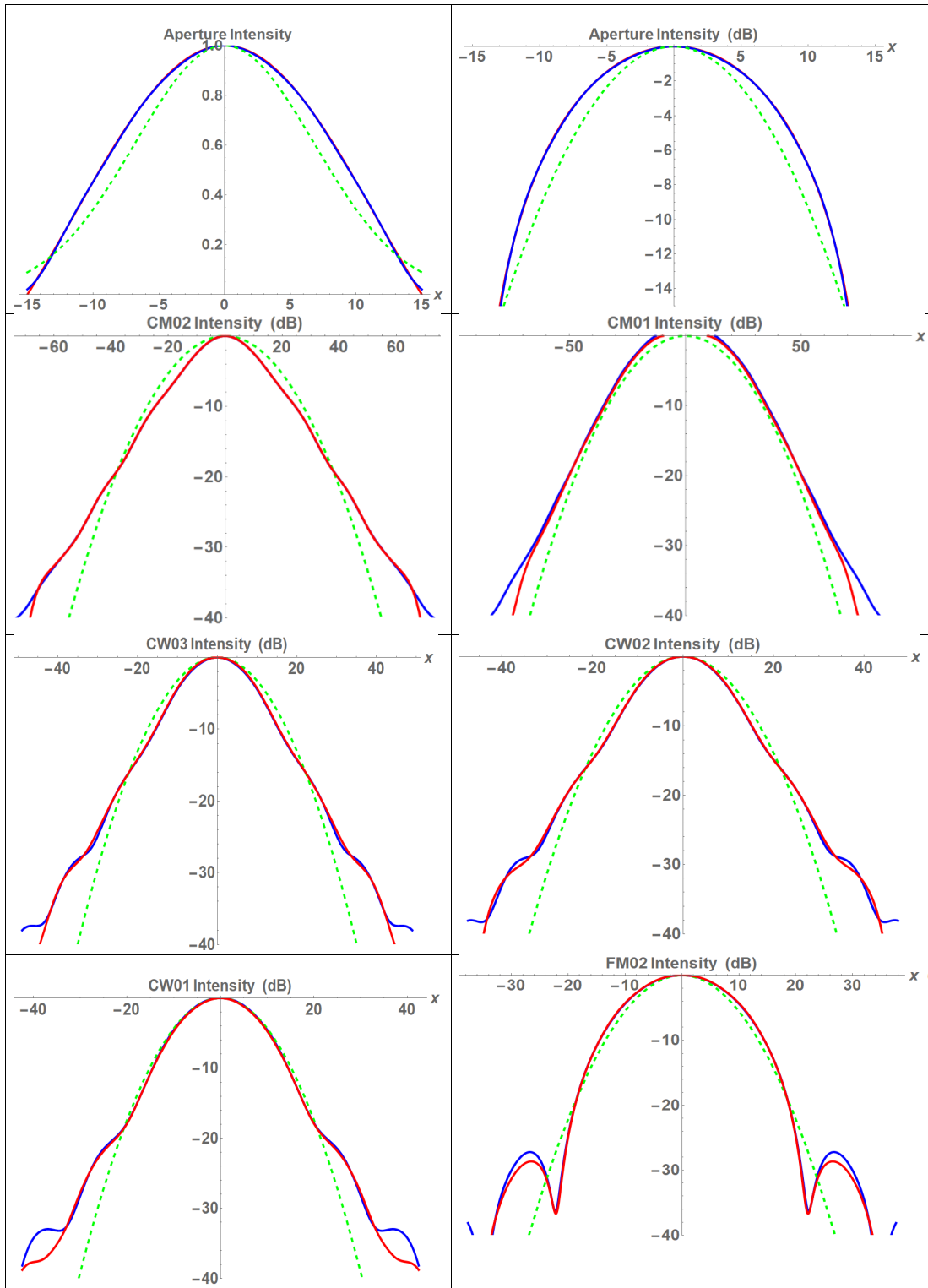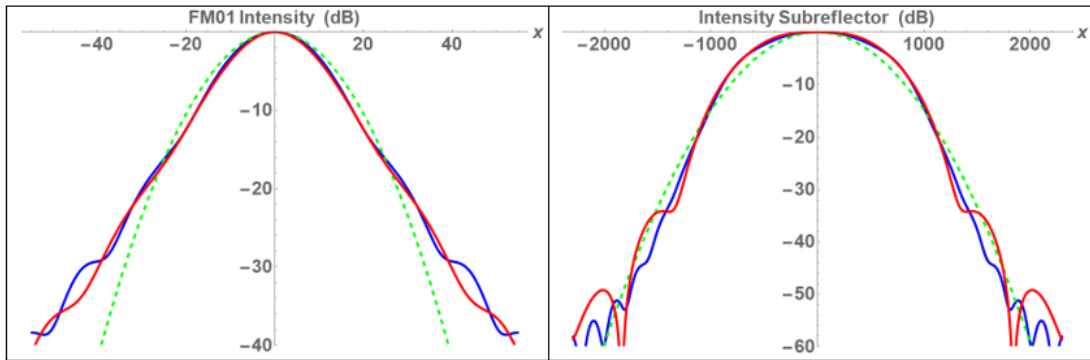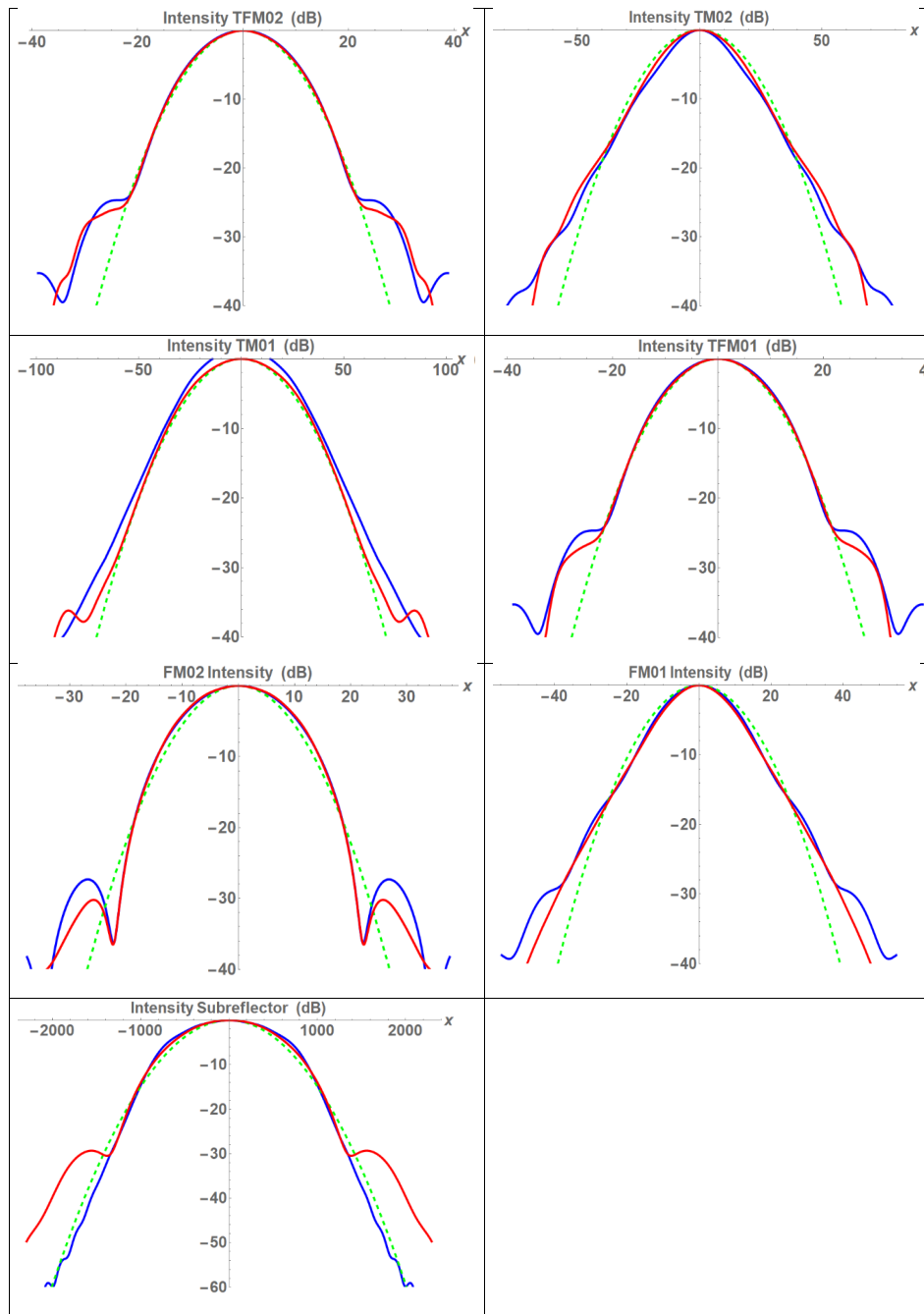
Figure 3.13: 84-GHz beam profile at the various optical components in the current 3-mm channel. The dashed green line shows the prediction when a single best-fit Gaussian beam is used (equivalent to the analyses carried out for Tables 3.7 and 3.8). The blue line shows the beam if there were no truncation at any of the components and the red line shows the predicted effect on the beam when both diffraction and truncation are considered.
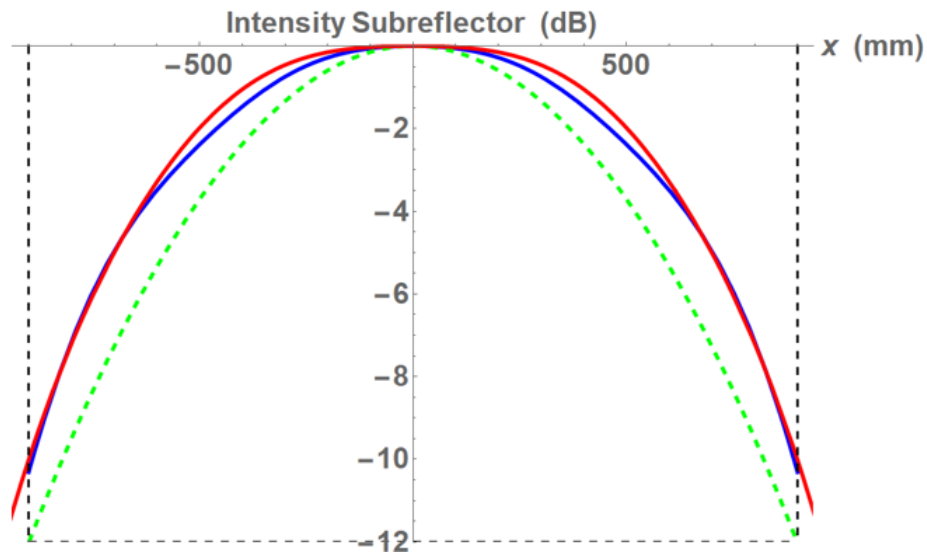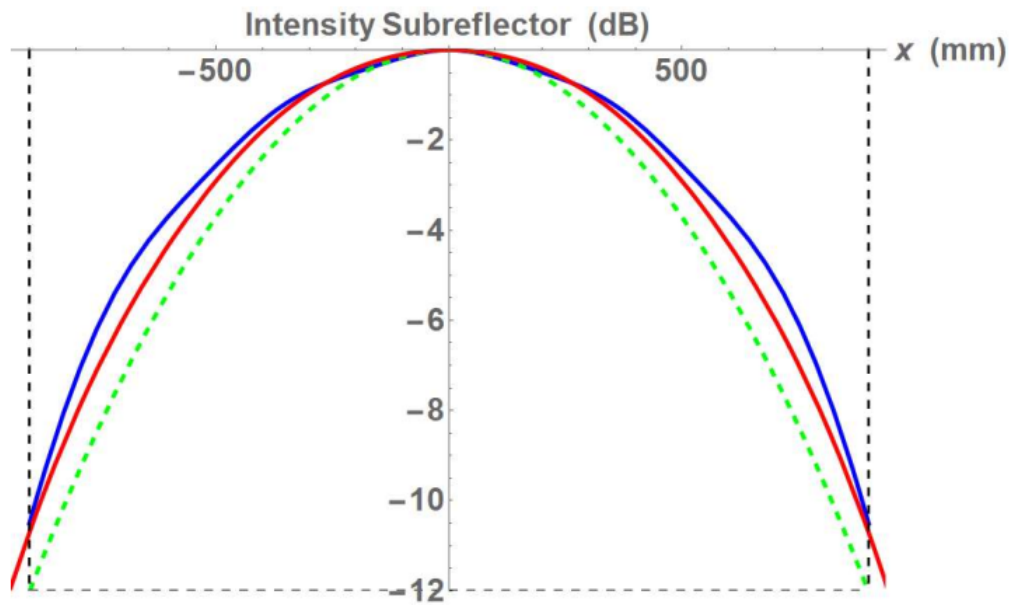

Figure 3.14: The field at the 900-mm radius sub-reflector as predicted by a Gaussian beam mode analysis (section of the final plot in Figure 3.13). The three traces are as given in Figure 3.13.

3.3.2 Beam Profile in the Proposed 3-mm System

The proposed system was modelled as just described for the existing system but with the extra steps for the Gaussian beam telescope addition included (Table 3.16).

	Component	Propagation distance (mm)	Truncation (radius, mm)	Focal length (mm)
1	Waist to aperture	40.18		
2	aperture		$a(= 15 \text{ mm})$	
3	aperture → CM02	120		
4	Mirror CM02		70	56.07
5	CM02 → CM01	180		
6	Mirror CM01		80	79.355
7	CM01 → CW03	200.1		
8	CW03		47.5	
9	CW03 → CW02	9		
10	CW02		46	
11	CW02 → CW01	34.3		
12	CW01		45.5	
13	CW01 → TFM02	35.8		
14	TFM02		32.5	
15	TFM02 → TM02	300		
16	TM02		67.5	300
17	TM02 → TM01	300		
18	TM01		82.5	300
19	TM01 → TFM01	300		
20	TFM01		32.5	
21	TFM01 → FM02	35.8		
22	FM02		55	
23	FM02 → FM01	146.4		
24	FM01		55	
25	FM01 → subreflector	8290.5		

Table 3.16: Propagation, focussing and truncation steps carried out for the GBM analysis of the proposed 3-mm channel. Rows 13-21 are the additional steps in the new proposed design.

Figure 3.15 shows cuts through the beam at optical components in the system (the plots corresponding to the aperture through CW_01 are the same as the existing

channel and so are not shown here). Each beam is again compared with the beam that would have been obtained if there were no truncation at the mirrors and a simple single Gaussian beam mode analysis (Tables 3.11 and 3.12).

The sidelobes that appear at the subreflector plane are below -30 dB and will be truncated by the subreflector itself. The plots show that the addition of the Gaussian beam telescope does not degrade the quality of the final beam.

Figure 3.15: 84-GHz beam profile at the various optical components in the proposed 3-mm channel. The dashed green line shows the prediction when a single best-fit Gaussian beam is used (equivalent to the analyses carried out for Tables 3.11 and 3.12). The blue line shows the beam if there were no truncation at any of the components and the red line shows the predicted effect on the beam when both diffraction and truncation are considered.

Figure 3.16: The field at the 900-mm radius sub-reflector as predicted by a Gaussian beam mode analysis (zoom-in of the final plot in Figure 3.15) for the proposed new system. The three traces are as given in Figure 3.15.

The power lost by truncation at the mirrors was again determined from the mode coefficients and calculated values are given in Table 3.17. As with the existing system, with these levels of truncation, very little power ($< 1\%$) is lost.

Component	Power (84 GHz)
aperture	1
CM02	0.9987
CM01	0.9981
CW03	0.9977
CW02	0.9976
CW01	0.9976
TFM02	0.9972
TM02	0.9969
TM01	0.9962
TFM01	0.9952
FM02	0.9951
FM01	0.9949

Table 3.17: Power in the beam as it propagates through the proposed 3-mm channel.

3.4 Physical Optics Analysis of the Beam Profile with GRASP

3.4.1 Beam Profile in the Existing 3-mm System

The previous Gaussian-beam mode analysis gives a good representation of the beam as it propagates through the 3-mm optical system, but while it does consider diffraction and truncation for a paraxial beam, several simplifications were made. In particular, the off-axis mirrors were represented by perfect thin on-axis lenses of the same equivalent focal length and so the asymmetries that we would expect for such a system were not modelled. The field was also considered as scalar with no cross-polarisation, something that we would again expect to be introduced after reflection from the mirrors. As described in Chapter 2, a full vector physical optics analysis can be carried out in GRASP for a more accurate prediction of the beam shape in the system.

The existing 3-mm channel was set up in GRASP (Figure 3.17) using the "Scatte-

rer → Reflector (Ellipsoid Surface)", "Scatterer→Reflector (Plane Surface)", "Aperture in Screen" and "Feed→Hybrid Mode Conical Horn" objects. (Details of how the mirrors are set up in GRASP are given later for the new mirrors proposed in this thesis.) The flat mirrors FM_01 and FM_02 were set up as apertures so the model could be compared with that of Walker [Walker, 2016]. The system as set up in GRASP is shown in Figure 3.17.
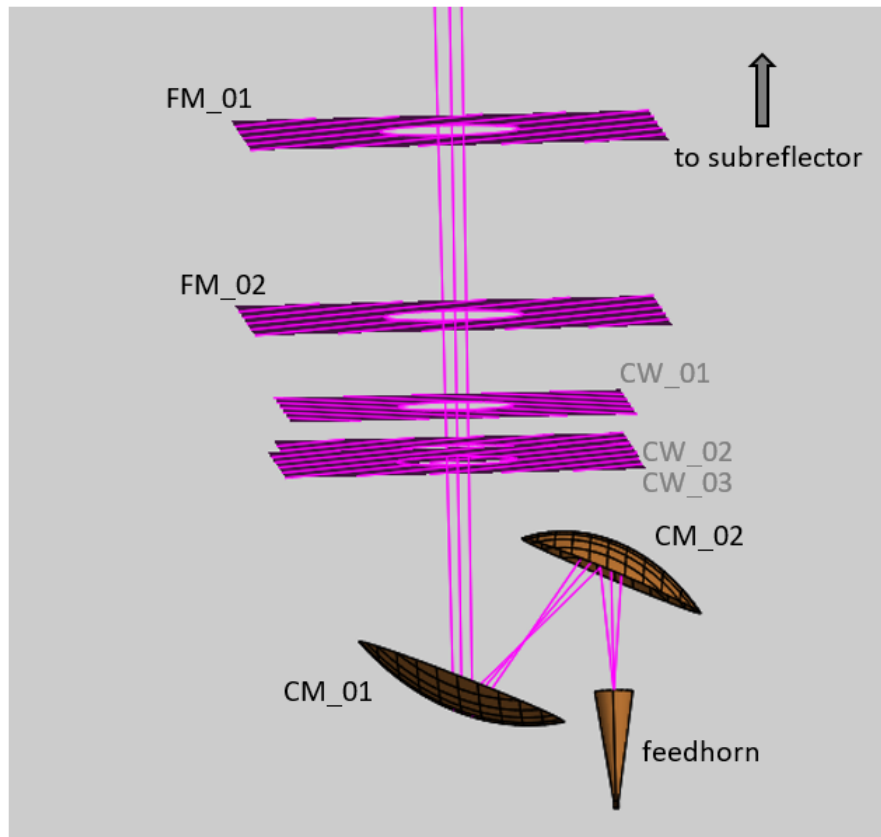
Figure 3.17: Model of the OSO 3-mm system as implemented in GRASP. The view has been tilted to see the aperures more clearly.

GRASP was used to calculate the currents induced on the mirrors and aperture screens and finally the field on a plane at the location of the subreflector was calculated. (An accuracy of -80 dB and 401×401 PO points were specified in GRASP, PO + PTD was used.) Orthogonal cuts through the beam at the plane of the subre-

flector are shown in Figure 3.18. The asymmetry introduced by the off-axis mirrors in one plane is clear. It should be noted that the subreflector will truncate this field at a radius of 900 mm.
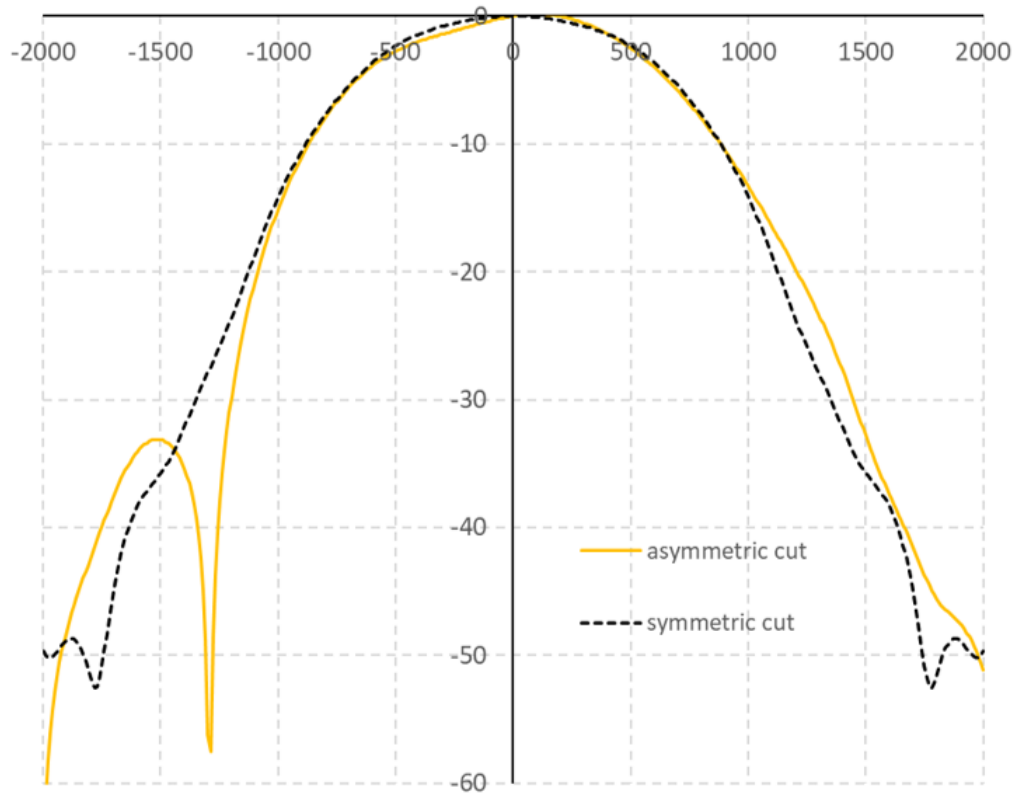
Figure 3.18: Orthogonal cuts through the OSO 3-mm channel co-polar beam on a plane at the subreflector location. The subreflector will truncate the beam at $r = 900\,\mathrm{mm}$.

Plots of the co-and cross-polar beam are shown in figure 3.19. The asymmetry gives rise to one sidelobe which will be truncated at the mirror and also means that the maximum of the beam is not quite at the centre.

The symmetric cut through the pattern was compared with the earlier Gaussian beam mode analysis to assess the effect of the more accurate analysis. The comparison is shown in Figure 3.20. The Gaussian beam mode analysis is clearly a very good approximation for this type of system if the asymmetries due to the off-axis

mirrors are not required.
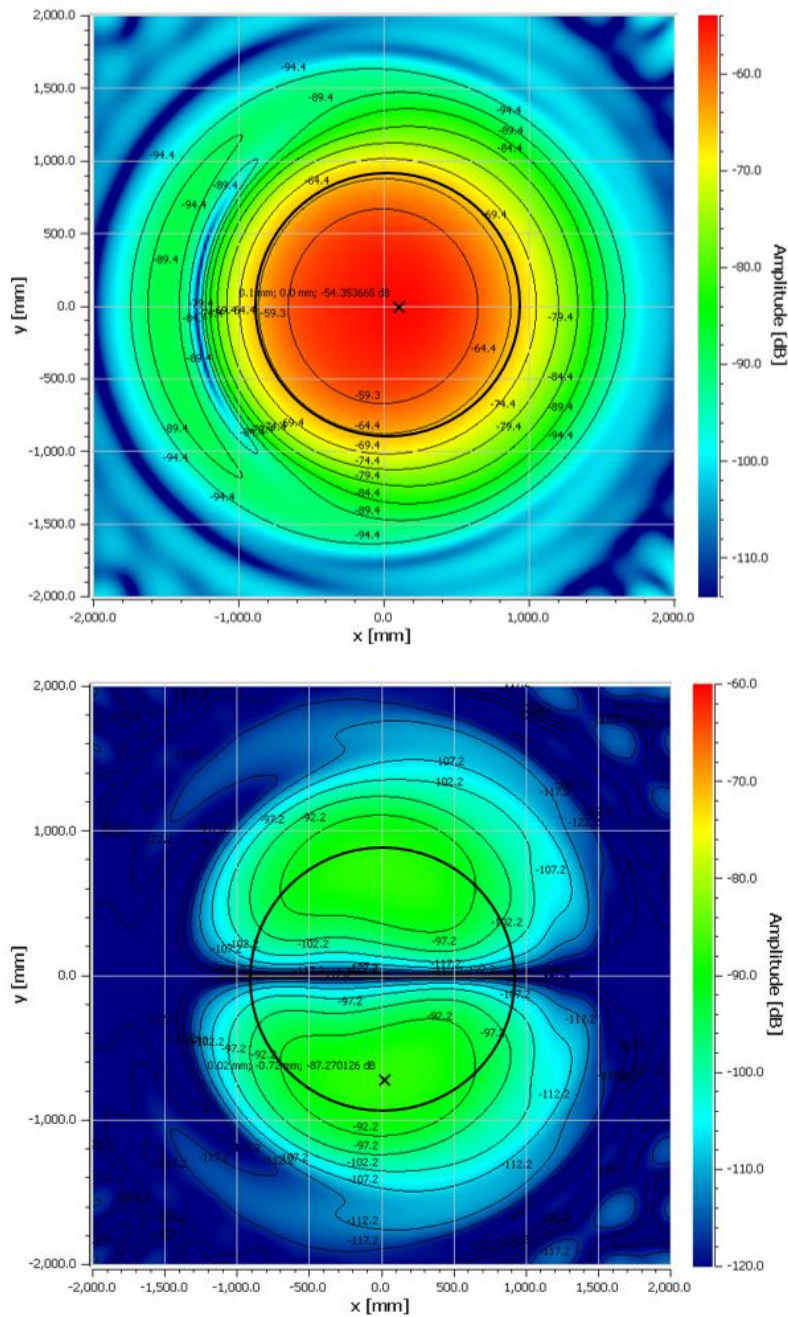
Figure 3.19: Co-(top) and cross-(bottom) polar plots of the beam pattern at the subreflector (whose size is indicated by the thick black circle). The peak of each plot is marked with an 'x'. The peak cross-polar level is 32.9 dB below that of the co-polar.
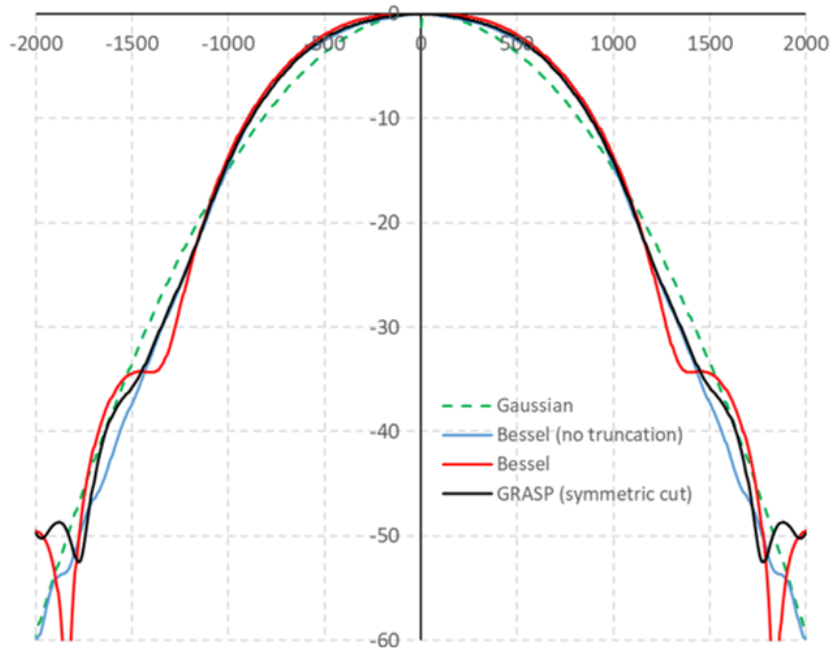
Figure 3.20: Beam profile at the subreflector location. Results for the GRASP PO calculation are compared with those from the Gaussian beam mode analyses using a single Gaussian approximation, no mirror truncation (20 Gaussian modes with the horn aperture field described by a Bessel function) and mirror truncation.

3.4.2   Beam Profile in the Proposed 3-mm System

Next, the proposed Gaussian beam telescope extension was added to the existing system. The off-axis mirrors were designed as follows. Each mirror was required to have a focal length of 300 mm and an angle-of-throw of 90 deg. The ABCD matrix analysis described earlier gave the beam radius (w, Table 3.11) and phase radius of curvature (R, Table 3.12) before and after each mirror. If the absolute value of the phase radii of curvature before and after the mirror are labelled R_1 and R_2, respectively, and ϕ is half the angle-of-throw, then the semi-major (a) and semi-minor (b) axes and the distance from the centre to the focus of the elliptical surface (c) can be found from equations 2.80, 2.81 and 2.82. The vertex distance, $2a$, and interfocal distance $2c$ are the values required by GRASP to define the

elliptical surface. The orientation of the ellipse was specified according to GRASP's convention (Figure 3.21). The local coordinate axes were rotated as required and centred at one of the ellipse focii. The surface could then be rotated as required, see figures 3.22 and 3.23. Each mirror rim was centred on the input beam ($x = y = 0$ in the local coordinate system) and given a radius of $2.5w$. The system as set up in GRASP is shown in Figure 3.24 which also illustrates the extra 600 mm distance between the cryostat (CW_01) and the subreflector that was required in this new system. The results of the GRASP analysis are shown in Figures 3.25 to 3.27.
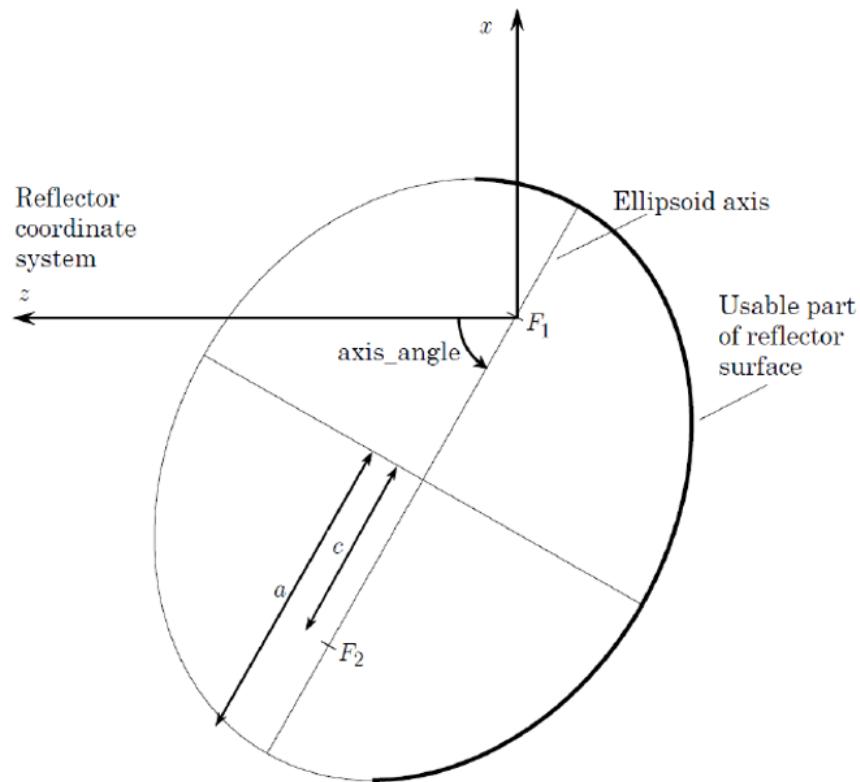
Figure 3.21: GRASP definition of elliptical surface orientation (taken from the GRASP manual [TICRA, 2013]). The axis angle is the anticlockwise rotation from the local +z axis. The usable part of the mirror is defined by the rim radius and offset in the local xy plane, with its concave part facing the +z direction.
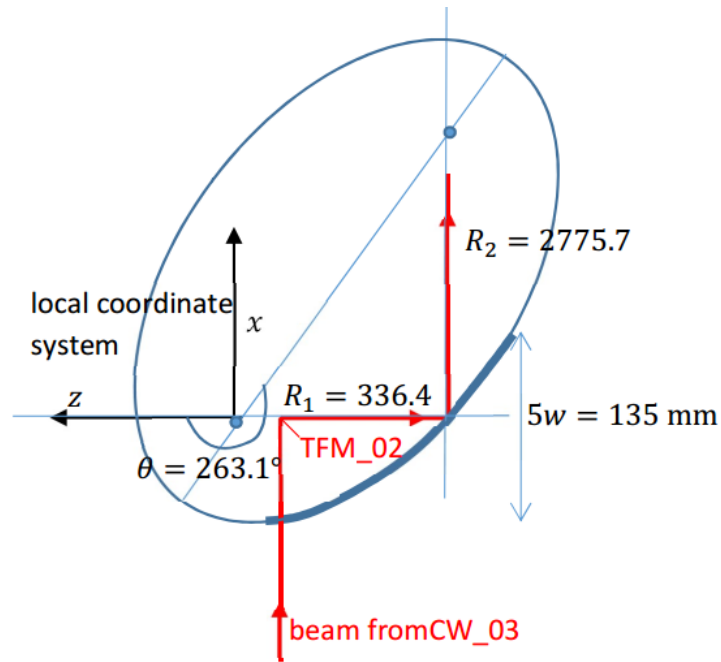
Figure 3.22: Set up of new mirror TM_02 in GRASP.
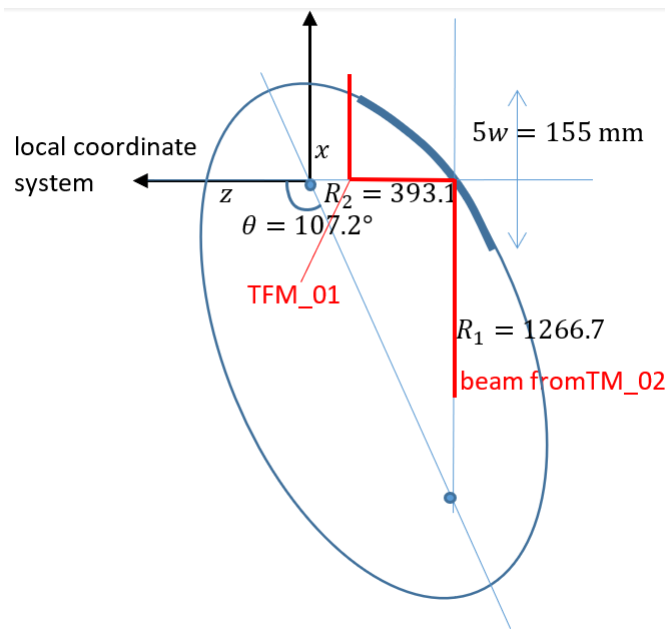
Figure 3.23: Set up of new mirror TM_01 in GRASP.
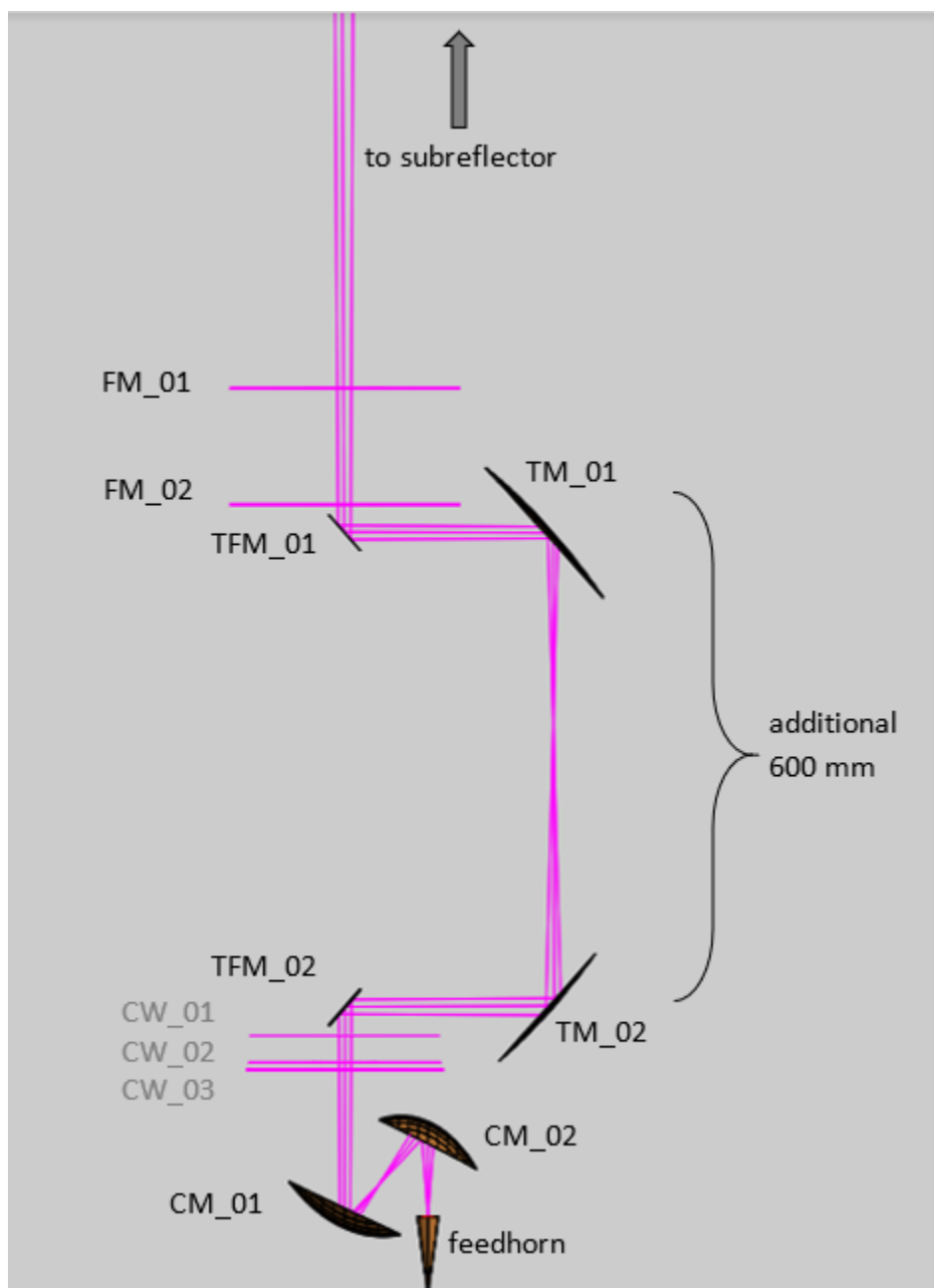
Figure 3.24: Model of the proposed new OSO 3-mm system as implemented in GRASP. The details of the GRASP .tor file are given in Appendix A.
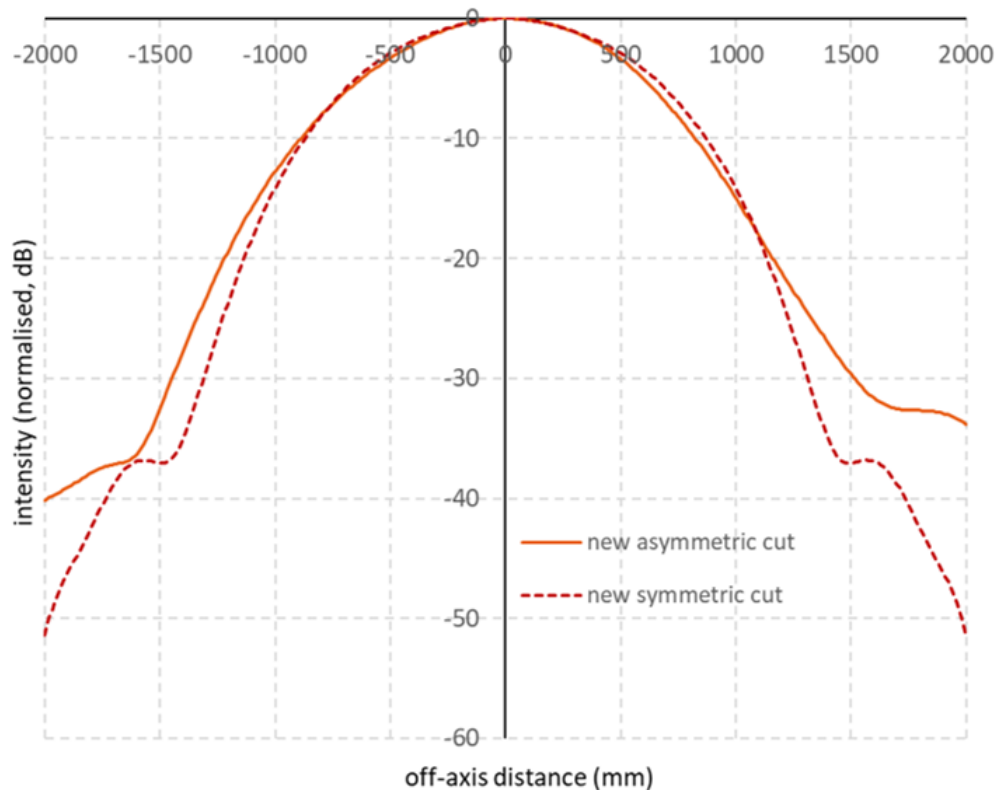
Figure 3.25: Orthogonal cuts through the proposed OSO 3-mm channel co-polar beam on a plane at the subreflector location. The subreflector will truncate the beam ar $r = 900$ mm.
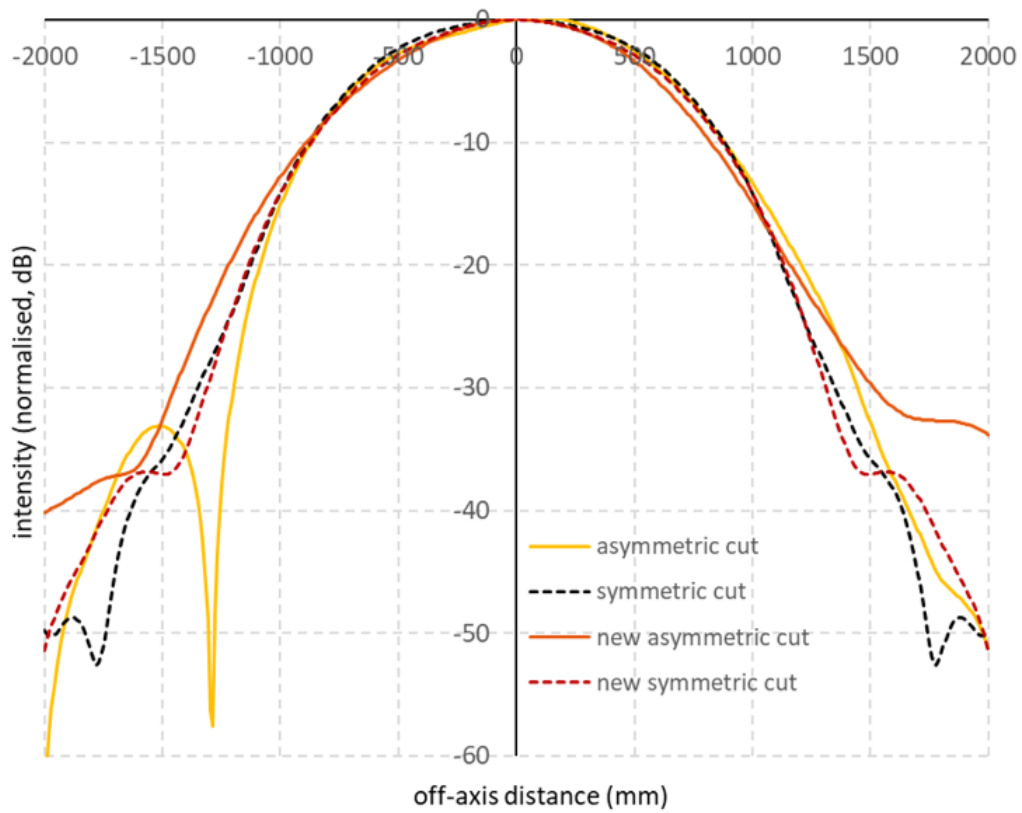
Figure 3.26: Orthogonal cuts through the OSO 3-mm channel co-polar beam on a plane at the subreflector location. The subreflector will truncate the beam at $r = 900$ mm. The beam for the new system which includes the Gaussian beam telescope addition is compared with the current system. The GRASP .tci command file used to generate these is given in Appendix B.
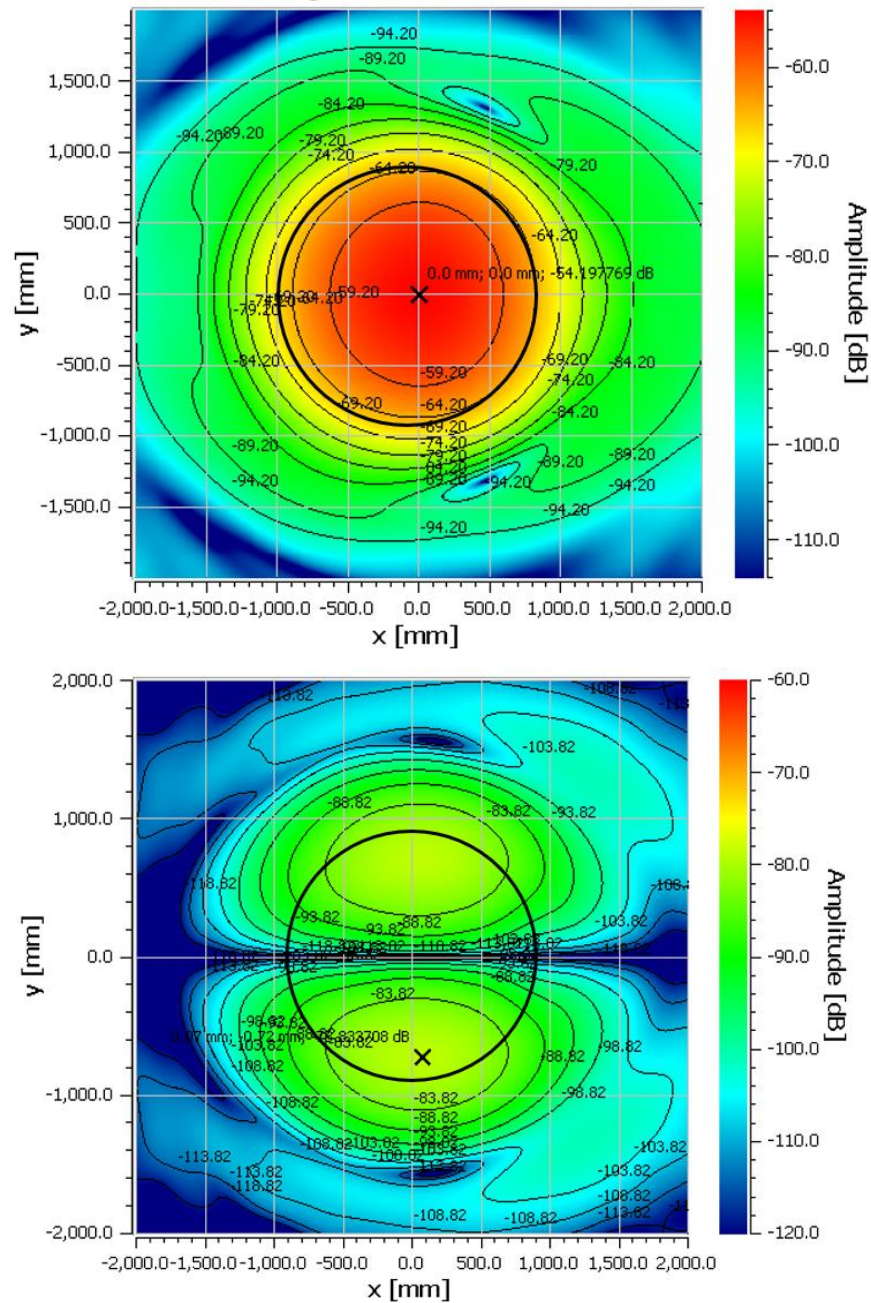
Figure 3.27: Co-(top) and cross-(bottom) polar plots of the beam pattern at the subreflector (whose size is indicated by the thick black circle) in the new proposed design. The peak of each plot is marked with an 'x'. The peak cross-polar level is 24.6 dB below that of the co-polar.

Although the beams appear slightly more asymmetric at low levels, the centre

of the main beam is on-axis in this new design. The cross-polar levels are increased but still low. In terms of beamshape over the subreflector, edge taper and cross-polarisation, we conclude that adding a Gaussian beam telescope is a possible method of moving the receiver cryostat back by 600 mm while maintaining the desired, frequency-independent beam at the subreflector. Finally we have compared the different analysis methods for this new system. The beam prediction of each is compared in Figures 3.28 and 3.29. There is excellent agreement between the Gaussian beam mode analysis (using 20 modes to describe the aperture field as a Bessel function and including truncation) down to -30dB. We would not expect there to be perfect agreement at the sidelobes because the simplified on-axis system of the Gaussian analysis will not be able to describe the off-axis mirror rims exactly. Even with this low level of truncation there is an effect on the main beam pattern, as can be seen when comparing the Gaussian analyses with and with out truncation.
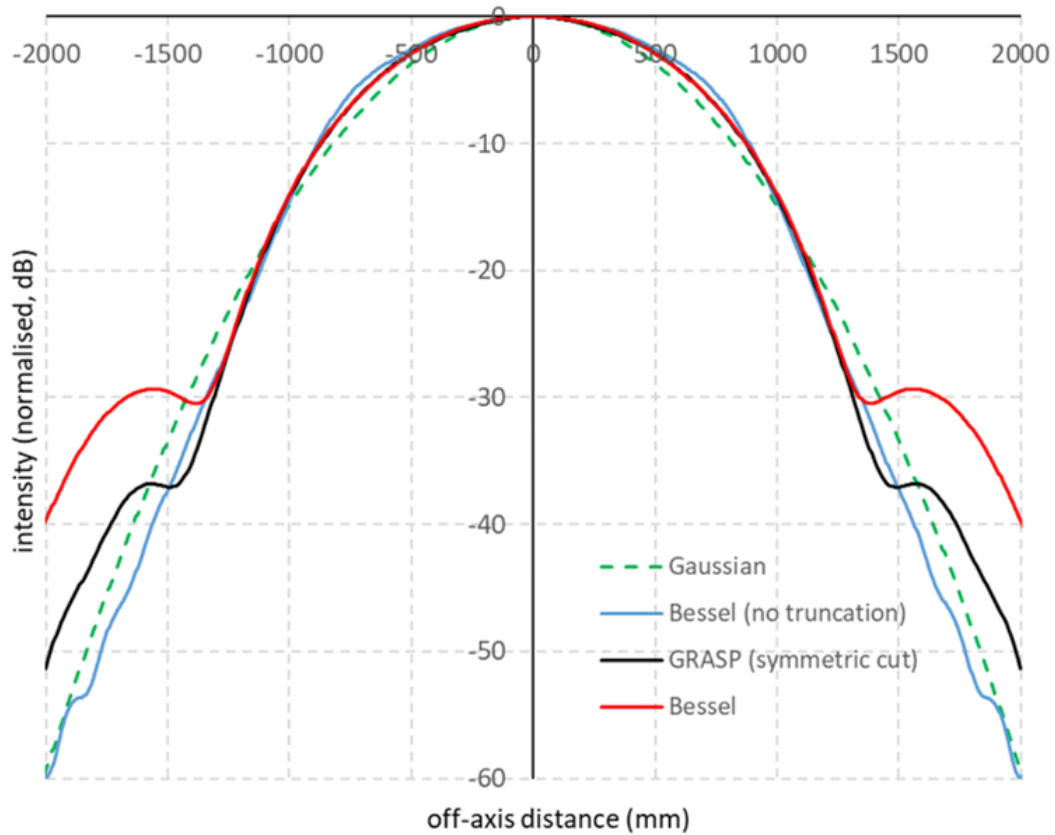
Figure 3.28: Beam profile at the proposed system subreflector location. Results for the GRASP PO calculation are compared with those from the Gaussian beam mode analyses using a single Gaussian approximation, no mirror truncation (20 Gaussian modes with the horn aperture field described by a Bessel function) and mirror truncation.
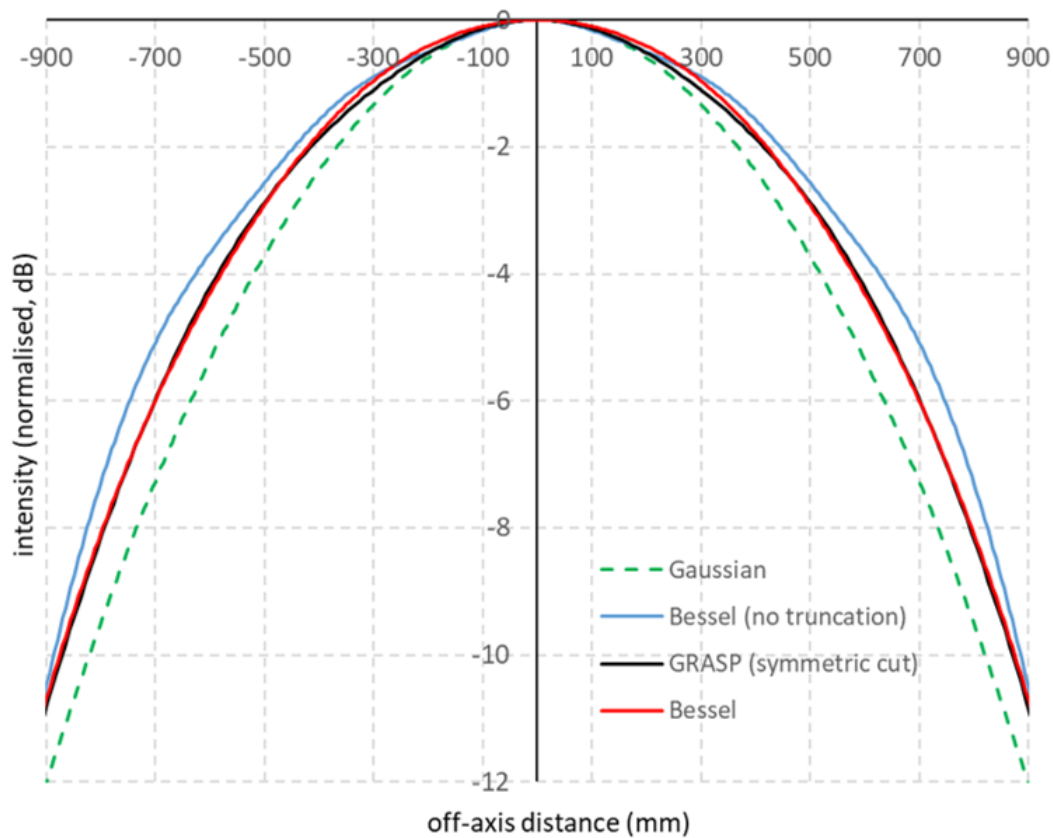
Figure 3.29: Same as figure 3.28 but zooming in on the part of the main beam that falls on the subreflector.

3.5   Conclusion

In this chapter the Onsala Space Observatory and its two main telescopes were described with my focus lying primarily on the 3 and 4 mm receiver channels of the 20 m telescope, and a proposed re-design of the 3 mm receiver channel.

The 4 mm channel was first analysed using Gaussian beam modes and ABCD matrices, following Walker [Walker, 2016]. This was used as a benchmark comparison with the earlier work. The analysis was then extended to the frequency of interest ($\sim$ 84 GHz) in the 3 mm channel before proposing the addition of Gaussian beam mode telescope optics to allow the receiver to be moved back 600 mm.

The proposed system was analysed using both Gaussian beam models and the more accurate physical optics described in Chapter 2. The extra optics was found to be a viable solution to the extra propagation distance required by OSO.

Carrying out the analysis using both Gaussian beam modes and physical optics has allowed me to judge the effectiveness of modelling techniques for such a system. The advantage of the Gaussian beam mode analysis over the more accurate physical optics is that it can be carried out in a relatively straight forward way using any mathematical software package. Vector physical optics software can be expensive to purchase. Both techniques are quick for a system like the OSO 3 mm channel modelled using a modern PC.

I found that Gaussian beam mode analysis using 20 modes gave an excellent prediction of beam shape and truncation levels and could certainly be used during the design phase of such a system. A final analysis using physical optics can then be carried out to determine beam asymmetry and cross polarization.

In the next chapter I extend this type of physical optics analysis to investigate the effect of non-ideal mirrors.

Chapter 4

Surface Tolerance Simulations with GRASP

4.1 Introduction

This chapter looks at modelling surface non-idealities using GRASP physical optics. In order to do this I make use of the "tabulated surface" function that allows surfaces to be defined in GRASP using a grid of points. Two particular non-idealities are investigated: random surface roughness and a raised ring feature. The effect of surface roughness is tested using the Onsala 4 mm model described in Chapter 3. The effect of a ring feature was analysed because it arose in the manufacture of a mirror for the QUBIC instrument with which the Maynooth group is involved. I also test the effects of the ring feature using the Onsala 4 mm model as a convenient sample system; there is no suggestion that either error was found or is a potential issue for the Onsala receiver.

In the previous chapter, two elliptical surfaces were entered into GRASP using 2nd order polynomials (CM_01 and CM_02) to define their shape. These surfaces were then shifted and rotated in GRASP until the required section of mirror was perpendicular to the local z-axis. However, GRASP is a flexible program and as

described at the end of Chapter 2, allows for a number of other methods for surfaces such as:

- **Ellipsoid** This class defines an ellipsoidal surface. The GRASP program is given the distance between vertices, the distance between foci and an angle of rotation for the surface (see figure 4.1). This input method was used for the new mirrors defined in Chapter 3.
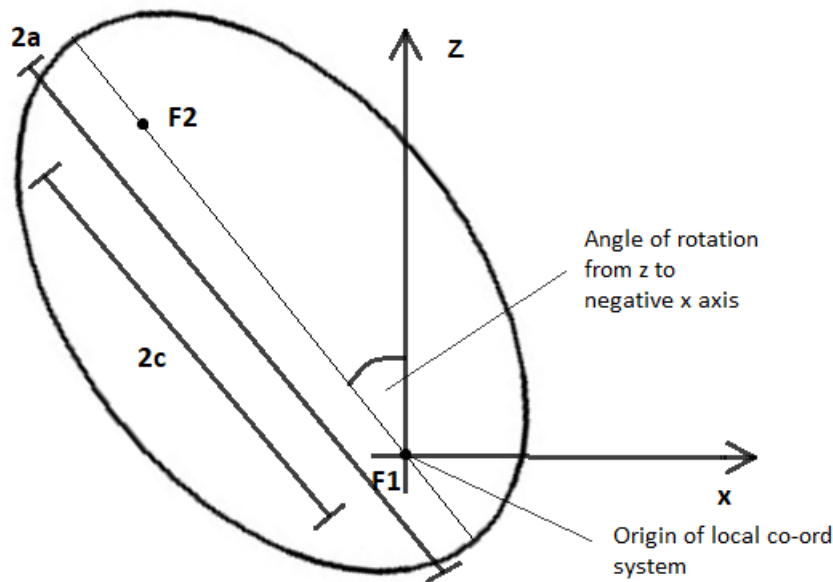

Figure 4.1: GRASP definition of an ellipsoidal surface (similar to figure 3.21).

- **Quadrics** Surfaces in this class are defined as second order polynomials where the surface z is defined in terms of x and y. This input method was used for the two existing elliptical mirrors in Chapter 3 (defined by Walker [Walker, 2016]).

- **Tabulated Surface** This class offers a number of differing methods to enter a surface in a tabular form.

This chapter outlines the processes followed in constructing a surface in GRASP using tabulated surfaces. This method of defining the mirrors proved to be useful

when adding random surface errors to an ideal descriptor in order to model real mirrors as manufactured.

4.2   Ellipses and Ellipsoids: Definition and Construction of Surfaces

In Chapter 3, the 4 mm channel of the Onsala 20 m telescope was discussed. In this chapter, the mirrors used in the 4 mm channel will be used to investigate the effect that random surface errors have on an optical system. These mirrors are common to the 3 and 4 mm systems.

4.2.1   Ellipses and Ellipsoids

The two powered mirrors used in the 4 mm system are elliptical mirrors which are commonly used due to their effectiveness at refocussing of a beam. Ellipses are a type of the shapes referred to as 'conics' since they can be described as a planar cut through a cone (see figure 4.2). Circles, ellipses, parabolas and hyperbolas are all examples of conic sections that differ by their *eccentricity*, ε. Each shape's eccentricity is as follows [Downs, 1993]:

- A **circle** has an eccentricity of 0

- An **ellipse** has an eccentricity where $0 < \varepsilon < 1$

- A **parabola** has an eccentricity of 1

- A **hyperbola** has an eccentricity of $\varepsilon > 1$

This eccentricity of a shape can be thought of as how far the foci diverge from the centre. For example, a circle has 0 eccentricity and its focus lies on its central point; any line through the centre of a circle will reflect back through it. An ellipse's

eccentricity results in a focus on either side of its centre and any line through one focus will be reflected and pass through the second. This attribute is one of the reasons that elliptical mirrors are a popular choice in optical systems.
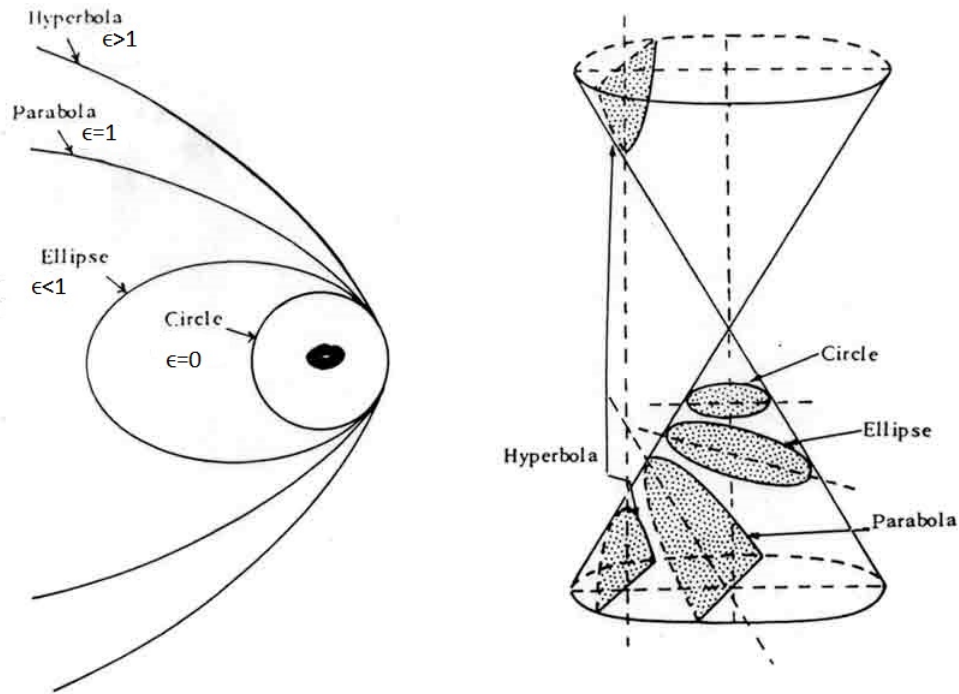

Figure 4.2: List of conic sections, their eccentricity and the planar cuts from the cone for each shape. [Bengal, 2004]

In the case of the Onsala system, the mirrors were first designed using their description as a conic section (parameters a and c were found from R_1 and f as described previously) and then implemented in GRASP using a second-order polynomial (quadric). Here a matrix formalism for the polynomial is used, as described next, so that the surface is translated and rotated as required before being input into GRASP as a table of points.

The general equation (canonical form) for an ellipse with the origin at its centre point, and using coordinate axes that are axes of the ellipse, is [Peiponen et al., 2013]:

$$\frac{x^2}{a^2} + \frac{y^2}{b^2} = 1 \tag{4.1}$$

where a and b are the major and minor half-axis respectively. When $a > b$ the ellipse formed is referred to as an oblate ellipse and where $b > a$ the ellipse is referred to as a prolate ellipse.

An ellipsoid of revolution is a quadric surface that is obtained by rotating an ellipse around one of its axes. Equation 4.1 can be adapted to describe an ellipsoid (3D) with the addition of a third term:

$$\frac{z^2}{a^2} + \frac{x^2 + y^2}{b^2} = 1. \tag{4.2}$$

The general form for a second-order polynomial of any conic section can be written as:

$$Ax^2 + 2Bxy + Cy^2 + 2Dx + 2Ey + F = 0 \tag{4.3}$$

and so they can be described using the general equation for a quadric surface (i.e a root of a polynomial of degree two in three variables):

$$Ax^2 + By^2 + Cz^2 + 2Dxy + 2Exz + 2Fyz + 2Gx + 2Hy + 2Iz + J = 0 \tag{4.4}$$

which is one of the input formats allowed by GRASP. To define an elliptical mirror, an ellipsoid of the correct shape must be constructed, then manipulated, so that the section of the shape that describes the mirror can be selected by defining the rim along a plane perpendicular to the local z-axis. Using the matrix form for the quadric equation allows a simple way to do this translation and rotation before reading the surface into GRASP. The matrix form of a general quadric equation is given by:

$$X^T Q X = 0 \tag{4.5}$$

where

$$X = \begin{bmatrix} x \\ y \\ z \\ 1 \end{bmatrix}, X^T = \begin{bmatrix} x & y & z & 1 \end{bmatrix}, Q = \begin{bmatrix} A & D & E & G \\ D & B & F & H \\ E & F & C & I \\ G & H & I & J \end{bmatrix} \tag{4.6}$$

and x, y and z are coordinates of a point on the surface.

Defining an ellipsoid centred at the origin of the coordinate system, Q becomes:

$$Q = \begin{bmatrix} A & 0 & 0 & 0 \\ 0 & B & 0 & 0 \\ 0 & 0 & C & 0 \\ 0 & 0 & 0 & J \end{bmatrix} \tag{4.7}$$

A, B and C each relate to an axis of the coordinate system. If we define the ellipsoid with its major axis lying along the z axis (as GRASP does before rotation, see figure 4.1), A and B are both equal and related to the length of the semi-minor axis and C relates to the semi-major axis. From equation 4.2, $A = B = \frac{1}{b^2}$ and $C = \frac{1}{a^2}$. J is equal to +1. Solving equation 4.5 across ranges for x, y and z forms an ellipsoid as can be seen in figure 4.3. In this example $A = B = 0.0000549079$ mm^{-2} and $C = 0.0000149358$ mm^{-2}. These numbers relate to mirror CM_02 of the 4 mm channel of the Onsala Space Observatory previously described in Chapter 3.
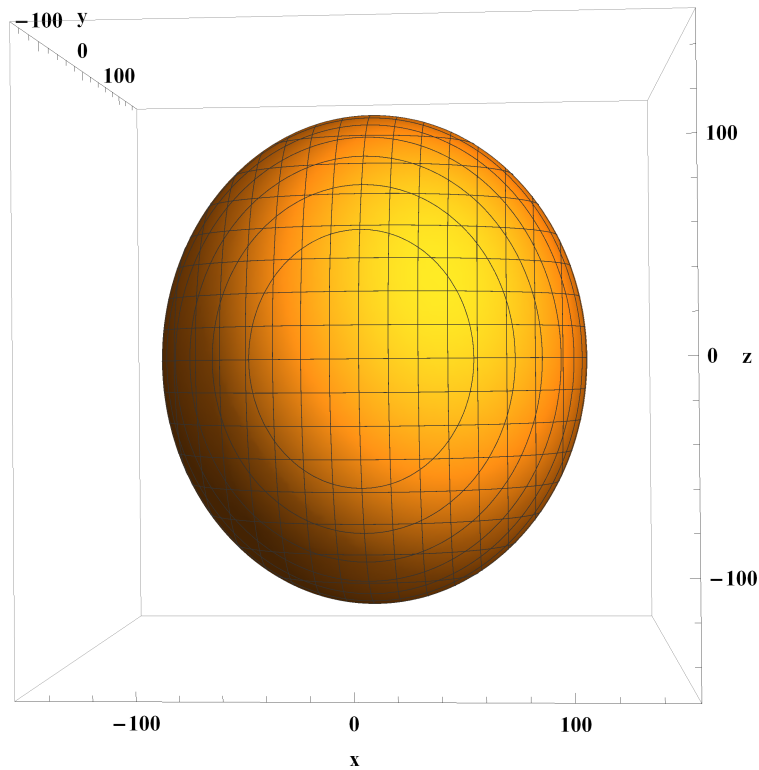
Figure 4.3: Ellipsoid generated in Wolfram Mathematica

The ellipsoid in figure 4.3 was constructed using the computer software Wolfram Mathematica [Wolfram Research]. This program was used for the initial construction of the mirror shapes used in this chapter. The following section will outline the steps taken to construct the required surface for the mirror, including orientation, and then how these were tabulated and implemented in GRASP.

4.2.2   Translation and Rotation

As just described the initial matrix equation for an ellipsoid with its major axis along the z-axis, which is also the axis of revolution, is

$$\begin{bmatrix} x \\ y \\ z \\ 1 \end{bmatrix}^{T} \cdot \begin{bmatrix} A & 0 & 0 & 0 \\ 0 & B & 0 & 0 \\ 0 & 0 & C & 0 \\ 0 & 0 & 0 & J \end{bmatrix} \cdot \begin{bmatrix} x \\ y \\ z \\ 1 \end{bmatrix} = 0 \tag{4.8}$$

where:

$$A = B = \frac{1}{b^2} = \frac{1}{c^2 - a^2} \tag{4.9}$$

$$C = \frac{1}{a^2} \tag{4.10}$$

$$J = 1 \tag{4.11}$$

In GRASP's canonical ellipsoid definition, the vertex distance $2a$ and the focal distance $2c$ are used.

Once the initial ellipsoid matrix is created, translation and rotational matrices are applied to it so that the correct section of the ellipsoid can be oriented as required within GRASP. In GRASP this requires a shift of $\Delta = c$ along the z-axis (see figure 4.4).
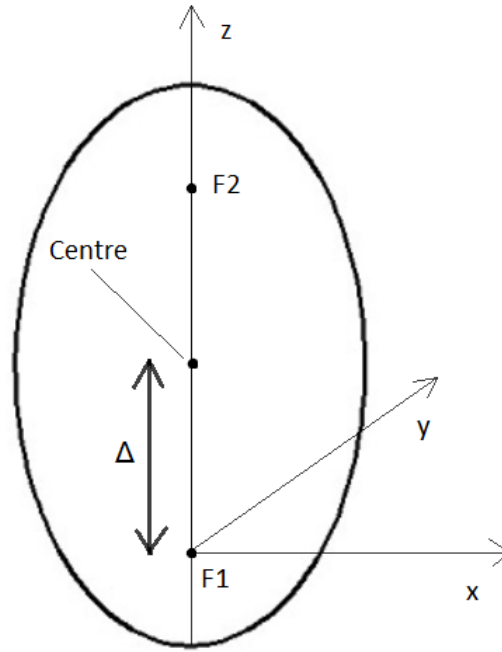
Figure 4.4: Shifting local coordinates of an ellipse

The translation matrix for this is:

$$
\left[
\begin{array}{ccc|c}
1 & 0 & 0 & 0 \\
0 & 1 & 0 & 0 \\
0 & 0 & 1 & \Delta \\
\hline
0 & 0 & 0 & 1
\end{array}
\right]
\tag{4.12}
$$

The translation matrix is first applied to the ellipsoid so that the corresponding equation is one that is centred on a focal point of the ellipse rather than its centre.

$$
\left[
\begin{array}{c}
x \\ y \\ z \\ 1
\end{array}
\right]^{T}
\cdot
\left[
\begin{array}{ccc|c}
1 & 0 & 0 & 0 \\
0 & 1 & 0 & 0 \\
0 & 0 & 1 & \Delta \\
\hline
0 & 0 & 0 & 1
\end{array}
\right]^{T}
\cdot
\left[
\begin{array}{cccc}
A & 0 & 0 & 0 \\
0 & B & 0 & 0 \\
0 & 0 & C & 0 \\
0 & 0 & 0 & J
\end{array}
\right]
\cdot
\left[
\begin{array}{ccc|c}
1 & 0 & 0 & 0 \\
0 & 1 & 0 & 0 \\
0 & 0 & 1 & \Delta \\
\hline
0 & 0 & 0 & 1
\end{array}
\right]
\cdot
\left[
\begin{array}{c}
x \\ y \\ z \\ 1
\end{array}
\right]
= 0
\tag{4.13}
$$

With the ellipsoid now defined with respect to a coordinate system centred on a

focal point, it is necessary to rotate it until the section of the shape that the mirror is to be made from is centred along the coring (local z) axis of the ellipsoid. As previously mentioned in Chapter 2, GRASP requires both a surface and a rim to create a scatterer. The rim is similar to a "cookie cutter" that cores out a desired section of an implemented shape. The rotational matrix is formed using the angle at which the ellipsoid is to be rotated. This can be around one or more axes. The rotational matrix for each axis can be seen here:

$$R_x\theta = \left[\begin{array}{ccc|c} 1 & 0 & 0 & 0 \\ 0 & \cos\theta & -\sin\theta & 0 \\ 0 & \sin\theta & \cos\theta & 0 \\ \hline 0 & 0 & 0 & 1 \end{array}\right]$$

$$R_y\theta = \left[\begin{array}{ccc|c} \cos\theta & 0 & \sin\theta & 0 \\ 0 & 1 & 0 & 0 \\ -\sin\theta & 0 & \cos\theta & 0 \\ \hline 0 & 0 & 0 & 1 \end{array}\right] \tag{4.14}$$

$$R_z\theta = \left[\begin{array}{ccc|c} \cos\theta & -\sin\theta & 0 & 0 \\ \sin\theta & \cos\theta & 0 & 0 \\ 0 & 0 & 1 & 0 \\ \hline 0 & 0 & 0 & 1 \end{array}\right]$$

These can then be included into the ellipsoid equation like so:

$$
\begin{bmatrix} x \\ y \\ z \\ 1 \end{bmatrix}^T \cdot \left[\begin{array}{ccc|c} 1 & 0 & 0 & 0 \\ 0 & 1 & 0 & 0 \\ 0 & 0 & 1 & \Delta \\ \hline 0 & 0 & 0 & 1 \end{array} \right]^T \cdot \begin{bmatrix} Rotational \\ Matrix \end{bmatrix}^T \cdot
$$

$$
\begin{bmatrix} A & 0 & 0 & 0 \\ 0 & B & 0 & 0 \\ 0 & 0 & C & 0 \\ 0 & 0 & 0 & -1 \end{bmatrix} \cdot \begin{bmatrix} Rotational \\ Matrix \end{bmatrix} \cdot \left[\begin{array}{ccc|c} 1 & 0 & 0 & 0 \\ 0 & 1 & 0 & 0 \\ 0 & 0 & 1 & \Delta \\ \hline 0 & 0 & 0 & 1 \end{array} \right] \cdot \begin{bmatrix} x \\ y \\ z \\ 1 \end{bmatrix} = 0
$$

(4.15)

where [Rotational Matrix] corresponds to the appropriate matrix or combination of matrices from 4.14. Figure 4.5 shows a translated and rotated ellipsoid constructed using this method. In this case the ellipse was translated by $\Delta = 63.803$ mm and rotated by $154.605°$.
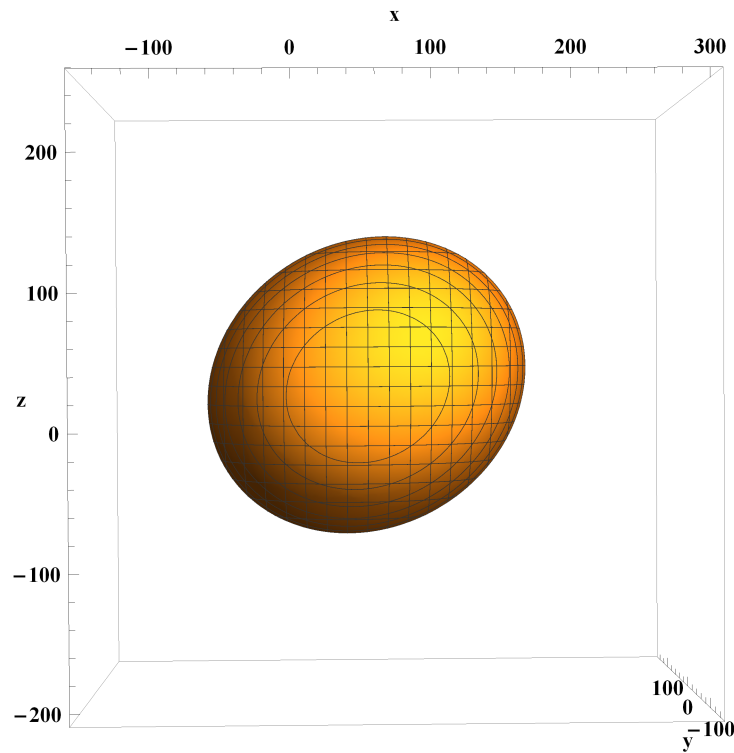
Figure 4.5: Ellipsoid after it has been translated and rotated around the y-axis, here the angle of rotation was 154.605°

Once the ellipsoid had been constructed and a corresponding equation formed, it was rearranged to solve for z as a function of x and y. Using this equation it was possible to create the table of data required for GRASP (Appendix C).

4.3   Implementation in GRASP

Implementation of a tabulated surface in GRASP requires a table of data points (x, y, z) on the surface to be generated as just described. The software then interpolates in between each point to knit together a whole surface. The file type required is called an *.sfc* file and they are of the format outlined in table 4.1

File Line	Contents
Line 1	**Text** - Record with identification text
Line 2	**Number of points** - Number of (x,y,z) points in file
Line 3...	$x(\text{i}),y(\text{i}),z(\text{i})$ - The x,y,z coordinates for the i'th point

Table 4.1: File format for irregular xy-grid input into GRASP

Once the file was constructed it could be imported into GRASP. To do this, GRASP requires you to first define a coordinate system whose origin is designated as $(0,0,0)$. The file and the units of the data points are selected and GRASP plots the surface.

4.4   Generation of Random Surface Errors

The surface created within GRASP as just described is perfect (assuming the sampling is sufficiently high) and certainly much smoother than is actually possible by manufacturing in real life. If the initial sampling is low enough when constructing the table, imperfections can be apparent due to the interpolation used by software, however these errors are usually easily spotted and reduced with increased sampling. In this section I discuss the generation of "errors" that, when added to the perfect surface, represent realistic manufacturing errors and surface roughness.

Surface errors can be added to the mirrors by generating a grid of random numbers and adding them to the ideal surfaces already generated. These random numbers could be drawn from e.g a uniform or normal (Gaussian) distribution. A random variable χ is said to be normally distributed with mean (expectation value $E[\chi]$) μ and variance σ^2 if its probability density function is given by

$$f_\chi(\chi) = \frac{1}{\sqrt{2\pi}\sigma}e^{[\frac{(\chi-\mu)^2}{2\sigma^2}]}.$$

(4.16)

It was decided to use such Gaussian random variables to simulate mirror surface roughness. Real surface features, however have some finite spatial scale and with a simple grid of random numbers this scale would be forced to equal the grid spacing.

The spatial size of features in a random field can be usefully described by its covariance function, a measure of the similarity between values at grid points a certain distance apart. If X and Y are random variables with means μ_x and μ_y then the covariance of X and Y is defined as

$$cov(X, Y) = E[(X - \mu_x)(Y - \mu_y)]. \tag{4.17}$$

Random surface features of finite size were generated by following the method of Kroese and Botev [Kroese and Botev, 2013] for generating stationary Gaussian processes (or fields) via circulant embedding. A stationary process is one in which the expectation function is constant and the covariance function is invariant under translation. The method generates a stationary spatial Gaussian field on the unit torus (i.e the unit square $[0, 1] \times [0, 1]$ in which points on the opposite sides are the same). The code is given in Appendix D.

A zero-mean Gaussian random field was generated with a Gaussian covariance function

$$cov(X_s, X_t) = e^{(-c^2 \|\vec{s} - \vec{t}\|^2)} \tag{4.18}$$

where $\|\vec{s} - \vec{t}\|$ is the distance between points on the grid. The coherence length (c^{-1}) could be varied to simulate surface errors of different spatial scales. Examples of Gaussian fields generated using this method are shown below
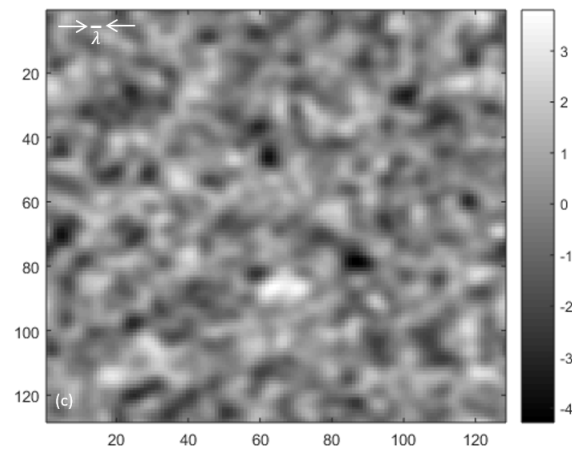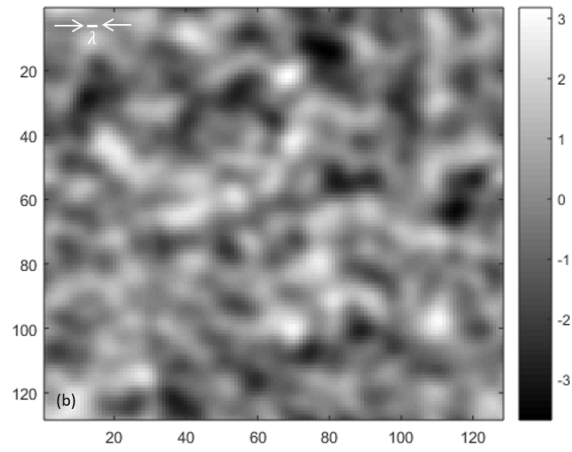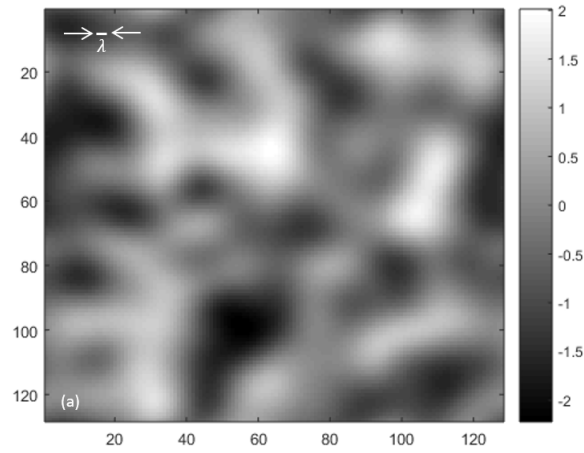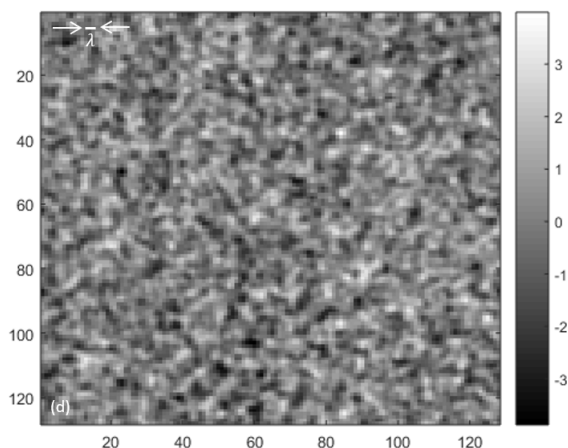
Figure 4.6: Gaussian random field (128×128) with coherence length $c^{-1} = (a)1/100, (b)1/500(c)1/1000$ and $(d)1/5000$. These fields were used to generate surface errors over a 200 mm $\times$ 200 mm section of the ellipsoidal mirrors. The corresponding size of λ is shown for 67 GHz.

4.5   Effect of Simulated Errors on Mirror Surfaces

4.5.1   Random Errors

The Onsala 4-mm channel was used as an example optical system to test the effect of random surface errors (there is no evidence that such features are an issue for the real system). The receiver horn and the two ellipsoidal mirrors CM_01 and CM_02 were set-up in GRASP as by generating a table of (x, y, z) points on their surface using the technique described in the previous section. For this test a grid of 128 $\times$ 128 points was generated covering an area of 200 mm $\times$ 200 mm in the xy plane in each case (figure 4.7). This is further reduced in GRASP by the mirror rim ($r = 80$ mm for CM_01 and $r = 70$ mm for CM_02). The system is shown in figure 4.8 (left), no cryostat or flat mirror apertures were used for these tests. The grid of "error" points was then scaled by some factor and added to the surface z values to generate a rough surface (the surface errors are therefore defined to be along the local z-axis, i.e. pepedicular to the plane of the rim). The effect on the rays in GRASP's layout

diagram is clear in figure 4.8 (right). A frequency of 67 GHz and various scaling factors from $\frac{\lambda}{20}$ to $\frac{\lambda}{60}$ were used.
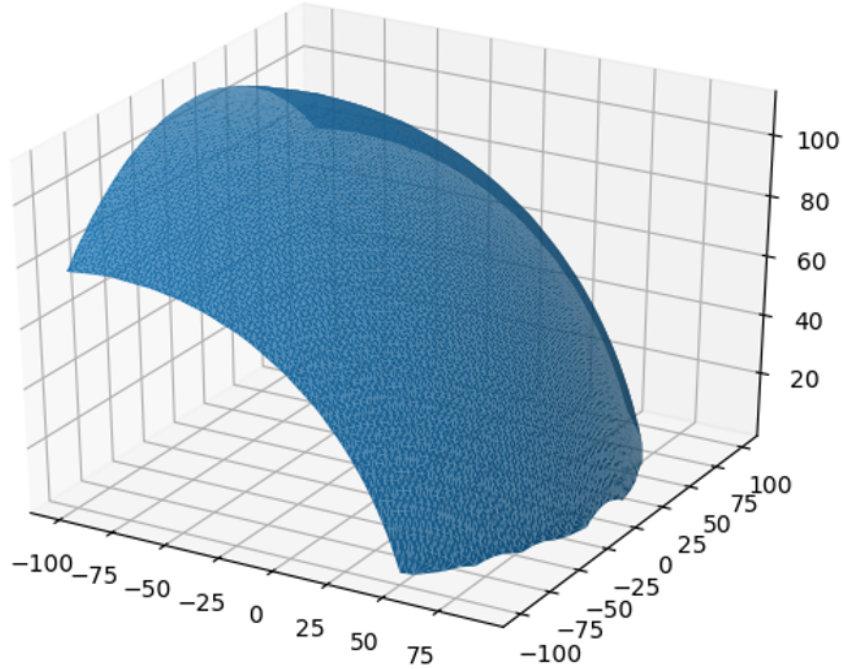

Figure 4.7: Grid of points generated for the ellipsoidal mirror CM_01. The random surface errors added are too small to be easily visible on a plot such as this.

Ruze theory [Ruze, 1966] deals with surface errors which are small with respect to the wavelength and are randomly distributed over the reflector surface. The beam pattern from such a reflector depends on many factors such as the *rms* surface error $\frac{\sigma}{\lambda}$, its curvature, the error correlation length, and whether it changes, and the illumination of the aperture. There are many approximations in the literature that are useful under different circumstances. In general surface irregularities have two effects: they reduce the axial gain (by a factor $e^{[-(\frac{4\pi\sigma}{\lambda})^2]}$ in the case of a parabolic reflector) and they produce an error beam surrounding the main beam.
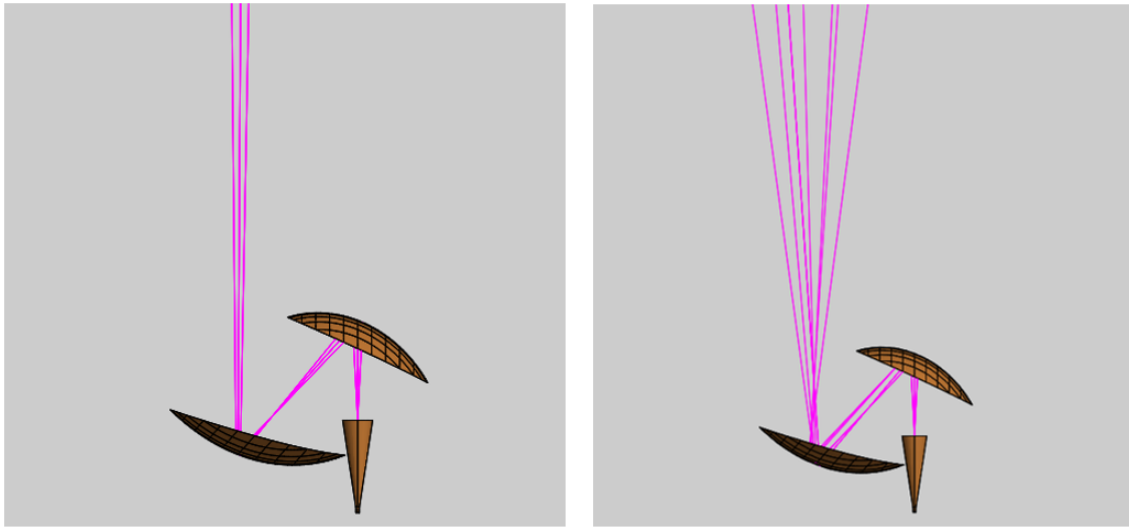
Figure 4.8: The OSO 4-mm test system as laid out in GRASP with (left) perfect and (right) rough mirrors.

Five simulations were carried out, first with small random errors of $\frac{\sigma}{\lambda} = \frac{1}{40}$ and a short coherence length of $c^{-1} = 1/5000$. A cut through the beams at the subreflector plane are showed in figure 4.9 and compared with the beam with no surface errors added. A reduction in on-axis gain and small variation in beam shape, as expected from Ruze theory, can be seen. The drop in gain becomes significant as the height of the surface errors increases, even at $\frac{\lambda}{20}$ (often used as a rule-of-thumb for polishing mirrors) and in particular as the spatial size of the surface features becomes large compared with wavelength. The variation from one simulation to the next is also large. Some beam plot cuts are shown in figures 4.9 to 4.12. The 2D beam plots in figures 4.13 to 4.16 show how beam errors increase with the rms error size and their correlation length c^{-1}.
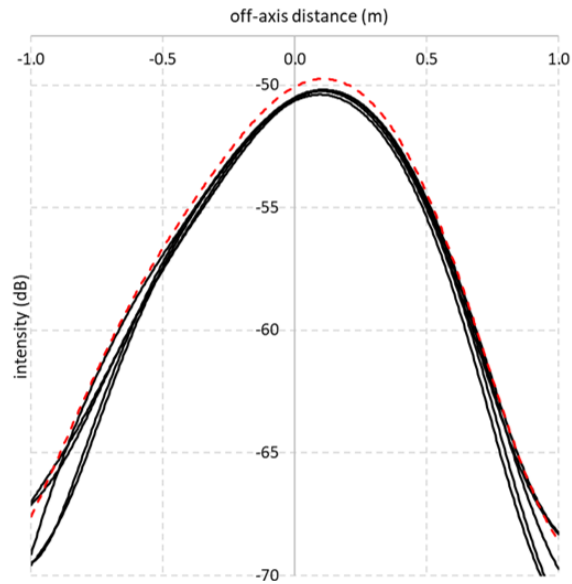
Figure 4.9: Cut through the beam pattern at the subreflector plane when random surface errors with $\sigma = \frac{\lambda}{40}$ and $c^{-1} = \frac{1}{5000}$ are added to each mirror. The beam from the nominal system with perfect mirrors is shown with a red dashed line.
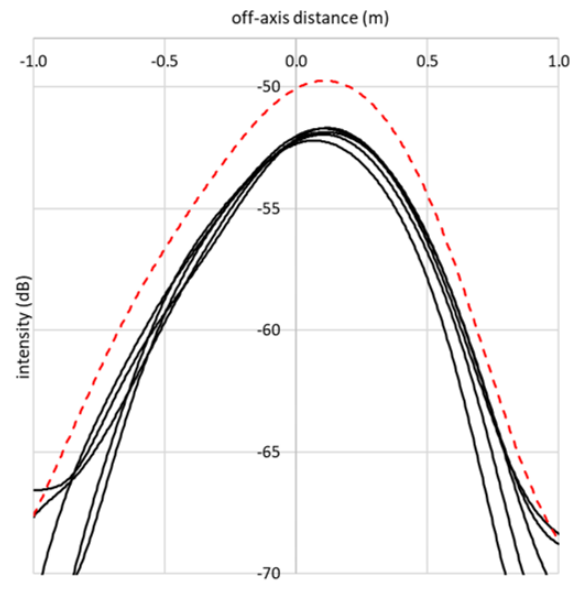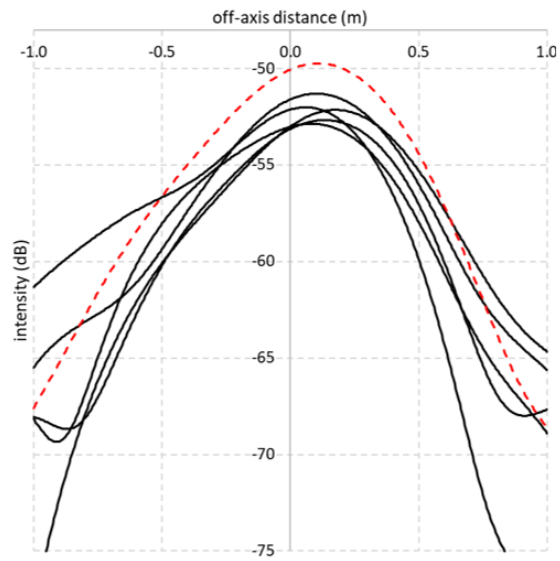

Figure 4.10: Cut through the beam pattern at the subreflector plane when random surface errors with $\sigma = \frac{\lambda}{20}$ and $c^{-1} = \frac{1}{5000}$ are added to each mirror. The beam from the nominal system with perfect mirrors is shown with a red dashed line.

Figure 4.11: Cut through the beam pattern at the subreflector plane when random surface errors with $\sigma = \frac{\lambda}{20}$ and $c^{-1} = \frac{1}{1000}$ are added to each mirror. The beam from the nominal system with perfect mirrors is shown with a red dashed line.
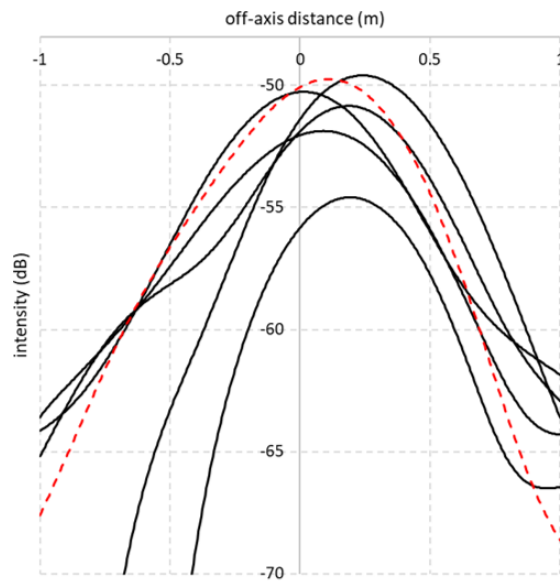

Figure 4.12: Cut through the beam pattern at the subreflector plane when random surface errors with $\sigma = \frac{\lambda}{20}$ and $c^{-1} = \frac{1}{100}$ are added to each mirror. The beam from the nominal system with perfect mirrors is shown with a red dashed line.

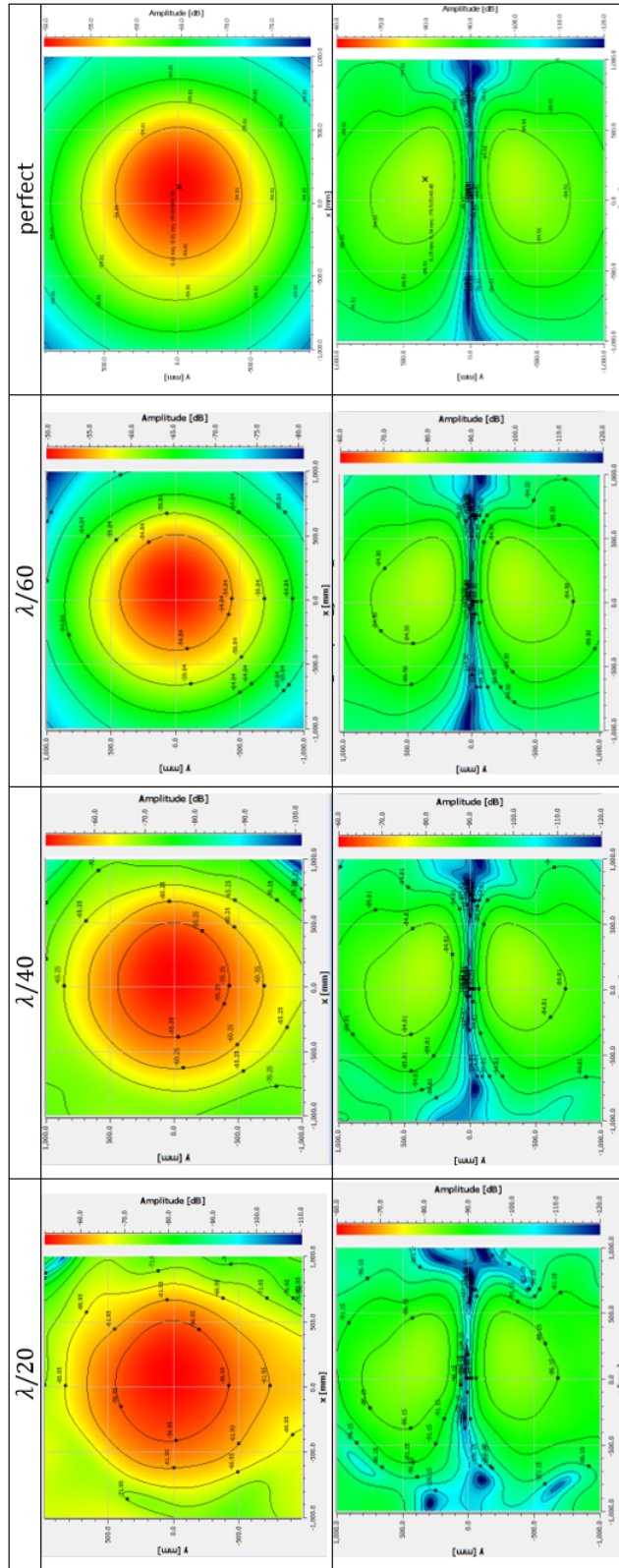Below are plots of the beam at the subreflector.

Figure 4.13: Co- and cross-polar plots of the beam when random errors of coherence length $c^{-1} = 5000$ (single realisation) were added to mirrors CM_01 and CM_02. The mean amplitude of the surface errors are given in the first row of the table and a simulation with perfect surfaces is included for comparison.

Figure 4.14: Co- and cross-polar plots of the beam when random errors of coherence length $c^{-1} = 1000$ (single realisation) were added to mirrors CM_01 and CM_02. The mean amplitude of the surface errors are given in the first row of the table and a simulation with perfect surfaces is included for comparison.
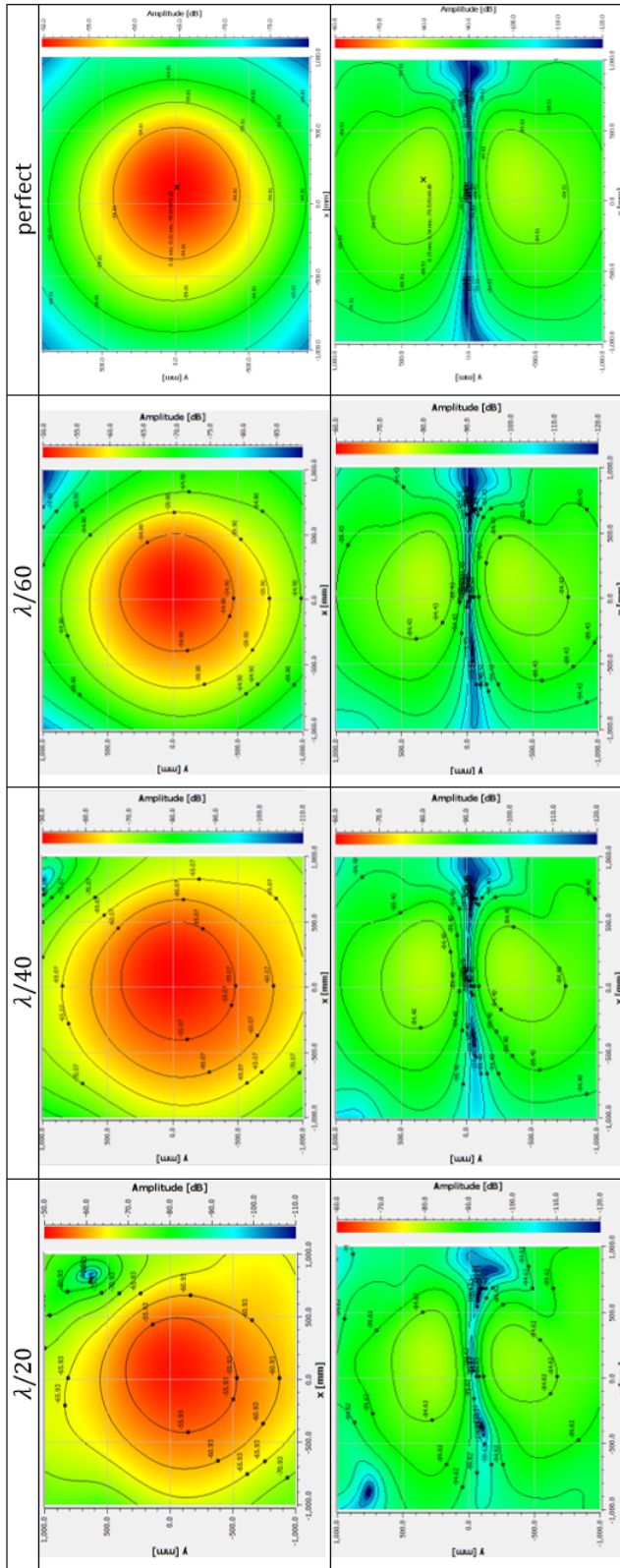
Figure 4.15: Co- and cross-polar plots of the beam when random errors of coherence length $c^{-1} = 500$ (single realisation) were added to mirrors CM_01 and CM_02. The mean amplitude of the surface errors are given in the first row of the table and a simulation with perfect surfaces is included for comparison.
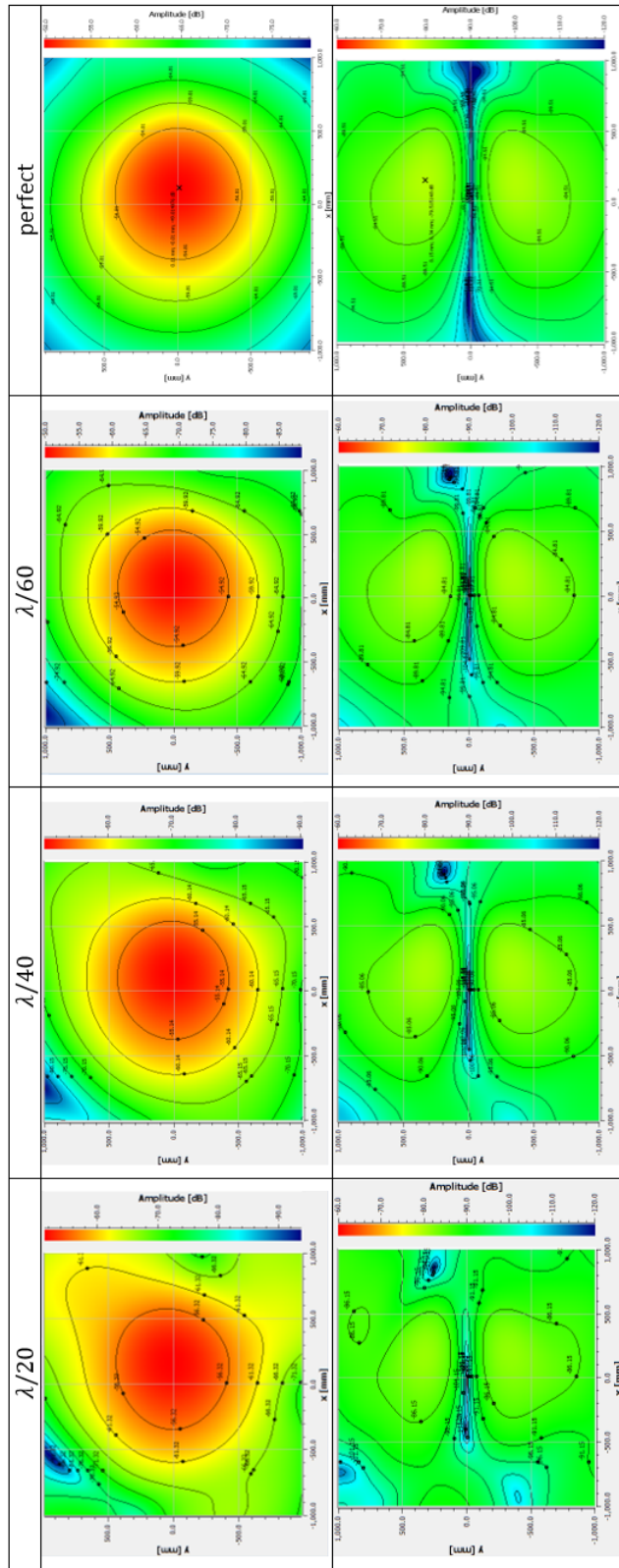
Figure 4.16: Co- and cross-polar plots of the beam when random errors of coherence length $c^{-1} = 100$ (single realisation) were added to mirrors CM_01 and CM_02. The mean amplitude of the surface errors are given in the first row of the table and a simulation with perfect surfaces is included for comparison.
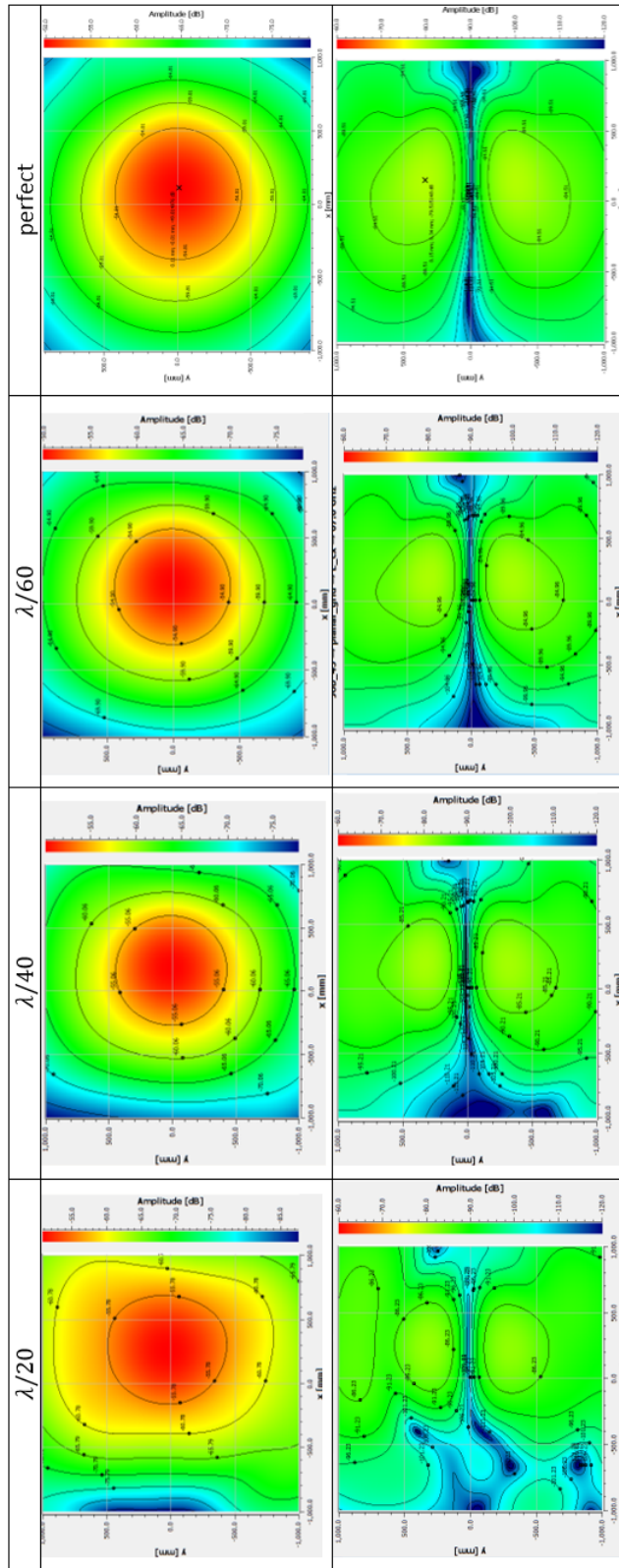
4.5.2   Systematic Errors

It was then decided to test the effect of a specific surface feature rather than surface roughness. The idea arose from work on the QUBIC [Battistelli et al., 2011] project in Maynooth when it was believed that one of the telescope mirrors had a raised ring feature. Careful measurement later showed that this particular mirror surface was in fact manufactured correctly.

Plots of some ring features tested are shown in Figure 4.18. The features were added to mirror CM_02 and correspond to a beam edge taper of -1.75 dB and -8.6 dB for the small and large ring, respectively. They were designed to occur close enough to the mirror centre for the beam to be still reasonably strong. The mirror was in the near field of the source beam and the beam shape was a shown in Figure 3.13. The OSO 4-mm channel system proved to be quite forgiving of a feature such as this with an error up to $\frac{\lambda}{10}$ or more in height being needed to see differences in the subreflector beam clearly (figure 4.17 to 4.18) for both the small and large ring.
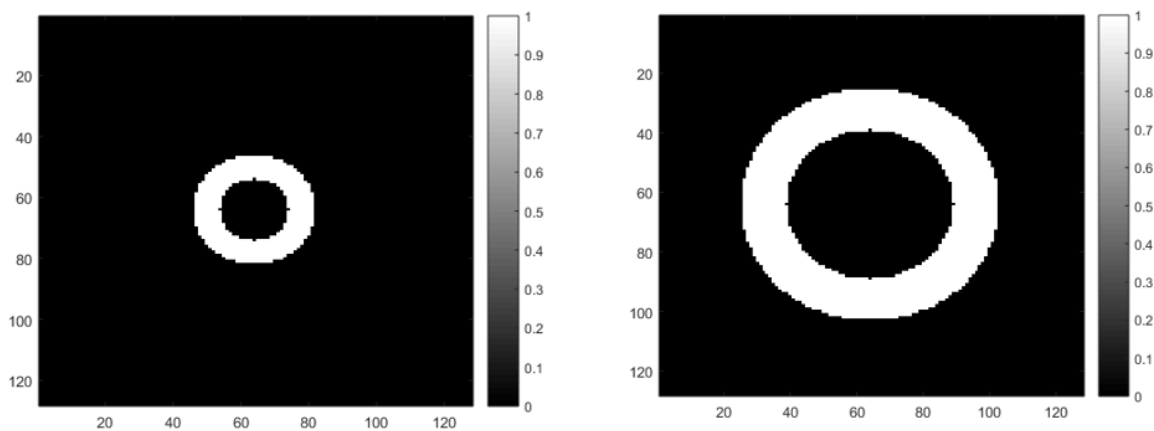

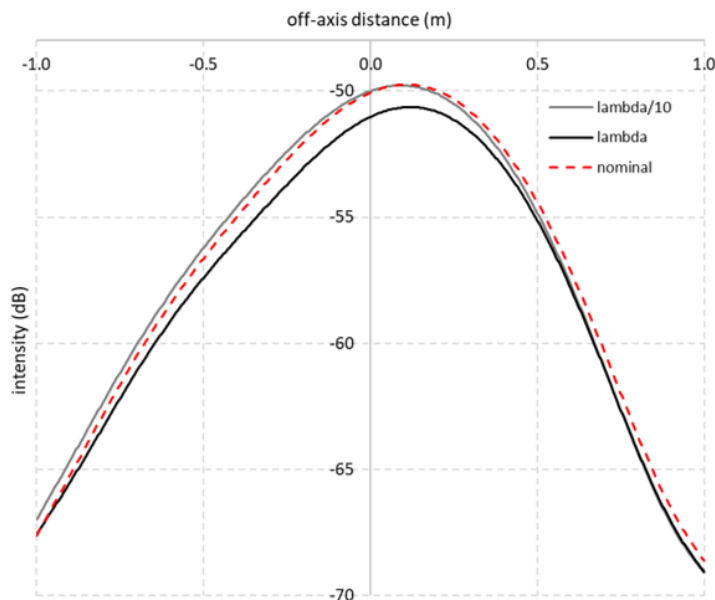**Figure 4.17:** Small and Large ring error added to the surface of CM_02

Figure 4.18: Beam pattern obtained when $\frac{\lambda}{10}$ and λ height ring features were added to the CM_02 mirror of the OSO 4-mm channel.

4.6   Summary and Conclusion

In this chapter I described the process of modelling mirror surfaces in GRASP using tabulated surfaces. Using this process allowed random surface errors to be easily added. The errors were generated using Gaussian random numbers found using a method devised by Kroese and Botev [Kroese and Botev, 2013]. These were then added to the surfaces of the OSO 4-mm telescope in GRASP and the resulting beams were compared to the perfect mirror model. Systematic errors were then investigated, namely the effect of a ring support causing the mirror to become flexed.

The effect of random errors across a mirror surface was first analysed. The generated errors were created using different coherence lengths, $\frac{1}{100}$, $\frac{1}{500}$, $\frac{1}{1000}$ and $\frac{1}{5000}$ (where 128 corresponds to the mirror size), and each of these were scaled by $\frac{\lambda}{20}$, $\frac{\lambda}{40}$ and $\frac{\lambda}{60}$. Comparing the beam plots and their patterns at the sub reflector, we

see distortions in the beam increase with increasing rms size and correlation length.

The mirror system of the 4 mm proved to be relatively tolerant of a ring feature, added to CM_02, requiring a scaling of $\frac{\lambda}{10}$ to see a noticeable effect on the beam's shape.

Chapter 5

The Vector Network Analyser: Calibration, Alignment and Analysis

5.1 Introduction

Several staff members in the Maynooth University Department of Experimental Physics work in the area of Terehartz imaging and this often involves the design of feed horns, lenses and other optical elements. Theoretical models of the performance of these components need to be verified and for this a Vector Network Analyser (VNA) is often used. A VNA contains both a source of radiation and a set of receivers that are used to measure the reflected and transmitted signal between the heads as it interacts with a device-under-test (DUT). The VNA is controlled by software written in a software development program called LabVIEW.

Before the VNA can be used for measurements, however, it must be calibrated and aligned. Calibration is done using a particular procedure which requires standardised components that produce known results. The most widely used calibration

procedure for the VNA is known as TOSM (Through , Offset, Short and Match). After calibration, the DUT system must be aligned and for this an automated fitting procedure is used. In this chapter I will describe these procedures and work that was done to test and streamline the alignment. Finally the VNA was used to test the new circular and rectangular waveguide probes that were designed for the system.

5.1.1   S-Parameters

In the S-parameter approach, common in RF and microwave engineering, component properties such as transmission and reflection coefficients, return loss and gain are expressed in terms of an S-parameter matrix that describes the response of the component to applied signals (see e.g [Hiebel, 2007]). The component, or set of components, is considered a 'black box' that interacts with the rest of a network via ports. The S-parameter matrix for a 2-port network (port 1 and port 2) is a 2×2 matrix that describes the relationship between the reflected and incident power at the two ports. If the transmitted and reflected powers are labelled $a_{1,2}$ and $b_{1,2}$ respectively (see figure 5.1) then

$$\begin{pmatrix} b_1 \\ b_2 \end{pmatrix} = \begin{pmatrix} S_{11} & S_{12} \\ S_{21} & S_{22} \end{pmatrix} \begin{pmatrix} a_1 \\ a_2 \end{pmatrix} \tag{5.1}$$

S_{11}, for example, is the input port reflection coefficient and S_{22} is the forward transmission coefficient.
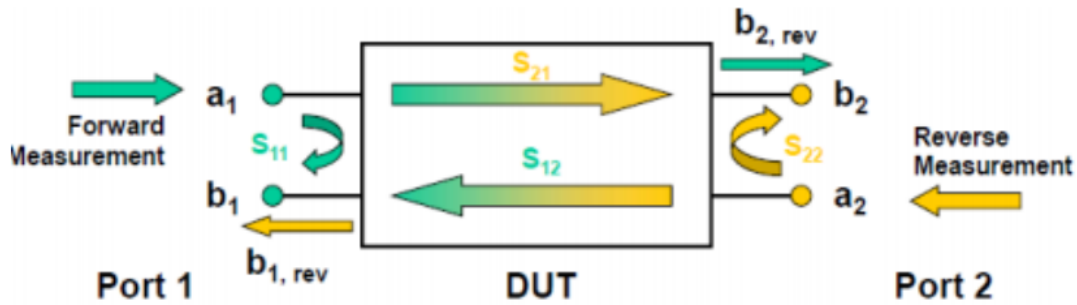
Figure 5.1: Incident and reflected power at a 2-port device (image from [Hiebel, 2007])

5.1.2   VNA

The VNA used in the Department of Experimental Physics is a ZVA-24 Rohde and Schwarz Vector Network Analyser [Hiebel, 2007]. The VNA is connected to two heads which operate at W band frequencies (75 GHz - 110 GHz). These heads can be moved around the laboratory bench and mounted in a number of positions. While each head both transmits and receives it is useful to consider one of the heads as a transmitting port (head 1) while the other acts as a receiver (head 2). For the measurements taken in this report, head 1 was placed on an XY scanner while head 2 was free to be moved along a translation stage in the z axis. The basic set up can be seen in figure 5.2.
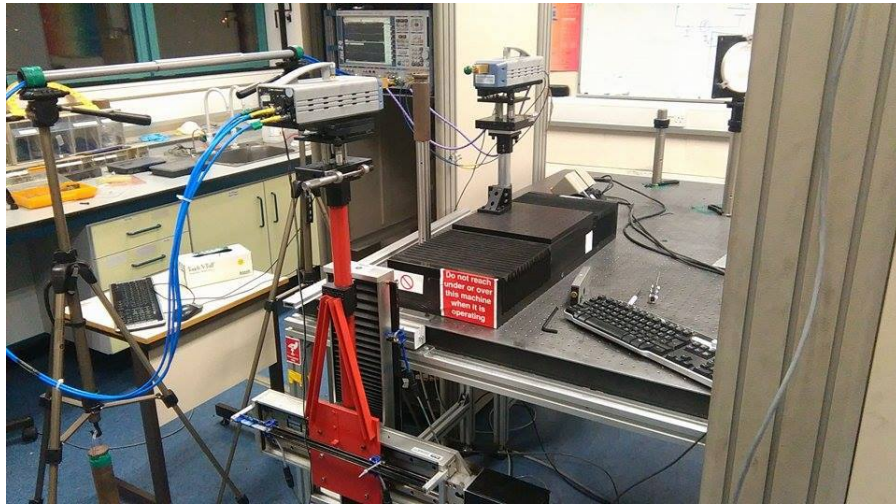
Figure 5.2: Set up of head 1(foreground) and head 2 (background).

When the VNA makes a measurement of the radiation transmitted by (or reflected from) a DUT, it saves it as a complex S-parameter and so both the amplitude and phase of the signal can be measured. A 2D image can be recovered by scanning the source, head 1, over the XY plane. Motion of the detector, head 2, along the z-axis can be used to reduce the effect of standing waves. Proper alignment of the system is critical for accurate measurements. Some of the measurements in this chapter relate to free-space propagation rather than a specific DUT, but the principles are the same.

5.1.3   LabVIEW

Laboratory Virtual Instrument Engineering Workbench (LabVIEW)[National Instruments, 2003] is a "block" diagram coding software program that uses visual representations of tasks for a programming language. Developed by National Instruments, it is a language that is commonly used for the automation and control of measuring instruments and for data acquisition. This makes it a convenient tool to use with the VNA as it allows broad control over the automation of the instrument while also allowing the user a choice of the information and data to be gathered.

In the development stage of LabVIEW code, the user is presented with two windows: the front panel and the block diagram. The front panel acts as the user interface and here the programmer can place the initial building blocks for the program such as controls and indicators. These can be seen in figure 5.3. Controls allow a user to enter data into the program while indicators give output values.
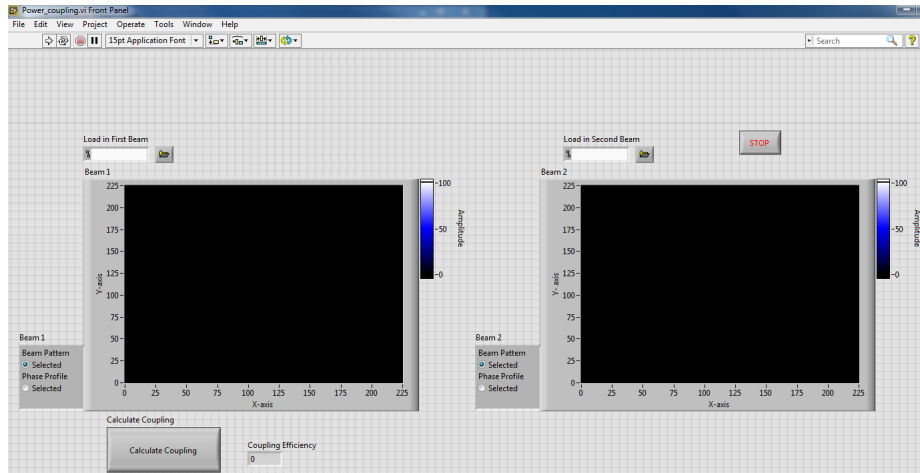

Figure 5.3: Example of a front panel window in LabVIEW

This front panel allows a skeleton of the code being developed to be easily written as each control and indicator is recreated on the block diagram. The developer uses wires to link these with different functioning nodes. The order of execution of a program is determined by the structure of the functional nodes used within the block diagram. These nodes can have a differing number of input and output terminals depending on their function. Loops can be created by using loop frames that overlap the functions required. An example of one of these block diagrams can be seen in figure 5.4.
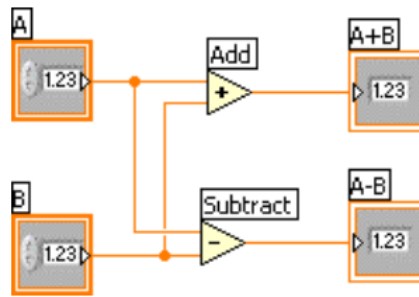
Figure 5.4: An example of a simple program to find the sum and difference of two numbers. The two input terminals (controls) are wired to an 'addition' node and to a 'subtraction' node. The output from this is then wired to the indicator blocks on the right.

One very practical aspect of LabVIEW is the creation of virtual instruments (VIs). These VIs are either pre created or custom created programs that carry out a certain function. Each VI comes with its own front panel and block diagram which can be tunnelled into. This tunnelling allows the user to enter a VI and customise it. The user can also create their own VI and create a bank of custom functions that can be further used in other more complex programs.

A Labview program, called GHOST, was designed by Marcin Gradziel of Maynooth University to control the VNA. This allows the user to both select the desired movement of the VNA and also what parameters are to be measured.

5.2   Calibration

Careful calibration must be carried out before measurements can be taken with the VNA. As it is a very sensitive system, even its own internal thermal electrical eddies can act as noise on any measurements taken. As earlier stated, we use the calibration method TOSM to account for this [Rytting, 1998].

5.2.1   Initial Setup

Both heads of the VNA are turned on roughly five hours prior to the calibration process. This allows the internal thermals to steady. Power is lost in the cables connecting the head ports to the VNA but this can be compensated for by increasing the VNA power output level. In our case it was found that using 10 dB for a set of long cables or 7 dB for a set of shorter cables, depending on which was being used, gave a good signal level.

The next step is to set the frequency range, step size and bandwidth. The default frequency range is 75 GHz – 100 GHz and the default frequency step size is 100 MHz. The measurement bandwidth is usually set to 100 MHz for co-polar scans and 10 Hz for cross-polar. With the configuration set, the TOSM calibration, described next, is then carried out.

5.2.2   Through, Offset, Short and Match (TOSM)

Before measuring the S-parameters of a DUT, both VNA ports must be calibrated in order to correct for system errors. Different calibration methods are used depending on the error model adopted. The most common method employed is TOSM which uses a 12-term error model (six forward and six reverse error terms, see e.g. figure 5.5).
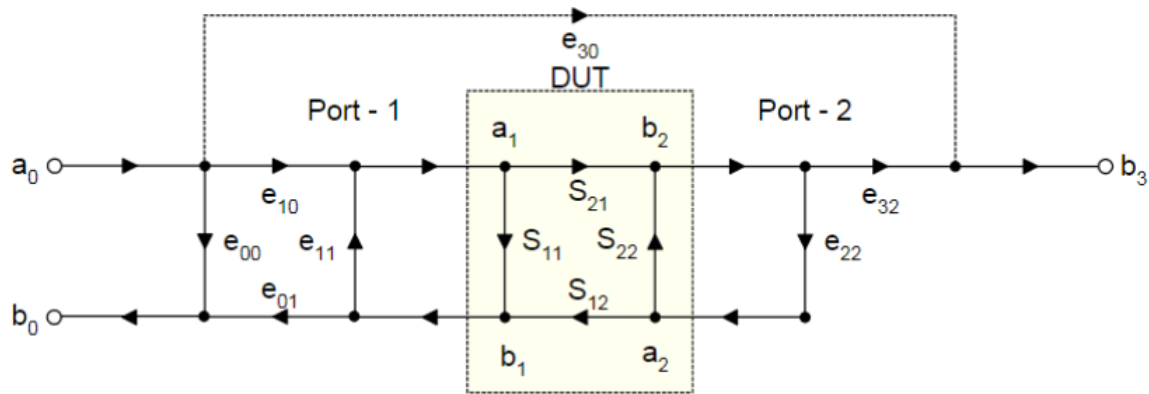
Figure 5.5: System error model for the forward direction. The six error terms are directivity (e_{00}), leakage/ isolation (e_{30}), reflection tracking ($e_{10}e_{01}$), transmission tracking ($e_{10}e_{32}$), Port-1 source match (e_{11}) and Port-2 load match (e_{22}). There is an equivalent model for the reverse direction[Rytting, 1998].

TOSM stands for Through, Offset, Short and Match. Each of these terms refers to a stage required in the calibration process. The offset, short and match are physical components that are connected to each head while 'through' is when the heads are directly connected to each other allowing for theoretically perfect transmission. The short (figure 5.6 (a)) is a device made of conductive metal that is characterized by 100% reflection of the signal. The match (5.6 (b)) contains a cone of absorbing material and is characterized by full absorption of the signal. The offset is a metal backplate that is placed onto the short. The length of the device causes a $\frac{\lambda}{4}$ shift in the signal at its central frequency. When combined with the short, the reflection coefficient has 180° phase at midband. Other calibration types differ in the number and types of standards used. For full correction, measurements are carried out in the forward ($a_2 = 0$) and reverse ($a_1 = 0$) directions. The VNA comes equipped with calibration software that uses the results of measurements made with each standard to compute the required error terms.
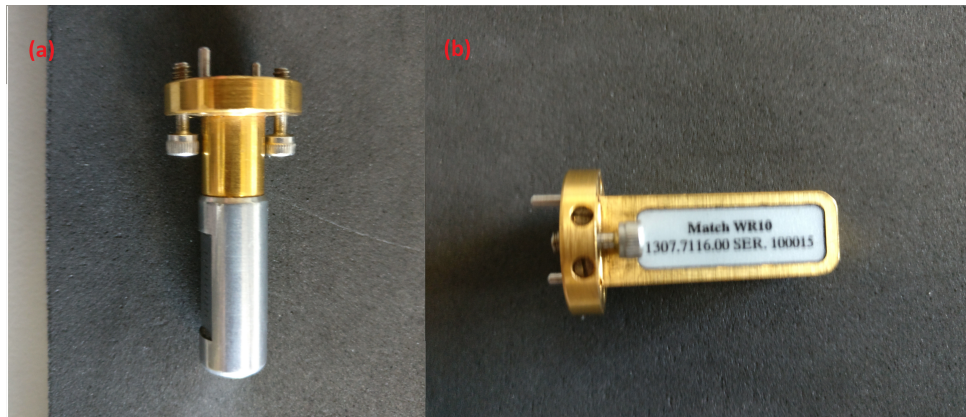
Figure 5.6: The (a) short and (b) match, device from the Rohde and Schwarz calibration kit.

The calibration procedure involves taking measurements after attaching the short to head 1, then with the offset placed at the back of the short and then with the match attached to head 1. These three measurements are then repeated for head 2. Finally, to perform the through calibration, the head 1 and head 2 waveguides are attached.

5.3   Alignment

One of the aims of the measurements outlined in this chapter was to test a new procedure to align the heads of the VNA [Tynan, 2016]. Due to the sensitivity of the system, alignment must be quite precise. There are two main components that must be aligned: the transmitting head (in this case head 2) must be aligned parallel to the z-axis translation stage along which it moves and this stage itself must be aligned orthogonally to the scanning plane of head 1. For these tests a horn was attached to the transmitting head on the z-axis and a measurement probe (WR10 rectangular guide) was attached to the other head which could scan in the xy plane.

5.3.1   Gaussian Fitter

The alignment process of the VNA heads is carried out using a LabVIEW program designed by Marcin Gradziel of Maynooth University. This program is designed to read in the S-parameter data received at the heads and to extract properties of the incident beam for each measurement frequency specified. The program does this by fitting a Gaussian amplitude profile and spherical phase front to the measured beam. Of the parameters that can be extracted from the fit, the four of interest here are the x and y coordinates of the beam centre, and the incident angles of the beam in the xz and yz planes (we refer to these as β and α). The incident angles are determined by the fit to the beam phase front. Figure 5.7 shows an example of the information displayed by the program and figure 5.8 shows the parameters extracted from a scan of the transmitting horn along the translation stage. In this case the data for the central frequency were used and the beam was measured at 13 positions of the transmitting head. Scans in the xy plane were typically taken over an area of 100 mm × 100 mm.

5.3.2   Alignment Process

The horn attached to the transmitting head of the VNA results in a beam at the xy plane that is approximately Gaussian in shape. The effects of any misalignment of the head to the translation stage and of the translation stage orthogonal to the xy plane are illustrated in the sketch in figure 5.9. If the head is mounted at an angle with respect to the translation stage, then, as the emitting horn is moved along that translation stage, the beam centre position on the xy plane changes, as was the case in figure 5.8. Geometry can be used to calculate the required adjustment to a tip-tilt stage on which the head is mounted and a further scan used to verify or refine this adjustment. The LINEST function in Excel was used to find a least-squares best fit to the slope of the beam direction.
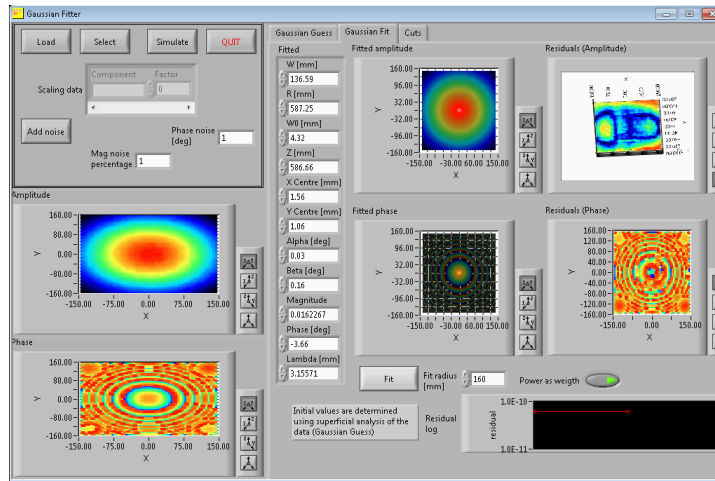
Figure 5.7: Interface for Gaussian fitter program developed in LabVIEW.

	A	B	C	D	E	F	G	H	I	J	K	L	M	N	O	P	Q
17					S12												
18	96 GHz	16/08/2016															
19	Z	W	R	w0	z	X_c	Y_c	α	β	Mag	Phase	Lambda		w0 avg	del Z	del Z avg	
20	0	82.02	363.5	4.4	362.45	-0.88	-2.4	0.07	0.05	0.027292	-2.23	3.12284		4.36	0	150	
21	25	88.16	388	4.37	387.04	-0.65	-2.59	0.07	0.08	0.025369	-33.75				25		
22	50	93.97	413	4.36	412.1	-0.36	-2.79	0.08	0.11	0.024142	-21.86				50		
23	75	99.69	431.4	4.36	436.56	-0.32	-2.7	0.05	0.11	0.022735	-99.06				75		
24	100	105.58	462.17	4.35	461.39	-0.46	-2.88	0.07	0.08	0.021387	-140.85				100		
25	125	111.54	485.29	4.32	484.56	-0.29	-3.21	0.07	0.1	0.02859	53.91				125		
26	150	118.04	512.99	4.32	512.31	-0.11	-2.92	0.03	0.11	0.01927	0.86				150		
27	175	123.9	538.22	4.32	537.57	0.01	-3.45	0.07	0.12	0.018354	1.03				175		
28	200	128.76	560.28	4.32	559.64	0.09	-2.86	0	0.12	0.001767	-335.67				200		
29	225	136.02	585.15	4.27	584.57	0.09	-3.03	0	0.12	0.016713	-348.89				225		
30	250	141.58	608.57	4.27	608.02	0.2	-3.09	0	0.12	0.016099	-516.93				250		
31	275	147.6	633.88	4.27	633.35	0.72	-3.25	-0.01	0.16	0.01547	-476.65				275		
32	300	153.03	657.74	4.27	657.23	0.71	-3.26	-0.01	0.15	0.014888	-242.35				300		
33																	
34			Xc			Yc			Avg B								
35			0.004673	-0.79703		-0.00238	-2.59846		0.11								
36			0.000411	0.072741		0.000577	0.101988										
37			0.921397	0.13878		0.608316	0.194581										
38									Del B								
39			Rad - Deg						-0.15772								
40			0.267716						Deg - RD								
41			Shift in X			Shift in Y			-0.00275	-2.24067							
42			0.408846			-0.20865											
43																	

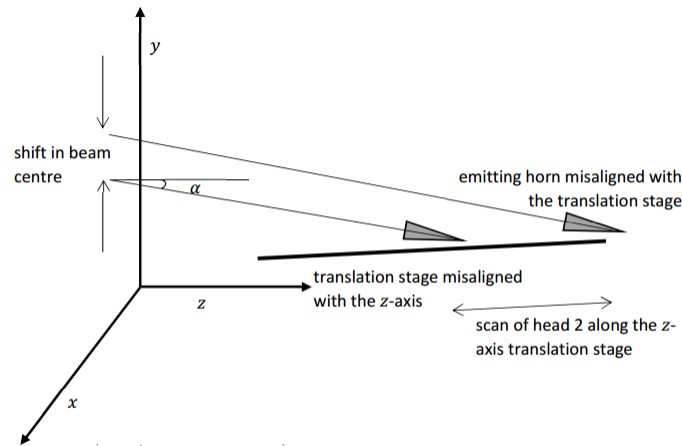**Figure 5.8:** Example of Excel spreadsheet with data taken from the Gaussian Fitter program.

Figure 5.9: Sketch of the effects of misalignment of the emitter with respect to the translation stage, and of the translation stage with respect to the z-axis. Misalignment along y only is shown but there can be an equivalent misalignment along x.

Once this adjustment to the position of the emitting head has been completed, the scan is repeated. This time the centre of the beam remains fixed (figure 5.10) but the misalignment of the translation stages results in non-zero angles α and β.
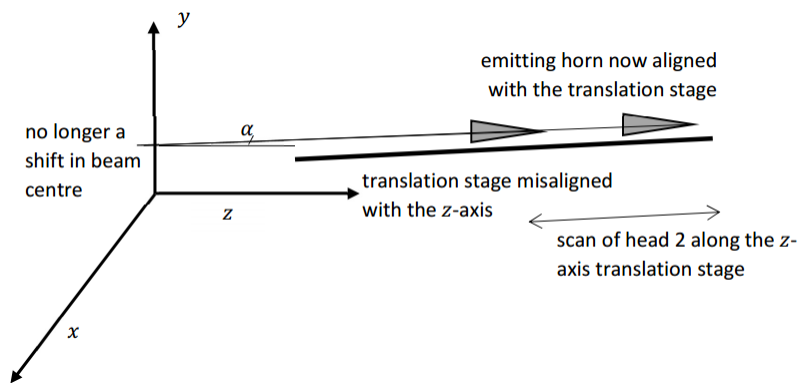

Figure 5.10: Sketch of the effects of misalignment of the translation stage with respect to the z-axis once the misalignment of the emitting head has been fixed. (There is an equivalent angle β in the x-direction.)

Geometry can again be used to correct the orientation of the translation stage for the angles α and β. The α offset is typically small (usually requiring a shift of

$1 - 3$ mm along the yz plane) and is related to the levelling of the optical bench. This is the most difficult to correct in our current set up and we use metal plates slipped under one end of the stage to adjust its tilt. One measurement is sufficient to determine the offset angles but in practice we re-measure to verify the adjustments and repeat if required.

5.3.3   Alignment of the DUT

The VNA is often used to measure the optical properties of components or devices on a propagating beam. In these cases, once the heads are aligned the DUT can be placed between them for measurements to be taken. Once again, the initial placement of a DUT generally turns out to be imperfect and it is not orthogonal to the propagation axis of the source beam. The correcting of this is a simpler process than that described previously for the two heads that are assumed now to be correctly aligned.

An aperture plate (metal plate with a small circular hole, 10 mm in diameter) had been made for each component holder to be used. The holder and aperture plate were mounted on a rotating stage between the transmitting and receiving heads. Once the aperture is centred, there are two misalignment issues to be resolved: firstly the plate mounted on the rotational stage may have a non-zero azimuth angle causing it to be not orthogonal to the beam propagation axis, and secondly the plate may be tilted forwards or backwards (similar to the α misalignment of the heads). We had less control over the tip-tilt alignment compared with the azimuthal alignment that was controlled by the rotating stage.

Centering of the component holder was carried out by measuring the aperture diffraction pattern produced on the xy scan plane. The aperture is relatively small compared to the beam and, if centred, should produce a symmetric pattern. Alignment of the rotation stage (azimuthal angle) was carried out by looking at the horn beam pattern reflected by the metal plate and back on to the scan plane (S_{22}).

Again, if the alignment is correct, the pattern should be symmetric. The phase turned out to be the most useful diagnostic. Figure 5.11 Shows the phase pattern after an initial scan when there is clearly some misalignment. Since the rotation stage affected the phase of the pattern along the x-scan direction, a cut of the phase pattern along this direction was recorded for a range of different rotation stage angles (set by the GHOST software mentioned in Section 5.1.3). Figure 5.11 shows two such phase cuts showing that an approximately flat phase was found for an azimuthal angle of $-0.5°$. The rotation stage was adjusted by this angle to correct for the azimuthal misalignment.

The tip-tilt angle of the plate (figure 5.13) was more difficult to adjust in increments (it could not be adjusted by the control software) and so in order to find the correct adjustment the azimuthal angle was again varied until the phase error along x exactly matched the phase error along y (i.e. the phase pattern was tilted at $45°$). The error that had to be introduced into the azimuthal angle to make this happen must then be equal to the tip-tilt error. The tip-tilt error determined in this way could then be corrected to complete the alignment of the component holder.
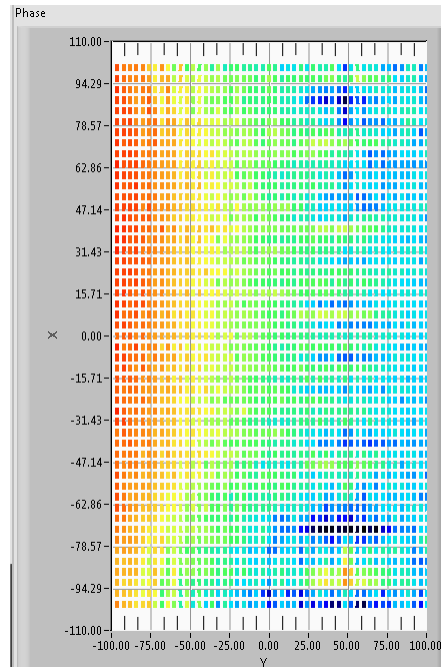
Figure 5.11: Example of the phase of the horn beam pattern reflected from a plate on a mis-aligned rotation stage.

In the future the aim is to automate the process i.e. to calculate and correct for the initial misalignments directly from one scan in the xy plane. For this work, however, we wanted to test the procedure by carrying it out manually and by then making measurements of real components, described next.
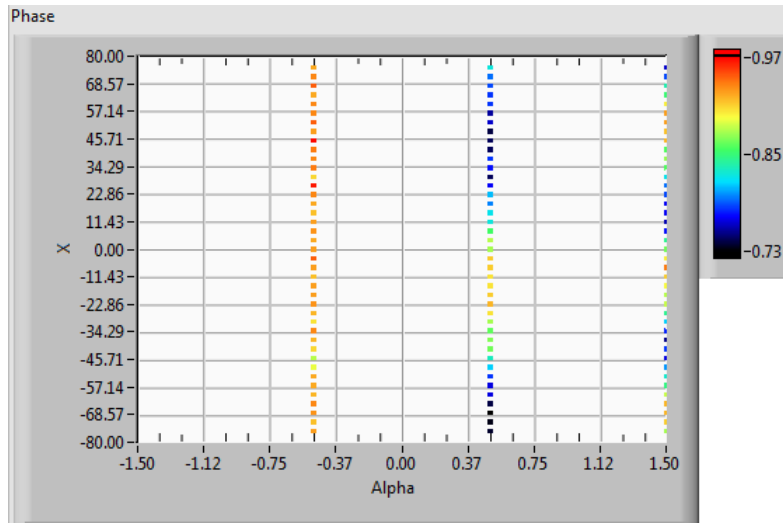
Figure 5.12: Phase along the x-dimension the scan plane as a function of rotation stage azimuth angle. The phase can be seen to be at its flattest at an angle of $-0.5°$.
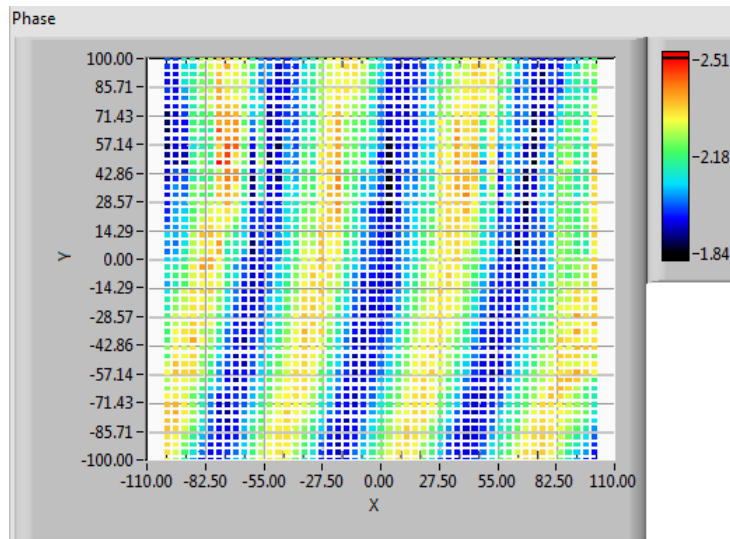

Figure 5.13: A slope in the phase pattern of the horn beam due to misalignment in the azimuthal and tip-tilt directions.

5.4   SwissTo12 Probe Measurements

New waveguide probes for the VNA had been designed and modelled in CST by Marcin Gradziel. A circular probe was designed as an improvement to the existing

WR10 rectangular probe used in the laboratory and included a wide aperture, a chamfered edge and a two-step transition from the feeding waveguide. The improved design resulted in a lower return loss and higher beam coupling when compared with a bare WR10 probe. An equivalent rectangular probe was designed to be used as a comparator. The designs were manufactured in gold-plated dielectric by the Swiss company SwissTo12 [SWISSto12, 2018]. Figure 5.14 shows a CST plot of the model for the new probes. The predicted performance of the probes is shown in Figure 5.15. For comparison, the same performance predictions for a bare WR10 waveguide probe are shown in Figure 5.16. The dielectric rectangular horn performs marginally less well than the WR10 (higher reflection, read from the scale on the left, and lower coupling to a plane wave, read from the scale on the right) but the new circular horn is an improvement. The aim of the measurements described in this section was to measure and compare the performance of these new probes.
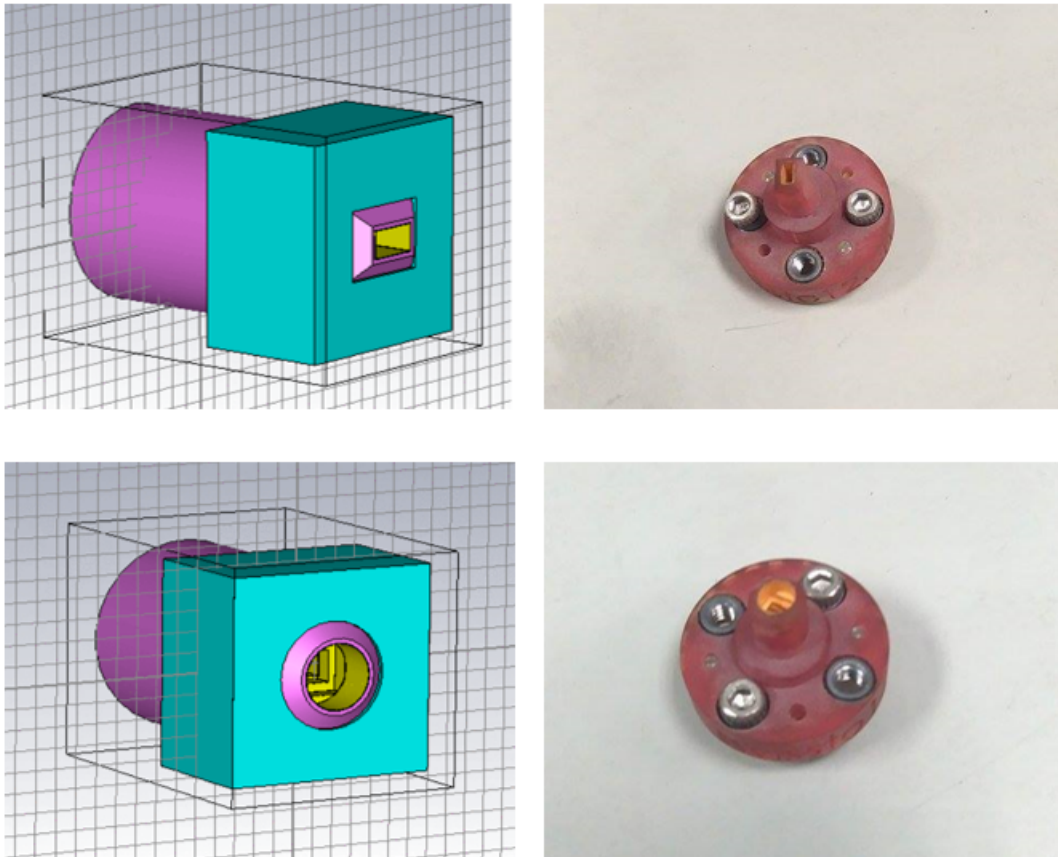
Figure 5.14: CST model (left) and photograph (right) of the two new probes: the rectangular probe (top) and the stepped circular probe (bottom).
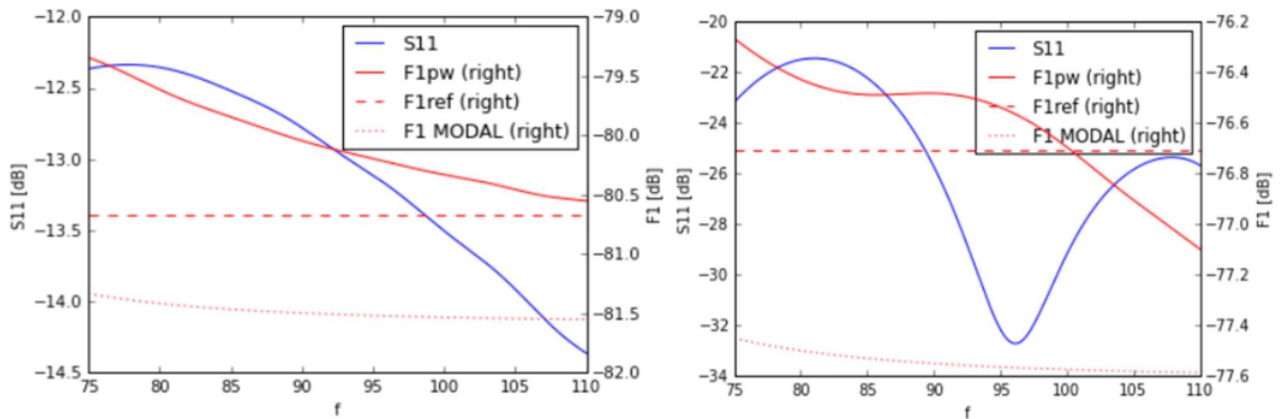
Figure 5.15: Predicted performance of the new SwissTo12 probes (in terms of reflected power S_{11} and power coupled from a plane wave F_1) as a function of frequency in GHz. The plot for the rectangular probe is on the left, and the circular probe is on the right (from M. Gradziel, Maynooth University.) The solid blue line shows the reflected power and the solid red line shows the power coupled to the probe from a plane wave. The red dashed line, for reference, shows the power falling on an area the size of the probe aperture. (The dotted line relates to coupling to a single mode rather than a plane wave.)
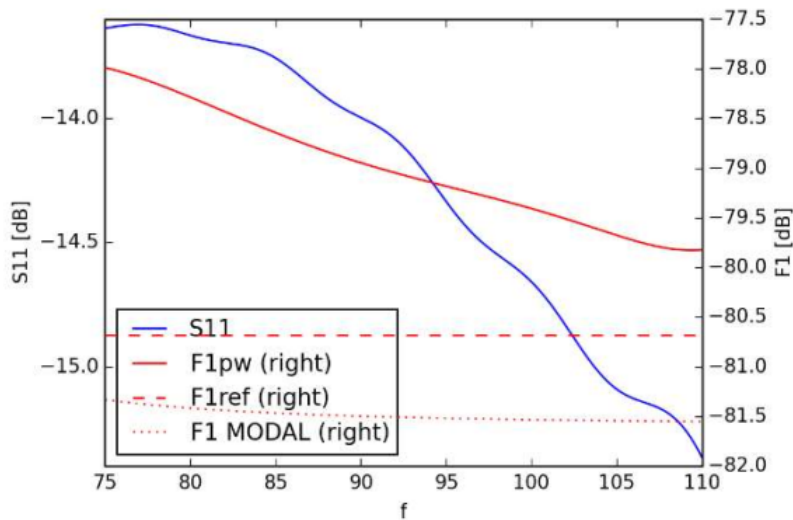

Figure 5.16: Performance of the standard WR10 rectangular probe. The individual traces are as in figure 5.15

5.4.1 Probe S_{11} measurements

The VNA was calibrated and aligned as just described. One of the new probes was placed on head 1 (figure 5.17) and a standard smooth-walled cylindrical horn was used on head 2. The beam from the smooth-walled horn could be accurately modelled. The total reflected power (S_{11}) was measured as the distance between the heads along the z-axis was increased. The result is shown in figures 5.18 and 5.19.
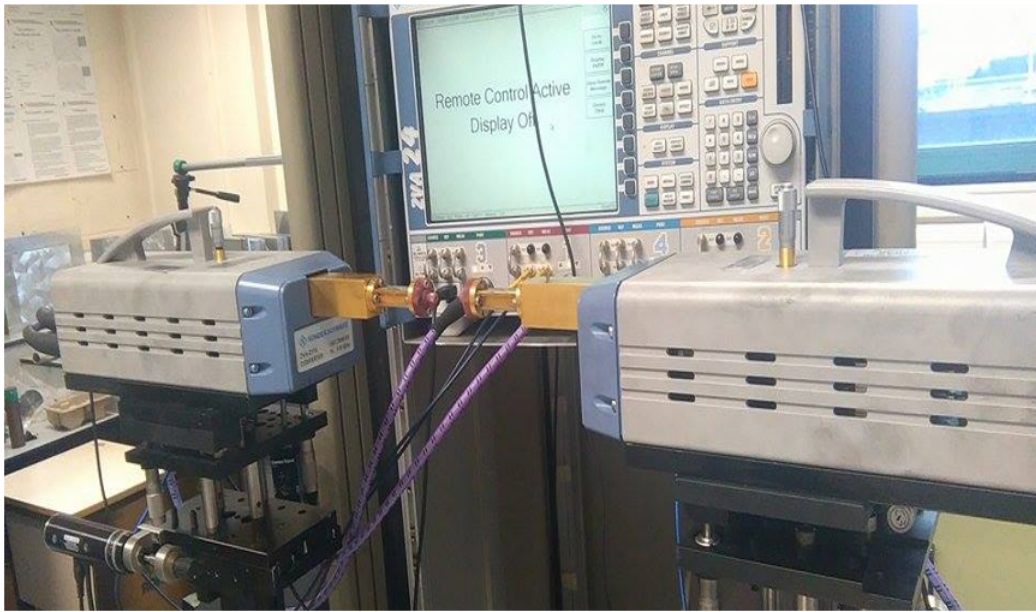

Figure 5.17: The VNA measurement of a new probe. For the measurements described here, a smooth-walled horn was used on head 2.
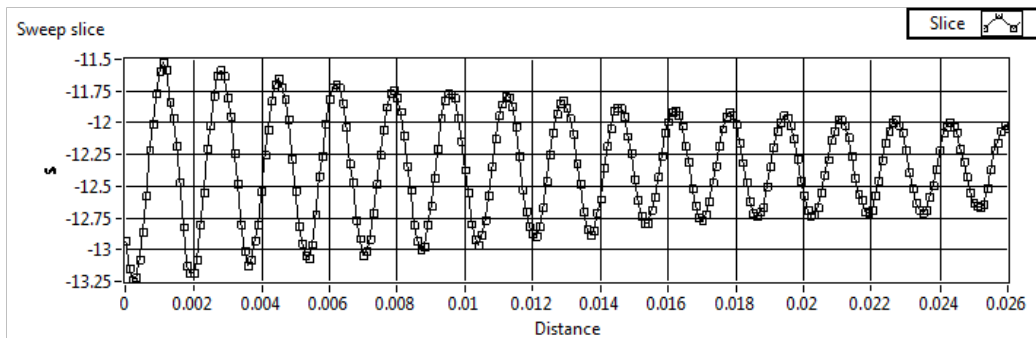

Figure 5.18: S_{11} measured at 95 GHz using the new rectangular probe.
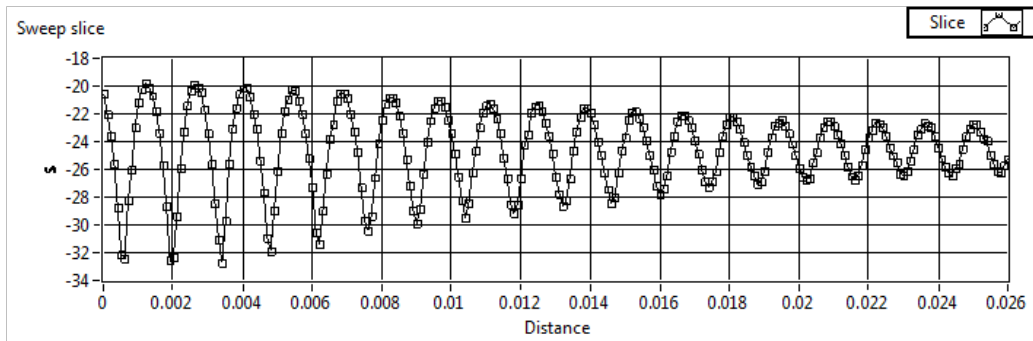
Figure 5.19: S_{11} measured at 95 GHz using the new circular probe.

The effect of standing waves on the measurements, especially at short distances is clear. The approximate averages: -12.2 dB (rectangular probe) and -23 dB (circular probe), are also at the level expected from simulations although not exactly as predicted at 95 GHz. Subsequent to these measurements, three nominally identical circular probes were measured at a range of frequencies. Figure 5.20 shows the variation that we can therefore expect from manufacturing tolerances. These measurements show that the results in figures 5.15 and 5.19 above are in the expected range. The blue trace corresponds to the horn measured in Figures 5.15 and 5.19.
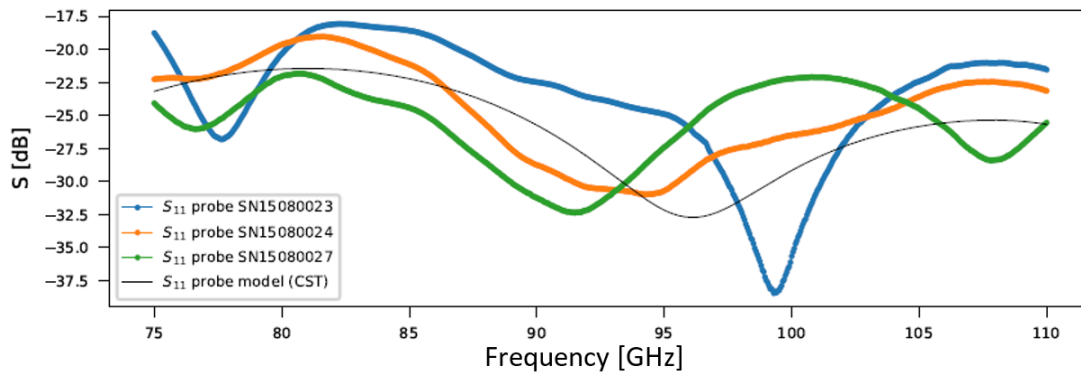

Figure 5.20: Predicted reflection from a stepped circular waveguide probe. The black line corresponds to the prediction (S_{11}, blue line) in Figure 5.15 (right) and the blue line is the horn measured in Figure 5.19.

5.4.2   Lens S_{22} measurements

Lens measurements were also undertaken as part of a project with Cardiff University that aimed to investigate coupling to large focal planes. The lens used was a large-diameter (260 mm) HDPE lens, coated in PTFE to reduce reflection, and its performance on-axis and at an angle of incidence of 10° was to be tested. The VNA was calibrated and aligned as described earlier and a lens holder was set up between a smooth-walled cylindrical horn on head 2 and a WR10 waveguide probe on head 1. The position of the lens, determined using a Gaussian beam mode analysis, was such as to produce a flat phase front at the probe. The scanner was set to take cuts of amplitude and phase (S_{12}) along the x and y axes. The lens was then rotated to +10° and the measurements repeated. The amplitude and phase cuts at 95 GHz are shown in figures 5.21 to 5.24. The measurements show that the lenses behaved well both on-axis and at 10°. We can estimate the residual misalignment in the system from the slope of the phase measured. A phase slope between ±45° in figure 5.22, for example, corresponds to about a quarter of a wavelength or 0.75 mm. This is reasonable considering the manual adjustments made to the set-up and with time could be further reduced for specific measurements. Future work will involve automation and automatic correction of misalignments.

Figure 5.21: E-cut power in the scan plane after transmission through a HDPE lens. The lens was first placed perpendicular to the beam propagation axis and rotated by 10°. A WR10 waveguide probe was used in making the measurements.
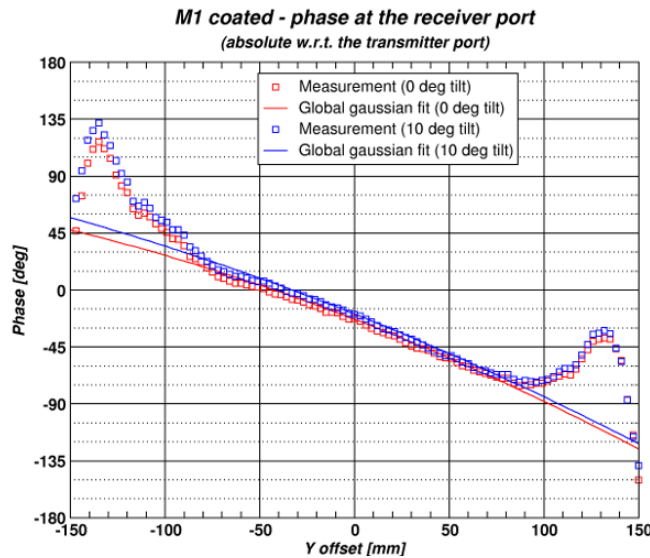
Figure 5.22: E-cut phase in the scan plane after transmission through a HDPE lens. The lens was first placed perpendicular to the beam propagation axis and rotated by 10°. A WR10 waveguide probe was used in making the measurements.

Figure 5.23: H-cut power in the scan plane after transmission through a HDPE lens. The lens was first placed perpendicular to the beam propagation axis and rotated by 10°. A WR10 waveguide probe was used in making the measurements.
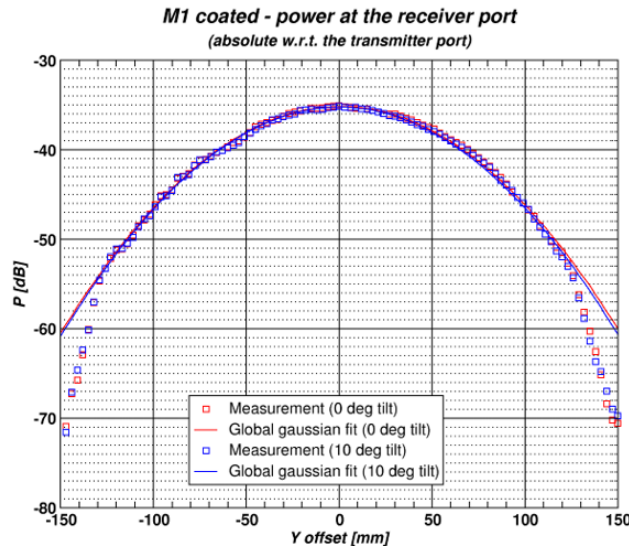

Figure 5.24: H-cut power in the scan plane after transmission through a HDPE lens. The lens was first placed perpendicular to the beam propagation axis and rotated by 10°. A WR10 waveguide probe was used in making the measurements.
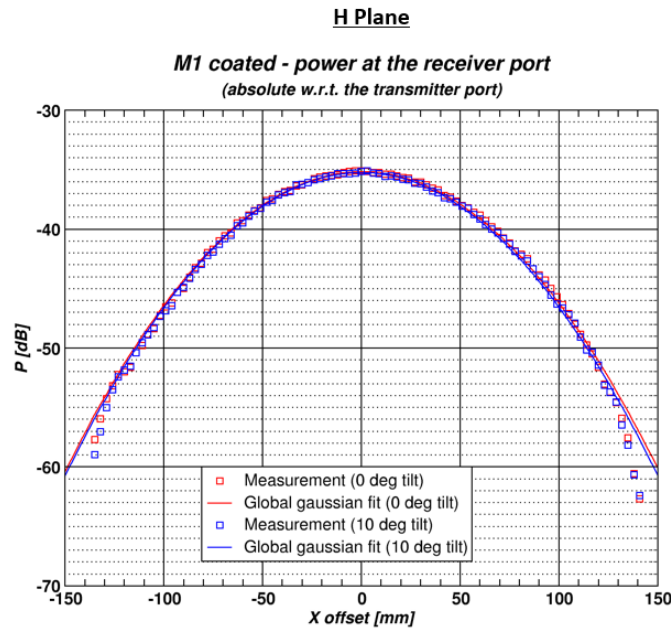
156

The measurements were repeated but using the new stepped circular waveguide probe instead of the WR10 waveguide. The results are shown in figures 5.25 to 5.28.

Figure 5.25: E-cut power in the scan plane after transmission through a HDPE lens. The lens was first placed perpendicular to the beam propagation axis and rotated by 10°. The new circular probe was used in making the measurements.
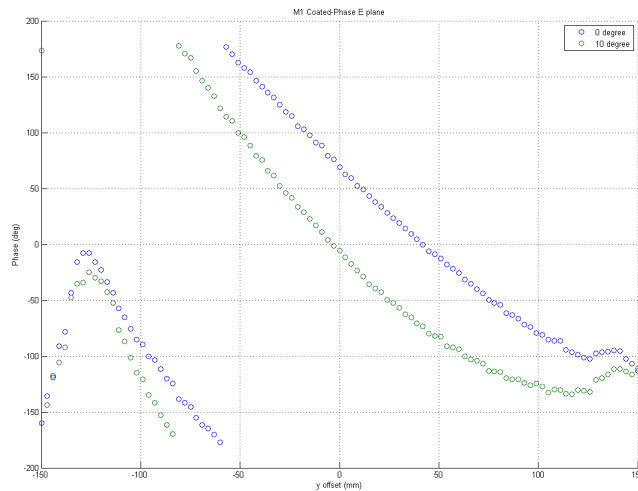
Figure 5.26: E-cut power in the scan plane after transmission through a HDPE lens. The lens was first placed perpendicular to the beam propagation axis and rotated by 10°. The new circular probe was used in making the measurements.

Figure 5.27: H-cut power in the scan plane after transmission through a HDPE lens. The lens was first placed perpendicular to the beam propagation axis and rotated by 10°. The new circular probe was used in making the measurements.
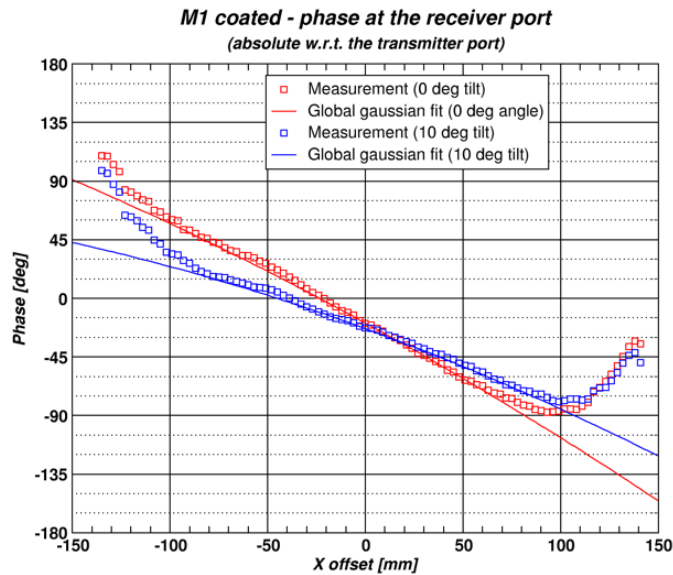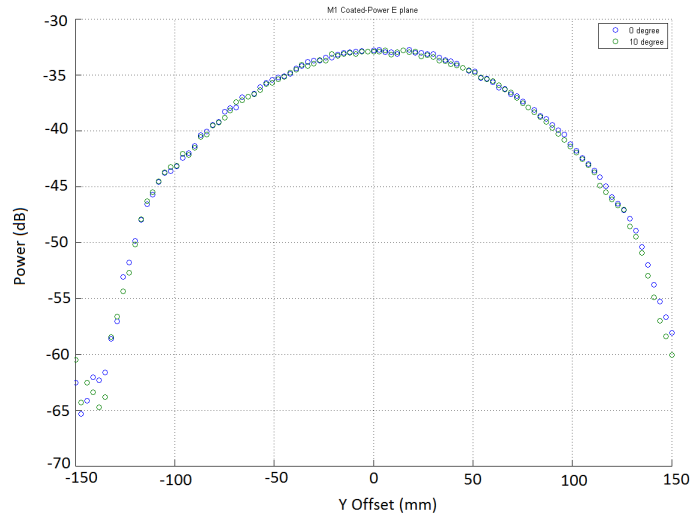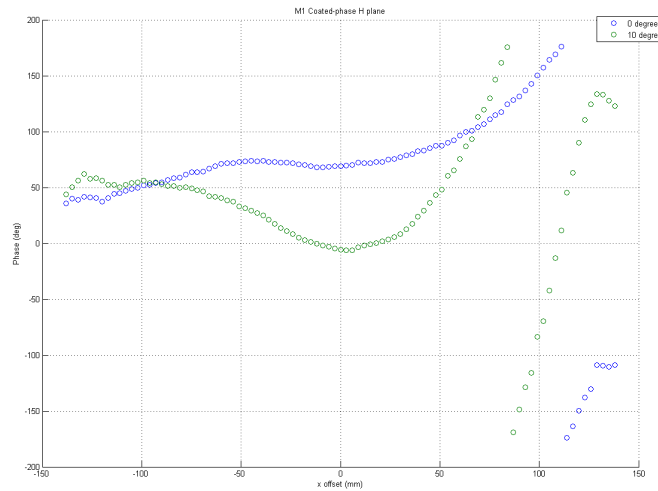

Figure 5.28: H-cut power in the scan plane after transmission through a HDPE lens. The lens was first placed perpendicular to the beam propagation axis and rotated by 10°. The new circular probe was used in making the measurements.
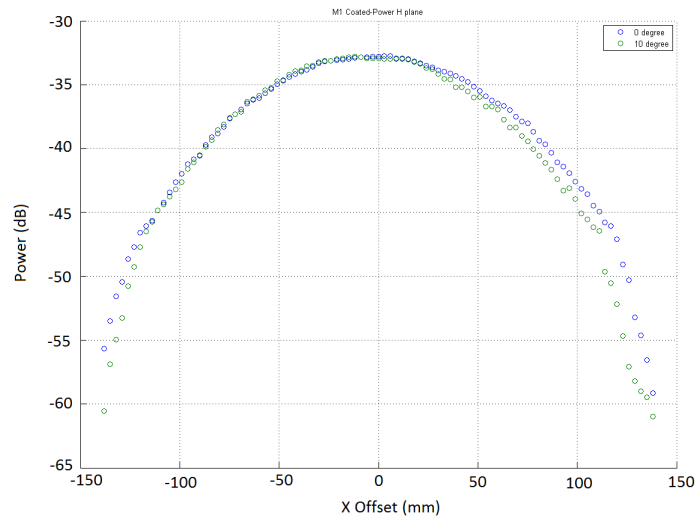
The peak amplitude measured using the WR10 probe was -35 dB and this increased to -32.7 dB when using the new circular probe. This 2.3 dB is close to the

improvement expected from the CST simulations of F1 power in Figure 5.15 (right) and Figure 5.16 (77.1 dB - (79.8 dB) = 2.7 dB).

5.5   Summary and Conclusion

The main aim of the work in this chapter was to give the author some experience at making laboratory measurements of quasi-optical components. These types of measurements are crucial for verifying manufacturing and the modelling results described in earlier chapters. The measurements were made with a VNA at Maynooth University.

The VNA was first calibrated using the standard TOSM technique and then a manual alignment procedure was tested for both the VNA heads and a DUT. The procedure was found to work sufficiently well for work to start on automating it. The alignment was tested using measurements of lenses and using newly designed waveguide probes for which theoretical simulations were available.

Chapter 6

Conclusions

In this thesis, my studies focussed on aspects of quasi-optical analysis of millimetre and submillimetre astronomical telescope systems, primarily that of the 3 and 4 mm channels of the Onsala 20 m telescope. The specific techniques used for this study were Gaussian beam mode analysis (GBMA) and physical optics (PO) as implemented in the GRASP package. The final part of this thesis looked at using the Experimental Physics Department's Vector Network Analyser (VNA) and using it to take measurements of quasi-optical components.

A broad overview of the history of astronomy in the millimetre and submillimetre region of the electromagnetic spectrum is given in Chapter 1. The chapter outlines a number of characteristics of this area of the electromagnetic spectrum as well as a number of current and possible applications associated with it.

In Chapter 2 I discuss the theory behind the two analysis methods used: GBMA and PO. The advantages and disadvantages of both these methods are discussed along with a more in-depth description of their functionality. An introduction to Gaussian beam propagation as well as ray matrix analysis is given. This is done in quite a bit of detail as I wrote my own code for this type of analysis. A Gaussian beam telescope is used for illustration. Finally, the functionality of the software package GRASP is described. I used GRASP for PO analysis of the telescope

systems in the later chapters. GRASP is commercially available and is considered the industry standard for this type of work. GBMA is quick and relatively accurate and can be used in the initial design and optimisation of an optical system. PO is used for the accurate characterisation of a final system and includes the effect of diffraction, truncation and off-axis aberrations.

Chapter 3 begins with a brief introduction to the Onsala Space Observatory, with particular attention given to the 3 and 4 mm channels of the 20 m telescope. An initial analysis of the 4 mm system was carried out, which was then applied to a proposed re-design of the 3 mm channel, the purpose of which was to allow for simultaneous viewing of the K band (18 - 27 GHz) and W band (85 - 116 GHz). To allow this, the receiver was required to be pushed back 600 mm. The proposed solution to this problem was the use of a Gaussian beam telescope. This proposition was first analysed using GBMA, which gave promising results in terms of beam shape and power. If optical components of sizes similar to existing components were used, then the additions proposed were found not to degrade the performance of the system. The proposed re-design was then analysed with full vector PO using GRASP, and again the performance of the new system was found the be good. Comparing the results of the two analysis techniques allowed the effects of off-axis asymmetry to be explored and I conclude that GBMA was sufficient to model the main features of the system.

Chapter 4 dealt with the concept of random and systematic errors that can affect telescopes, primarily telescope mirrors, in real life systems. Random errors were generated using Gaussian random variables, with a method devised by Kroese and Botev [Kroese and Botev, 2013] to mimic mirror imperfections with non-zero correlation lengths. These errors were added to the perfect mirror models of the 4 mm channel system in GRASP using different coherence values, $\frac{1}{100}$, $\frac{1}{500}$, $\frac{1}{1000}$ and $\frac{1}{5000}$, and these each were scaled by $\frac{\lambda}{20}$, $\frac{\lambda}{40}$ and $\frac{\lambda}{60}$. The imperfections caused distortion of the beam in both co-polarization and cross-polarization, with the greatest effect

being caused by a coherence length of $\frac{1}{100}$ and scaled by $\frac{\lambda}{20}$. When the systematic errors (a feature due to a ring support was used as an example) were applied to a mirror, the beam was quite tolerant to distortion and I required a scaling of $\frac{\lambda}{10}$ to see a noticeable effect.

In the last chapter, Chapter 5, an introduction to the department's VNA work was given as well as some of the theory required to understand its operation. The process of setting up, calibrating and aligning of the kit was described in detail. The main aim of my work was to test a proposed alignment procedure that could be automated in the future. After alignment, the VNA was used to measure the performance of a lens using newly designed waveguide probes. The results showed that the alignment was sufficient to test the lenses and the increase in power measured by a new probe was consistent with predictions.

This work has given me a useful introduction into design, analysis and measurements of quasi-optical astronomical telescopes.

Appendix A

GRASP Tor file

This is the GRASP .tor file that describes the proposed OSO 3 mm redesign shown in figure 3.24. The details may be useful if such a proposal is adopted in the future.

Global coor_sys ( )

Intercept coor_sys

(origin : struct(x: 0.0 mm, y: 0.0 mm, z: 220.0 mm))

frequency frequency

(frequency_list : sequence(84.0 GHz))

rimM1 elliptical_rim

(half_axis : struct(x: 70.0 mm, y: 70.0 mm))

Eliptic1 polynomial_2nd_order

(coefficients : struct(xx: 0.510923E-02, xy: 0.0, yy: 0.510923E-02, x: 0.0, y: 0.0, c: 0.0, zz: -0.338698E-02, z: -1.0, xz: 0.0, yz: 0.0, unit: mm), origin : struct(x: -18.1193 mm, y: 0.0 mm, z: -279.2043 mm), rotations : sequence (struct(around: y_original, angle: 197.0166)))

Mirror1 reflector

(coor_sys : ref(Intercept), surfaces : sequence(ref(Eliptic1)), rim : ref(rimM1))

interceptM2 coor_sys

(origin : struct(x: 0.0 mm, y: 0.0 mm, z: 327.3062 mm), base : ref(GlobalM2)
)

GlobalM2 coor_sys

(origin : struct(x: 120.0 mm, y: 0.0 m, z: 412.7123 mm), x_axis : struct(x: -1.0,
y: 0.0, z: -0.1224646799E-15))

rimM2 elliptical_rim

(half_axis : struct(x: 80.323 mm, y: 80.323 mm))

Eliptic2 polynomial_2nd_order

(coefficients : struct(xx: 0.361004E-02, xy: 0.0, yy: 0.361004E-02, x: 0.0, y:
0.0, c: 0.0, zz: -0.23145E-02, z: -1.0, xz: 0.0, yz: 0.0, unit: mm), origin : struct(x:
-23.4071 mm, y: 0.0 mm, z: -410.6986 mm), rotations : sequence (struct(around:
y_original, angle: 195.6787)))

Mirror2 reflector

(coor_sys : ref(interceptM2), surfaces : sequence(ref(Eliptic2)), rim : ref(rimM2)
)

POM1 po_single_face_scatterer

(frequency : ref(frequency), scatterer : ref(Mirror1), po_points : struct(po1:
401, po2: 401), spill_over : on)

POM2 po_single_face_scatterer

(frequency : ref(frequency), scatterer : ref(Mirror2), po_points : struct(po1:
401, po2: 401), spill_over : on)

aperture coor_sys

(origin : struct(x: 0.0 mm, y: 0.0 mm, z: 100.0 mm))

idealhorn hybrid_mode_conical_horn

(frequency : ref(frequency), coor_sys : ref(aperture), waveguide_radius : 1.890684177
mm, aperture_radius : 15.0 mm, semi_flare_angle : 8.626926559)

CW_01_coor_sys coor_sys

(origin : struct(x: 0.0 m, y: 0.0 m, z: -243.3 mm), x_axis : struct(x: -1.0, y: 0.0, z: 0.0), base : ref(interceptM2))

TFM_02_coor_sys coor_sys

(origin : struct(x: 0.0 m, y: 0.0 m, z: 35.8 mm), x_axis : struct(x: 0.707106781186548, y: 0.0, z: -0.707106781186548), base : ref(CW_01_coor_sys))

TFM_02_surface plane

( )

POTM02 po_single_face_scatterer

(frequency : ref(frequency), scatterer : ref(TM_02), po_points : struct(po1: 401, po2: 401), spill_over : on)

gridAtSub planar_grid

(coor_sys : ref(sub_coor_sys), x_range : struct(start: -2000.0, end: 2000.0, np: 401, unit: mm), y_range : struct(start: -2000.0, end: 2000.0, np: 401), frequency : ref(frequency))

POTM01 po_single_face_scatterer

(frequency : ref(frequency), scatterer : ref(TM_01), po_points : struct(po1: 401, po2: 401), spill_over : on)

POTFM02 po_single_face_scatterer

(frequency : ref(frequency), scatterer : ref(TFM02), po_points : struct(po1: 401, po2: 401), spill_over : on)

POTFM01 po_single_face_scatterer

(frequency : ref(frequency), scatterer : ref(TFM_01), po_points : struct(po1: 401, po2: 401), spill_over : on)

CW_03_coor_sys coor_sys

(origin : struct(x: 0.0 mm, y: 0.0 mm, z: -200.1 mm), base : ref(interceptM2))

CW_02_coor_sys coor_sys

(origin : struct(x: 0.0 mm, y: 0.0 mm, z: -209.1 mm), base : ref(interceptM2))

FM_02_rim_aperture elliptical_rim

(half_axis : struct(x: 55.0 mm, y: 55.0 mm))

FM_02_coor_sys coor_sys

(origin : struct(x: 0.0 mm, y: 0.0 mm, z: -914.9 mm), base : ref(interceptM2))

FM_01_coor_sys coor_sys

(origin : struct(x: 0.0 mm, y: 0.0 mm, z: -1061.4 mm), base : ref(interceptM2)

)

FM_01_rim_aperture elliptical_rim

(half_axis : struct(x: 55.0 mm, y: 55.0 mm))

CW_03_rim_aperture elliptical_rim

(half_axis : struct(x: 47.5 mm, y: 47.5 mm))

CW_03_aperture aperture_in_screen

(coor_sys : ref(CW_03_coor_sys), rim : ref(CW_03_rim_aperture))

CW_02_rim_aperture elliptical_rim

(half_axis : struct(x: 46.0 mm, y: 46.0 mm))

CW_01_rim_aperture elliptical_rim

(half_axis : struct(x: 45.5 mm, y: 45.5 mm))

CW_02_aperture aperture_in_screen

(coor_sys : ref(CW_02_coor_sys), rim : ref(CW_02_rim_aperture))

CW_01_aperture aperture_in_screen

(coor_sys : ref(CW_01_coor_sys), rim : ref(CW_01_rim_aperture))

FM_02 aperture_in_screen

(coor_sys : ref(FM_02_coor_sys), rim : ref(FM_02_rim_aperture))

FM_01 aperture_in_screen

(coor_sys : ref(FM_01_coor_sys), rim : ref(FM_01_rim_aperture))

sub_coor_sys coor_sys

(origin : struct(x: 0.0 mm, y: 0.0 mm, z: -9351.9 mm), base : ref(interceptM2)

)

sub_planar_cut planar_cut

(coor_sys : ref(sub_coor_sys), rho_range : struct(start: -2000.0, end: 2000.0, np: 400, rho_unit: mm), phi_range : struct(start: 0.0, end: 0.0, np: 1), file_name : sub_planar_cut.cut, comment : "Field data in cuts")

POCW03 po_aperture_in_screen

(frequency : ref(frequency), scatterer : ref(CW_03_aperture), po_points : struct(po1: 401, po2: 401))

POCW02 po_aperture_in_screen

(frequency : ref(frequency), scatterer : ref(CW_02_aperture), po_points : struct(po1: 401, po2: 401))

POCW01 po_aperture_in_screen

(frequency : ref(frequency), scatterer : ref(CW_01_aperture), po_points : struct(po1: 401, po2: 401))

POFM01 po_aperture_in_screen

(frequency : ref(frequency), scatterer : ref(FM_01), po_points : struct(po1: 401, po2: 401))

POFM02 po_aperture_in_screen

(frequency : ref(frequency), scatterer : ref(FM_02), po_points : struct(po1: 401, po2: 401))

gaussian_beam gaussian_beam

(frequency : ref(frequency), coor_sys : ref(aperture), beam_radius : 9.6525 mm, phase_front_radius : 100.0 mm)

sub_planar_cut_orthog planar_cut

(coor_sys : ref(sub_coor_sys), rho_range : struct(start: -2000.0, end: 2000.0, np: 400, rho_unit: mm), phi_range : struct(start: 90.0, end: 90.0, np: 1), comment : "Field data in cuts")

TFM_02_rim elliptical_rim

(half_axis : struct(x: 32.4 mm, y: 32.4 mm))

TFM02 reflector

(coor_sys : ref(TFM_02_coor_sys), surfaces : sequence(ref(TFM_02_surface)), rim : ref(TFM_02_rim))

TM_02_surface ellipsoid

(vertex_distance : 3112.044 mm, foci_distance : 2795.998 mm, axis_angle : 263.09067)

TM_02_coor_sys coor_sys_grasp_angles

(origin : struct(x: 36.354 mm, y: 0.0 mm, z: 35.8 mm), theta : 90.0, psi : 180.0, base : ref(CW_01_coor_sys))

TM_02_rim elliptical_rim

(half_axis : struct(x: 67.0 mm, y: 67.0 mm))

TM_02 reflector

(coor_sys : ref(TM_02_coor_sys), surfaces : sequence(ref(TM_02_surface)), rim : ref(TM_02_rim))

TM_01 reflector

(coor_sys : ref(TM_01_coor_sys), surfaces : sequence(ref(TM_01_surface)), rim : ref(TM_01_rim))

TM_01_coor_sys coor_sys_grasp_angles

(origin : struct(x: 93.101 mm, y: 0.0 mm, z: 635.8 mm), theta : 90.0, psi : 180.0, base : ref(CW_01_coor_sys))

TM_01_rim elliptical_rim

(half_axis : struct(x: 82.0 mm, y: 82.0 mm))

TM_01_surface ellipsoid

(vertex_distance : 1659.791 mm, foci_distance : 1326.285 mm, axis_angle : 107.241)

TFM_01_surface plane

( )

TFM_01_rim elliptical_rim

(half_axis : struct(x: 32.4 mm, y: 32.4 mm))

TFM_01_coor_sys coor_sys

(origin : struct(x: 0.0 mm, y: 0.0 mm, z: 635.8 mm), x_axis : struct(x: 0.707106781186548, y: 0.0, z: 0.707106781186548), base : ref(CW_01_coor_sys))

TFM_01 reflector

(coor_sys : ref(TFM_01_coor_sys), surfaces : sequence(ref(TFM_01_surface)), rim : ref(TFM_01_rim))

//DO NOT MODIFY OBJECTS BELOW THIS LINE. //THESE OBJECTS ARE CREATED AND MANAGED BY THE //GRAPHICAL USER INTERFACE AND SHOULD NOT BE //MODIFIED MANUALLY! view_1 view

(objects : sequence(ref(view_1_coor_sys_plot),ref(view_1_reflector_plot),ref(view_1_feed_plot), ref(view_1_output_points_plot),ref(view_1_tabulated_planar_source_plot),ref(rays_from_point_sources), ref(view_1_plate_plot),ref(view_1_aperture_in_screen_plot)), show_hide : struct(reflectors: show, coordinate_systems: hide, feeds: show, output_points: show, struts: show, tabulated_meshes: show, boxes: show, plates: show, wires: show, mom_meshes: hide, apertures_in_screen: show, lenses: show, tabulated_planar_sources: show, plane_waves: show, dgr_intercostals: show, cad_files: show, rooftop_mirrors: show, loads: show, bors: show, mom_sources: show, reflectarray: show))

view_1_coor_sys_plot coor_sys_plot

( )

view_1_reflector_plot reflector_plot

( )

view_1_feed_plot feed_plot

( )

view_1_output_points_plot output_points_plot

( )

view_1_tabulated_planar_source_plot tabulated_planar_source_plot

( )

rays_from_point_sources rays_from_point_sources

(objects : sequence(ref(idealhorn)), theta_range : struct(start: -5.0, end: 5.0, np: 3), ray_path_range : struct(start: 0.0 mm, end: 10000.0 mm))

view_1_plate_plot plate_plot

( )

view_1_aperture_in_screen_plot aperture_in_screen_plot

( )

//$$ Saved at 17:49:31 on 23.10.2018 by GRASP ver. 10.5.0 SN=006233

Appendix B

GRASP Tci file

This GRASP .tci file was used to generate the results shown in figure 3.26 and 3.27.

COMMAND OBJECT POM1 get_currents (source : sequence(ref(idealhorn)),
& auto_convergence_of_po : on, convergence_on_scatterer : sequence(ref(Mirror2)))
& cmd_1 COMMAND OBJECT POM2 get_currents (source : sequence(ref(POM1)),
& auto_convergence_of_po : on, convergence_on_scatterer : & sequence(ref(CW_03_aperture)))
cmd_2 COMMAND OBJECT POCW03 get_currents (source : sequence(ref(POM2)),
& auto_convergence_of_po : on, convergence_on_scatterer : & sequence(ref(CW_02_aperture)))
cmd_4 COMMAND OBJECT POCW02 get_currents (source : sequence(ref(POCW03)),
& auto_convergence_of_po : on, convergence_on_scatterer : & sequence(ref(CW_01_aperture)))
cmd_5 COMMAND OBJECT POCW01 get_currents (source : sequence(ref(POCW02)),
& auto_convergence_of_po : on, convergence_on_scatterer : sequence(ref(TFM02)))
& cmd_6 COMMAND OBJECT POTFM02 get_currents (source : sequence(ref(POCW01)),
& auto_convergence_of_po : on, convergence_on_scatterer : sequence(ref(TM_02))) &
cmd_7 COMMAND OBJECT POTM02 get_currents (source : sequence(ref(POTFM02)),
& auto_convergence_of_po : on, convergence_on_scatterer : sequence(ref(TM_01))) &
cmd_10 COMMAND OBJECT POTM01 get_currents (source : sequence(ref(POTM02)),

& auto_convergence_of_po : on, convergence_on_scatterer : sequence(ref(TFM_01)))

& cmd_11 COMMAND OBJECT POTFM01 get_currents (source : sequence(ref(POTM01)),

& auto_convergence_of_po : on, convergence_on_scatterer : sequence(ref(FM_02))) &

cmd_12 COMMAND OBJECT POFM02 get_currents (source : sequence(ref(POTFM01)),

& auto_convergence_of_po : on, convergence_on_scatterer : sequence(ref(FM_01))) &

cmd_13 COMMAND OBJECT POFM01 get_currents (source : sequence(ref(POFM02)),

& auto_convergence_of_po : on, convergence_on_output_grid : & sequence(ref(sub_planar_cut)))

cmd_8 COMMAND OBJECT sub_planar_cut_orthog get_field (source : & sequence(ref(POFM01)))

cmd_9 QUIT

Appendix C

Code for Generating .sfc Files

This code generates GRASP .sfc surfaces file of the mirror CM_02 of the OSO 4 mm channel.

```
import numpy as np
import cmath
import matplotlib.pyplot as plt
from mpl_toolkits import mplot3d
from matplotlib import cm
import random
import pandas as pd
xmin = -100
xmax = 100
ymin = -100
ymax = ymin * -1
steps = 51
data =np.loadtxt(f,delimiter='/n')
#Output file f = open("rotated_ellipse_M2.sfc","w")
x = np.linspace(xmin,xmax,steps)#define x range
```

```python
y = np.linspace(ymin,ymax,steps)#define y range
## generate list place holders
xr = []
yr = []
zpr = []
znr = []
for xn in x:
    for yn in y:
        calc = (1.2273e-16)*((-5.24695e17) + (1.98421e15)*xn + (1.13564e-23)*
        np.sqrt(1.38322e82 - (1.05156e80)*xn - (4.0931e77)*(xn*xn) - (6.08141e77)*(yn*yn)))
        ellipsoid = calc + a
        #calculate quadratics
        if ellipsoid >= 0:
        xr.append(xn)
        yr.append(yn)
        zpr.append(ellipsoid)
        xr = np.asarray(xr)
        yr = np.asarray(yr)
        znr = np.asarray(znr)
        zpr = np.asarray(zpr)
xmin = min(xr)
xmax = max(xr)
ymin = min(yr)
ymax = max(yr)
numx = len(xr)
numy = len(yr)
numberofpoints = numx
fileloop = pow(steps,2)
```

f.write("list of coordinates for irregular grid in GRASP \n")

f.write("

for i in range (0,numx): f.write("%f" %xr[i]+" ""%f" %yr[i]+" ""%f" %zpr[i])
f.write("\n")

for i in range (0,numx): f.write("%f" %xr[i]+" ""%f" %yr[i]+" ""%f" %znr[i])
f.write("\n")

f.write("%d" %xmin +", " "%d" %ymin +", " "%d" %xmax +", " "%d" %ymax
+ "\n");

f.write("%d" %numx +", " "%d" %numy + "\n")

f.close()

surf = ax.plot_trisurf(xr, yr, zpr)

plt.show()

For mirrors CM_01 the lines for calc. were replaced by calc = 1.66344e-15*(-
3.86454e16 + 1.46403e14*xn + 3.78199e-24*np.sqrt(6.80029e80 - 5.15245e78*(xn)
- 2.009e76*(xn*xn) - 2.98497e76*(yn*yn)))

Appendix D

Surface Error Generation Code

This Matlab code was used to generate a 128 × 128 grid of random Gaussian numbers with rms 1 and covariance 100.

```
n = 128;
t1 = [0:1/n:1-1/n]; t2 = t1;
for i=1:n % first row of cov. matrix, arranged in a matrix. 100 in this example
        for j=1:n
        G(i,j)=exp(-100*(min(abs(t1(1)-t1(i)), ...
        1-abs(t1(1)-t1(i)))^2 + min(abs(t2(1)-t2(j)), ...
        1-abs(t2(1)-t2(j)))^2));
        end;
end;
Gamma = fft2(G); % the eigenvalue matrix n*fft2(G/n)
Z = randn(n,n) + sqrt(-1)*randn(n,n);
X = real(fft2(sqrt(Gamma).*Z/n));
imagesc(X); colormap(gray)
fileID = fopen('list_rough_surface_covar_100.txt','wt');
fmt = '%5e/n';
```

```
for j=1:n
        for i=1:n
        b = X(i,j);
        fprintf(fileID,fmt,b);
        end;
end;
fclose(fileID);


    dlmwrite('grfield3_128e.txt',b,'delimiter',',')
```

References

F. I. Akyildiz and J. M. J. C. Han. Terahertz band: Next frontier for wireless communications. *Physical Communication*, 12:16–32, September 2014.

ALMA. About ALMA, at first glance. URL `http://www.almaobservatory.org/en/about-alma-at-first-glance/`.

E. Battistelli et al. QUBIC: The QU Bolometric Interferometer for Cosmology. *Astroparticle Physics*, 34(9):705–716, 2011.

V. Belitsky, I. Lapkin, M. Fredrixon, E. Sundin, L. Helldner, L. Pettersson, S.-E. Ferm, M. Pantaleev, B. Billade, P. Bergman, A. O. H. Olofsson, M. S. Lerner, M. Strandberg, M. Whale, A. Pavolotsky, J. Flygare, H. Olofsson, and J. Conway. A new 3 mm band receiver for the Onsala 20 m antenna. *Astronomy and Astrophysics*, 580(A29):1–6, August 2015.

F. Bengal. Class 2 - ellipses, conics, 2004. URL `http://lasp.colorado.edu/~bagenal/3750/ClassNotes/Class2/Class2.html`.

S. Bernal. Rays and matrices. In *A Practical Introduction to Beam Physics and Particle Accelerators*, 2053-2571, pages 1–8. Morgan and Claypool Publishers, 2016. ISBN 978-1-6817-4076-8. doi: 10.1088/978-1-6817-4076-8ch1.

Chalmers University. Technical description (25 m telescope), 2014. URL `http:`

`//www.chalmers.se/en/researchinfrastructure/oso/radio-astronomy/`
`25m/Pages/Technical-description.aspx`.

Chalmers University. Technical description (20 m telescope), 2016. URL `http:`
`//www.chalmers.se/en/researchinfrastructure/oso/radio-astronomy/`
`20m/Pages/Description.aspx`.

A. S. Chirkin. Physical optics. *Quantum Electronics*, 29(3):281, 1999.

R. Cumming and M. Nystås. The 20-metre telescope gets a new
radome, 2014. URL `http://www.chalmers.se/en/news/Pages/`
`The-20-metre-telescope-gets-a-new-case.aspx`.

P. Dean et al. Terahertz imaging using quantum cascade lasers—a review of systems
and applications. *Journal of Physics D: Applied Physics*, 47(37), 2014.

J. Downs. *'Practical Conic Sections: The Geometric Properties of Ellipses, Parabolas and Hyperbolas'*. Dover Publications, 1993.

EAO. URL `http://www.eaobservatory.org/jcmt/public/jcmt/`.

G. A. Ediss. 'Diffraction of a Gaussian beam at an aperture'. *IEE Proceedings H: Microwaves Antennas and Propagation*, 137:171–174, June 1990.

ESA. Observations Very Long Baseline Interferometry VLBI. URL
`http://www.esa.int/Our_Activities/Space_Science/Observations_Very_`
`Long_Baseline_Interferometry_VLBI`.

ESA. Planck at a glance, 2009. URL `http://www.esa.int/Our_Activities/`
`Space_Science/Planck/Planck_at_a_glance`.

J. F. Federici, B. Schulkin, F. Huang, D. Gary, R. Barat, F. Oliveira, and D. Zimdars. THz imaging and sensing for security applications—explosives, weapons

and drugs. *Semiconductor Science and Technology*, 20(7):S266, 2005. URL http://stacks.iop.org/0268-1242/20/i=7/a=018.

U. Frisk et al. The odin satellite i. radiometer design and test. *Astronomy & Astrophysics*, 402(27-34), 2003.

P. Goldsmith. *Quasioptical Systems. Gaussian Beam Quasioptical Propagation and Applications.* IEEE Press Marketing, 1998.

Google. Google maps, 2017. URL https://www.google.ie/maps.

Harvard. The chandra mission, 2014. URL http://chandra.harvard.edu/about/axaf_mission.html.

M. Hiebel. Fundamentals of vector network analysis, 2007.

H. Hirabayashi, H. Hirosawa, H. Kobayashi, Y. Murata, P. G. Edwards, E. B. Fomalont, K. Fujisawa, T. Ichikawa, T. Kii, J. E. J. Lovell, G. A. Moellenbrock, R. Okayasu, M. Inoue, N. Kawaguchi, S. Kameno, K. M. Shibata, Y. Asaki, T. Bushimata, S. Enome, S. Horiuchi, T. Miyaji, T. Umemoto, V. Migenes, K. Wajima, J. Nakajima, M. Morimoto, J. Ellis, D. L. Meier, D. W. Murphy, R. A. Preston, J. G. Smith, S. J. Tingay, D. L. Traub, R. D. Wietfeldt, J. M. Benson, M. J. Claussen, C. Flatters, J. D. Romney, J. S. Ulvestad, L. R. D'Addario, G. I. Langston, A. H. Minter, B. R. Carlson, P. E. Dewdney, D. L. Jauncey, J. E. Reynolds, A. R. Taylor, P. M. McCulloch, W. H. Cannon, L. I. Gurvits, A. J. Mioduszewski, R. T. Schilizzi, and R. S. Booth. Overview and initial results of the very long baseline interferometry space observatory programme. *Science*, 281 (5384):1825–1829, 1998. ISSN 0036-8075. doi: 10.1126/science.281.5384.1825. URL http://science.sciencemag.org/content/281/5384/1825.

J. A. Hodgson, T. P. Krichbaum, A. P. Marscher, S. G. Jorstad, I. Marti-Vidal,

M. Bremer, M. Lindqvist, P. de Vicente, and A. Zensus. The latest results from the Global mm-VLBI Array. *arXiv e-prints*, July 2014.

IAU. IAU list of important spectral lines, 1991. URL `https://www.craf.eu/iau-list-of-important-spectral-lines/#Supplementarylist`.

P. Johansen. Uniform physical theory of diffraction equivalent edge currents for truncated wedge strips. *IEEE Transactions on Antennas and Propagation*, 44(7), 1996.

P. Kroese and Z. Botev. Spatial process generation. 08 2013.

M. Lindqvist. Onsala's 25-metre radio telescope celebrates 50 years, 2014. URL `http://www.chalmers.se/en/researchinfrastructure/oso/news/Pages/Onsala's-25-metre-radio-telescope-celebrates-50-years.aspx`.

H. B. Liu, H. Zhong, N. Karpowicz, Y. Chen, and X. C. Zhang. Terahertz spectroscopy and imaging for defense and security applications. *Proceedings of the IEEE*, 95(8), August 2007.

B. Lyons. Multiwavelength astronomy: Your world in different light. Slideshow Presentation, 2016.

M. Montgomery, N. Malloy, C. Muhl, et al. Atmospheric absorption and transmission, 2015. URL `http://gsp.humboldt.edu/olm_2015/Courses/GSP_216_Online/lesson2-1/atmosphere.html`.

NASA. Terahertz tools advance imaging for security, industry. URL `https://spinoff.nasa.gov/Spinoff2010/ps_8.html`.

NASA. The WMAP achievement, 2010. URL `https://map.gsfc.nasa.gov/mission/sgoals_universe.html`.

NASA. The electromagnetic spectrum, 2013. URL `https://imagine.gsfc.nasa.gov/science/toolbox/emspectrum1.html`.

NASA. Fermi gamma-ray space telescope, 2017. URL `https://www.nasa.gov/content/fermi-gamma-ray-space-telescope`.

National Instruments. *LabVIEW User Manual*. 11500 North Mopac Expressway, Austin Texas, 2003.

O. Nyström. *'Design, Characterization, and Calibration of Low-Noise Terahertz Receivers'*. PhD thesis, Chalmers University of Technology, 2011.

A. Y. Pawar, D. D. Sonawane, K. B. Erande, and D. V. Derle. Terahertz technology and its applications. *Drug Invention Today*, 5(2):157–163, June 2013.

K.-E. Peiponen, J. Zeitler, and M. Kuwata-Gonokami. *'Terahertz Spectroscopy and Imaging'*. Springer, 2013.

E. Pickwell, B. E. Cole, A. J. Fitzgerald, M. Pepper, and V. P. Wallace. In vivo study of human skin using pulsed terahertz radiation. *Physics in Medicine & Biology*, 49:1595, 2004.

K. Riley, M. Hobson, and S. Bence. *'Mathematical Methods for Physics and Engineering'*. Cambridge, 2006.

J. Ruze. Antenna tolerance theory a review. *Proceedings of the IEEE*, 54(4):633–640, 1966.

D. Rytting. *Network analyzer error models and calibration methods*. Palo Alto, California, 1998.

P. Schilke, T. D. Groesbeck, G. A. Blake, and T. G. Phillips. A line survey of orion kl from 325 to 360 ghz. *The Astrophysical Journal Supplement Series*, 108: 301–337, 1997.

P. K. Sethy, P. R. Mishra, and S. Behera. An introduction to terahertz technology, its history, properties and application. *International conference on computing and communication*, February 2015.

SKA. URL `http://skatelescope.org/ska-organisation/`.

SKA. Designing the ska telescopes – across 18 time zones: A global effort to deliver a dish prototype, 2019. URL `https://www.skatelescope.org/news/across-18-time-zones-a-dish-prototype/`.

D. G. Smith. *'Field Guide to Physical Optics'*. SPIE, 2013.

SWISSto12, 2018. URL `http://www.swissto12.com/`.

R. Syms and J. Cozens. *'Optical Guided Waves and Devices'*. McGRAW-HILL Book Company Europe,, 1992.

TICRA. *'GRASP Technical Description'*. 2013.

N. Trappe. *'Quasi-optical Analysis of the HIFI instrument for the Herschel Space Telescope'*. PhD thesis, Maynooth University, 2002.

N. Tynan. *'Accurate Characterisation of Refractive Components for Future CMB Missions'*. PhD thesis, Maynooth University, 2016.

G. Walker. *'Design and Analysis of the Onsala 4 mm Receiver and other Antenna Configurations for Millimeter Wave Astronomy'*. PhD thesis, Maynooth University, 2016.

M. Whale. 'OSO 4mm receiver - notes on optical design and prescribed work packages'. November 2014.

G. Winnewisser. Interstellar and laboratory spectroscopy in the terahertz region. *Journal of Molecular Structure*, pages 1–10, 1997.

S. Withington. Terahertz astronomical telescopes and instrumentation. *Phil. Trans. R. Soc. Lond. A*, 362:395–402, 2004.

Wolfram Research. Mathematica, Version 10.2. Champaign, IL, 2017.